Alma Mater Studiorum - Università di Bologna

Dipartimento di Fisica e Astronomia
Corso di Astrofisica e Cosmologia

First evidence of a shock in a radio mini-halo cluster: implications from new LOFAR data

Tesi di laurea

Presentata da:
Noemi La Bella

Relatore:
Prof. Myriam Gitti

Correlatori:
Prof. Annalisa Bonafede
Dr. Timothy Shimwell

Appello IV
Anno Accademico 2019-2020

Contents

Abstract

Diffuse non-thermal radio emission in galaxy clusters provides direct information on the relativistic particles and magnetic fields in the intracluster medium (ICM). Radio halos and mini halos are two types of these radio sources. Radio halos are extended ($\simeq$ Mpc-scale) synchrotron sources found in merging systems, whereas mini-halos are found in cool core galaxy clusters, extending on a smaller scale (≤ 500 kpc) around the radio-loud AGN. Both of them are characterized by steep spectrum ($\alpha < -1, S \propto \nu^{\alpha}$). With the advent of the LOw Frequency ARray, LOFAR, new properties of the diffuse emission in galaxy clusters have been revealed in the low radio frequencies. One of these recent discoveries is the presence of ultra-steep spectrum radio emission on Mpc scale outside the cool-core. This new zoology of sources opens new questions on the mechanism which triggers particles acceleration on larger scale. A possible scenario is an emission induced by the sloshing motion of the core after a minor merger, which dissipates low energy in the ICM and can produce steep spectra commonly observed at low frequency.

The origin of the mini-halos in cool-core cluster is still debated. Hadronic and turbulence re-acceleration models have been proposed to explain their emission. In the re-acceleration scenario, turbulence can be generated by the sloshing core motion or by the AGN feedback process. In this context, the X-ray detection of shocks or cold fronts in the ICM can probe the process which produces turbulence in cool-core clusters. However, few mini-halos have been studied in detail, due to their small size and the presence of the strong central source, and no clear conclusions on their origin and spectral properties have been obtained so far.

The high sensitivity and resolution of the LOFAR array allow us to better distinguish between the emission of the core and the mini-halo, and reveal the steep spectra of these sources.

New LOFAR observations of the cool-core galaxy cluster RBS797 were requested with the aim to investigate signs of steep large scale emission extending outside the cool core, beyond the known mini-halo. In order to perform an accurate investigation of this scenario, we carried out a multi-wavelength study to reveal the presence of surface brightness discontinuities in the ICM possibly associated to shock or cold fronts.

The low resolution LOFAR image produced in this thesis work does not show Mpc diffuse emission and leads to an upper limit of the undetected emission of $P_{140\mathrm{MHz}} < 1.4 \times 10^{24}$ W/Hz. Comparing the low resolution 140 MHz LOFAR image with the 1.4 GHz VLA image, obtained using VLA archival observation, we found a more extended diffuse emission at the high frequency. Spectral index analysis of this mini-halo was performed and a flattening of the spectral index toward the external region was found, in

particular $\alpha = -0.45 \pm 0.09$. This represent the first detection of a flattening of the diffuse radio emission spectra, and one possible explanation of this trend is the presence of a shock wave propagating to the external region of the cluster. However, no shock surrounding the edges of mini-halo has been detected before this work in any system.

The X-ray analysis was carried out by means of detailed morphological and spectroscopic study of archival Chandra observation, in order to detect brightness discontinuities in the ICM, and investigate to their possible relation with the extended radio emission.

From our analysis, we discovered an inner discontinuity, at $\simeq 43$ kpc, which can be associated to the presence of bright rims surrounding the prominent cavities, and an outer discontinuity, at $\simeq 84$ kpc from the center, which presents thermodynamic properties consistent with those typically found in shock fronts. These findings are compatible with the radio properties: the presence of a of a possible "cocoon shock" propagating in the ICM, which compresses, heats the plasma, and re-accelerate relativistic particles to higher energy, can explain a larger extension of the 1.4 GHz emission with respect to the 140 MHz LOFAR emission, and the flattening of the spectral index increasing with the distance from the center.

This represents the first direct indication of a cocoon shock in the boundary of a mini-halo, thus providing new evidences of the link between the AGN feedback and the mini-halo origin. Its detection will be spectroscopically confirmed by the upcoming deep Chandra exposure (420 ks awarded in Cycle 21, PI Gitti), which will provide important implications for the origin of radio mini-halos.

This Thesis work is organized as follows.

- In Chapter 1 we introduce the thermal and non thermal emission properties of galaxy clusters. This thesis mainly focus on the non thermal diffuse phenomena.

- In Chapter 2 we briefly describe the basic concepts of the radio interferometry and highlight the difference between the classical interferometry and the new generation of low frequencies interferometers. We also provide an overview of LOFAR new array and the techniques used for analysing the data.

- In Chapter 3 we present the main results of the LOFAR radio analysis, the new images produced and our accurate spectral study of the mini-halo in this cool-core cluster.

- In Chapter 4 we report the main steps of the Chandra analysis and describe our detailed morphological and spectroscopic investigation of brightness discontinuities in the ICM.

- In Chapter 5 we summarize the main results obtained from the LOFAR and Chandra analysis and present our multi-wavelength interpretation of the new discoveries found in RBS797.

Sommario

L'emissione diffusa non termica negli ammassi di galassie fornisce informazioni sulle particelle relativistiche e campi magnetici nell'ICM. Radio aloni e mini aloni sono due tipi di queste radio sorgenti. I radio aloni sono oggetti che emettono per sincrotrone su scale del Mpc e sono trovati in sistemi con eventi di merger, invece i mini aloni sono sorgenti che si trovano al centro degli ammassi di galassie cool-core e si estendono su scale di $\simeq 500$ kpc. Entrambe sorgenti sono caratterizzate da spettri ripidi ($\alpha < -1, S \propto \nu^\alpha$). Grazie alle osservazioni in bassa frequenza dell' interferometro LOFAR, LOw Frequency ARray, sono state rivelate nuove peculiari proprietà dell'emissione diffusa negli ammassi di galassie. Una di queste recenti scoperte è la presenza di emissione radio molto ripida trovata su scale del Mpc fuori dal core. Questa nuova zoologia di sorgenti apre nuove domande sul possibile meccanismo capace di accelerare le particelle su scale più grandi. Un possibile scenario è che l'emissione sia generata dal moto di sloshing del core, dopo un evento di merger minore. Questo dissipa basse energie nell'ICM e può produrre spettri molto ripidi comunemente osservati nella bassa frequenza. L'origine dei mini aloni negli ammassi di galassie cool-core è ancora sconosciuta. Per spiegare questa emissione sono stati proposti modelli adronici o di riaccelerazione indotta da turbolenza. In quest'ultimo scenario, la turbolenza può essere generata dal moto di sloghing del core oppure dal meccanismo di AGN feedback. In questo contesto, la rivelazione nei raggi X di shock e cold front nel ICM può indicare il processo che produce turbolenza negli ammassi cool-core. Tuttavia, non ci sono chiare idee sull'origine di questi oggetti e sulle loro proprietà spettrali, perchè pochi mini aloni sono stati fino ad ora studiati in dettaglio, a causa della loro piccola dimensione e della forte emissione della sorgente centrale.

L'alta sensitività e risoluzione dell'interferometro LOFAR ha permesso di poter distinguere meglio l'emissione del core da quella del mini alone e di rivelare lo spettro ripido di queste sorgenti.

Le nuove osservazioni LOFAR dell'ammasso cool-core RBS797 sono state richieste con il fine di indagare sulla presenza di una emissione a spettro ripido fuori il cool-core e su scale più grandi del mini alone. Per ottenere un'accurata analisi di questo scenario, abbiamo portato avanti uno studio multi-banda in modo da rivelare la presenza di discontinuità in brillanza nell'ICM, possibilmente associati ad shock o cold front.

L'immagine a bassa risoluzione che abbiamo realizzato in questo lavoro di tesi non mostra emissione diffusa su larga scala, in particulare l'emissione non rivelata presenta un upper limit di $P_{140\text{MHz}} < 1.4 \times 10^{24}$. Confrontando l'immagine a bassa risoluzione LOFAR a 140 MHz, con l'immagine ad alta risoluzione VLA a 1.4 GHz, ottenuta da osservazioni di archivio, abbiamo trovato un'emissione diffusa più estesa alle alte frequenze. Tramite un'analisi

di indice spettrale del mini alone, abbiamo scoperto un indice spettrale che si appiattisce spostandoci verso le zone esterne dell'ammasso, in particolare $\alpha = -0.45 \pm 0.09$ (S $\propto \nu^{\alpha}$). Dal momento che questo rappresenta la prima volta che viene trovato un appiattimento dell' indice spettrale dell'emissione diffusa, una possibile spiegazione che abbiamo dato è legata alla presenza di uno shock che si propaga nelle zone esterne dell'ammasso. Tuttavia, non è mai stato trovato uno shock che circonda un mini alone prima di questo lavoro di tesi. Quindi, in seguito, abbiamo analizzato in dettaglio osservazioni Chandra sia dal punto di vista morfologico che spettroscopico, con lo scopo di rivelare discontinuità in brillanza nell'ICM, ed eventualmente collegare la loro presenza con l'emissione radio estesa.

In questa analisi, abbiamo scoperto una discontinuità interna, a circa 43 kpc, che può essere associata alle rims brillanti che circondano le prominenti cavity, ed una discontinuità esterna, a circa 84 kpc dal centro, che presenta proprietà termodinamiche tipicamente osservate negli shock. Questo possibile "cocoon shock" che si propaga nell'ICM, comprime e riscalda il plasma, e può ri-accelerare le particelle relativistiche nelle alte energie. Dunque, la sua presenza spiega sia l'emissione più estesa rilevata ad 1.4 GHz rispetto a quella 140 MHz, sia l'appiattimento dell'indice spettrale verso le zone esterne. Questa nostra scoperta rappresenta la prima diretta rivelazione di un coocon shock al confine del mini alone e fornisce nuove evidenze del legame tra il processo di AGN feedback e l'origine del mini alone. La sua presenza potrà essere spettroscopicamente confermata con le nuove esposizioni Chandra (420 ks, ottenute nel Ciclo 21, PI Gitti), che forniranno importanti implicazioni sull'origine dei mini aloni.

Questa tesi è organizzata come segue.

- Nel Capitolo 1 introduciamo le proprietà termiche e non termiche degli ammassi di galassie. Questa tesi principalmente si focalizza sui fenomeni non termici.

- Nel Capitolo 2 descriviamo brevemente i concetti alla base dell'interfometria ed evidenziamo le differenze tra la classica radio interferometria con la nuova generazione di interferometri a bassa frequenza. Inoltre, presentiamo le principali caratteristiche del nuovo interferometro LOFAR e le tecniche che vengono usate per analizzare i dati.

- Nel Capitolo 3 presentiamo i principali risultati ottenuti dall'analisi LOFAR, ovvero le nuove immagini e un accurato studio dell'indice spettrale del mini alone di questo ammasso.

- Nel Capitolo 4 riportiamo l'analisi dei nostri dati Chandra e la nostra dettagliata analisi morfologica e spettroscopica sulle discontinuità in brillanza nell'ICM.

- Nel Capitolo 5 riassiumiamo i risultati principali ottenuti dall'analisi LOFAR e da quella Chandra, e presentiamo la nostra interpretazione multi-banda delle nuove scoperte trovate in RBS797.

Chapter 1

Galaxy Clusters

Galaxy clusters (GCs) are the most massive virialized aggregates of matter in the Universe, characterized by gravitational masses of $\sim 10^{14} - 10^{15} \mathrm{M_\odot}$. Dark Matter is the dominant component of GCs ($\sim 80\%$), while baryonic matter constitutes a small fraction (~ 20 %) of the total mass of clusters. Although GCs were first identified in optical band (Abell, 1958), stars in galaxies represent only a few percent of the baryonic mass. Most of the baryons in clusters reside in a hot (T $\sim 10^7 - 10^8$ K) rarefied ($n_{gas} \sim 10^{-3}\,\mathrm{cm^{-3}}$) plasma, called Intra Cluster Medium (ICM), which accounts for the $\sim 15\%$ of a cluster's mass budget. This high temperature is set by the virialization process in deep potential well of dark matter halo during the cluster formation.

According to the standard cosmological scenario, GCs form via hierarchical process of mergers and accretion of smaller structures (Peebles & Yu, 1970; Press & Schechter, 1974; Voit, 2005). These objects are created as a consequence of the gravitational collapse driven by overdense perturbations of dark matter generated in the primordial Universe (for more details see Coles & Lucchin 2002). This cosmological picture is supported by cosmological simulation, such as the *Millenium Simulation* (Springel, 2005), which is shown in Figure 1.1. The large vacuum regions and cosmic filaments constitute a connected network called *cosmic web* (van de Weygaert & Bond, 2008), whose intersections are occupied by GCs.

The thousand of galaxies contained in GCs cross the system with a crossing time estimated as (Sarazin, 2009):

$$t_{cr} = \frac{\sigma_v}{d} \approx 10^9 \mathrm{yr} \left(\frac{d}{\mathrm{Mpc}}\right) \left(\frac{\sigma_v}{10^3 \mathrm{Km/s}}\right)^{-1} \tag{1.1}$$

where d is the cluster diameter and $\sigma_v = 1000$ Km/s is the velocity dispersion of galaxies. Comparing this crossing time with a Hubble time of $t_0 = 13.7$ Gyr [1], only the central region of GCs ($\sim 1\mathrm{Mpc}$) can reach the dynamic equilibrium. Assuming the validity of the *Virial Theorem*, the typical virial mass of GCs is given by:

$$M_{vir} \simeq \frac{r_{vir}\sigma_v^2}{G} \simeq 10^{15} \mathrm{M_\odot} \left(\frac{r_{vir}}{\mathrm{Mpc}}\right) \left(\frac{\sigma_v}{10^3 \mathrm{Km/s}}\right)^2 \tag{1.2}$$

where G is the gravitational costant and r_{vir} is the virial radius of the cluster.

---

[1]In this thesis work we assume a cosmology with $H_0 = 70\,\mathrm{km\,s^{-1}\,Mpc^{-1}}$, $\Omega_m = 0.3$ and $\Omega_\Lambda = 0.7$.
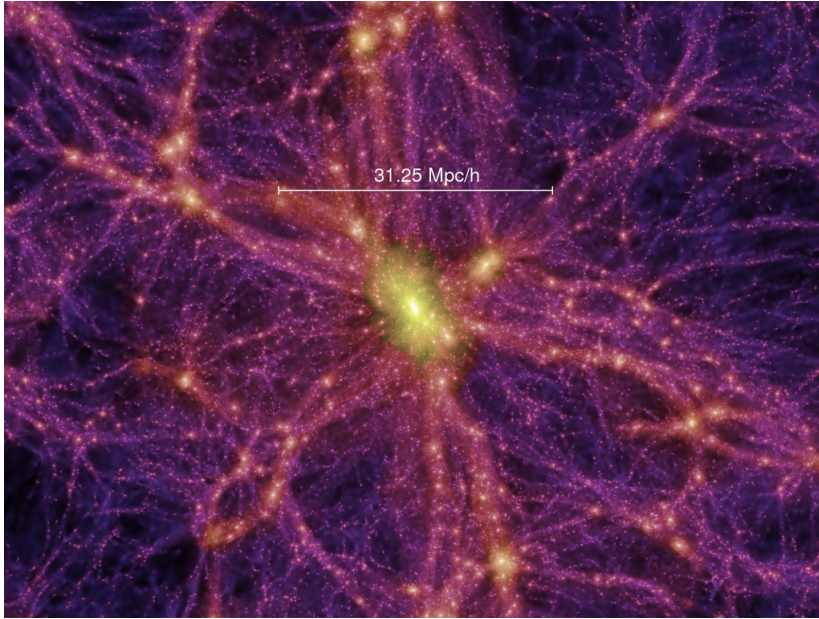
Figure 1.1: The Millenium Simulation is the largest N-body simulation which traces the dark matter distribution at the present time ($z = 0$, i.e. $t_0 = 13.7$ Gyr). By zooming a node of this *cosmic web*, the figure evidences an example of intersection in which GCs reside. From Springel (2005).

1.1 Thermal emission

GCs are very strong X-ray emitters with luminosities of $\sim 10^{43} - 10^{45}$ erg/s. At the typical temperature and density of GCs, most of the X-ray continuum emission is due to thermal Bremsstrhlung from the ICM (Felten et al., 1966). The specific emissivity at frequency ν (i.e. emitted energy per unit time, frequency and volume) of a hot fully ionized plasma with an atomic number Z and a temperature T is (Rybicki & Lightman, 1986):

$$J_{br}(v, T) = 6.8 \times 10^{-38} Z^2 n_e n_i T^{-1/2} e^{-h\nu/kT} \overline{g}(v, T) \; [\text{erg cm}^{-3}\text{s}^{-1}\text{Hz}^{-1}] \qquad (1.3)$$

where $\overline{g}(v, T)$ is the Gaunt factor, which includes corrections for quantum mechanical and distant collisions effects, n_e and n_i are the number density of electrons and ions, respectively. If GCs are considered as relaxed systems, the ICM can be assumed in hydrostatic equilibrium, whose condition is defined by the following equation:

$$\frac{1}{\rho} \cdot \frac{dp}{dr} = -\frac{d\phi}{dr} \qquad (1.4)$$

where ϕ is the gravitational potential of the cluster, ρ is the gas density and p is the gas pressure. Considering the ICM as spherical symmetric and perfect gas (i.e. $P = k\rho T/\mu m_p$, with μ the mean molecular weight and m_p the proton mass), the Eq. 1.7 becomes:

$$\frac{1}{\rho} \cdot \frac{dp}{dr} = -\frac{GM(r)}{r^2} \qquad (1.5)$$

with $M(r)$ the total mass of the cluster inside the radius r. Under these hypothesis, another method to estimate the total mass of GCs, is:

$$M_{tot}(< r) = -\frac{kTr}{G\mu m_{\rm p}} \left[\frac{d\,\ln\rho}{d\,\ln r} + \frac{d\,\ln T}{d\,\ln r} \right] \tag{1.6}$$

The gas density and temperature profiles are quantities measured directly from X-ray observations (e.g. Gitti et al., 2007; Ettori et al., 2010). Cavaliere & Fusco-Femiano (1976) proposed a gas density profile under the assumption that the ICM is isothermal and the cluster potential is described by King's model [2]. This density radial profile is expressed by:

$$\rho(r) = \rho_0 \left[1 + \left(\frac{r}{r_{\rm core}} \right)^2 \right]^{-\frac{3}{2}\beta} \tag{1.7}$$

where $r_{\rm core}$ is the core radius (i.e. a measure of the size of the central core) and β is defined as:

$$\beta = \frac{\sigma_r^2}{kT/\mu m_{\rm p}} \tag{1.8}$$

with σ_r the velocity dispersion in the line-of-sight. This gas density distribution is known as *β model*, where the β parameter represents the ratio of specific kinetic energies of galaxies and gas. It can be derived by fitting the X-ray surface brightness radial profile $I(b)$ at the projected radius b, which is obtained from the integration of the emissivity of the gas along the light of sight:

$$I(b) = I_0 \left[1 + \left(\frac{b}{r_{\rm core}} \right)^2 \right]^{\frac{1}{2}-3\beta} \tag{1.9}$$

Substituting Eq. 1.7 in Eq. 1.6, the β mass profile can be written as:

$$M_{tot}(< r) = \frac{kr^2}{G\mu m_{\rm p}} \left[\frac{3\beta rT}{r^2 + r_{\rm core}^2} - \frac{dT}{dr} \right] \tag{1.10}$$

This simple model depends only on three parameters and gives a first approximation of the brightness profile of GCs. However, it underestimates the centrally peaked emission of *cool-core galaxy cluster* (e.g. Pratt et al., 2009), explained in the next subsection. This central excess emission can be qualitatively described by the *double β model* (Xue & Wu, 2000; Mohr et al., 1999), which considers the ICM as a two-phase gas in hydrostatic equilibrium. Thanks to Chandra [3] and XMM-Newton[4] observations, accurate profiles of thermodynamical properties of several GCs have been obtained (e.g. Croston et al., 2006; Molendi et al., 2002; Arnaud et al., 2010). Due to the high particles backgrounds of these satellites, the observations provide profiles throughout the ICM within less than half of the virial radius. The advent of the Suzaku[5] satellite allowed to extend these studies in the outskirts regions of several GCs (e.g. Urban et al., 2014)), which observations showed a steep decrease of temperature profiles at

---

[2]In the King's approximation the gravitational potential of the cluster is assumed to come both from the gas and the galaxies (King, 1962).

[3]https://chandra.harvard.edu/

[4]https://heasarc.gsfc.nasa.gov/docs/xmm/xmm.html

[5]https://www.nasa.gov/suzaku

R_{500} (i.e. the radius within which the mean density is 500 times the critical density of the Universe) and beyond. Many research works has recently focused on the derivation of universal density, temperature, pressure profiles of GCs. In this context, Ghirardini et al. (2019) investigate the ICM properties over the entire cluster volume of the GCs in the *XMM Cluster Outskirts Project*, X-COP (Eckert, 2017), a very large program on XMM-Newton which combines X-ray observations with the *Sunyaev-Zel'dovich* (SZ)[6] signal out to the virial radius.

Although the Suzaku satellite has a lower background than the Chandra e XMM satellites, and hence allows us to study the outskirts emission in GCs, its angular resolution is limited to $\simeq 2'$. Therefore it does not reach good spatial resolution as in the case of Chandra, which has a resolution of $\simeq 0.5''$. In our thesis work, to detect brightness discontinuities in the ICM, we needed the higher resolution of Chandra observations.

1.2   Cool-core Galaxy Clusters

As we discussed above, thermal bremsstrahlung is the main X-ray emission process from GCs. The ICM looses energy in a radiative cooling time t_{cool}, given by:

$$t_{cool} = \frac{5}{2} \frac{k\rho T}{\mu m_{\rm p}} \frac{1}{n_e n_i \Lambda(T)} \tag{1.11}$$

where $\mu \simeq 0.6$ is the molecular weight typical of the ICM and $\Lambda(T)$ is the cooling function (Sutherland & Dopita, 1993). At the the centre of cool-core GCs the densest gas has sufficient time to cool, indeed $t_{\rm cool}$ is shorter than the age of the cluster. In particular, we can define the *cooling radius* as the radius at which the cooling time equals the age of the cluster. In Fig. 1.2, we can see the cooling time as a function of radius for a sample of relaxed clusters. Therefore, cool-core GCs are characterized by dropped temperature profile at smaller radii.

GCs disturbed by *mergers* do not show strong signs of cooling, indeed we can distinguish two morphology of clusters as cool-core and non cool-core GCs (Molendi & Pizzolato, 2001).

In absence of heating mechanism, the loss of thermal energy at the center of cool-core cluster, reduces the gas pressure, and a phenomenon known as *cooling-flow* is expected (Fabian, 1994), in which the gas should flow toward the center. The *mass inflow rate* $\dot{M}_{cool}$, with typical value of $\sim 100 M_\odot$ yr^{-1} (Fabian, 1994), can be estimated by the X-ray luminosity $L_{\rm cool}$ from the cooling region (i.e. the region inside the cooling radius), as:

$$L_{\rm cool} = \frac{5}{2} \frac{\dot{M}_{\rm cool}}{\mu m_{\rm p}} k T_{\rm gas} \tag{1.12}$$

When the gas cools down it is compressed by the surrounding environment, leading to a further increase of the central density and consequently of X-ray emissivity. In particular, peaked surface brightness distribution are detected. However, high resolution spectral observation with Chandra and XMM-Newton, revealed that the expected cooling flow rates were overestimated and that the mass inflow rate from observations

---

[6]The Sunyaev-Zel'dovich effect is produced by the interaction of the CMB photons with the hot electrons in the ICM, which leads to a distortion of the black-body spectrum of the CMB (Sunyaev & Zeldovich, 1972)

is $\dot{M}_{\mathrm{obs}} \sim 0.1 \dot{M}_{\mathrm{cool}}$. The lack of the expected " flow " for these system represents the so-called *cooling-flow problem* (McNamara & Nulsen, 2007).
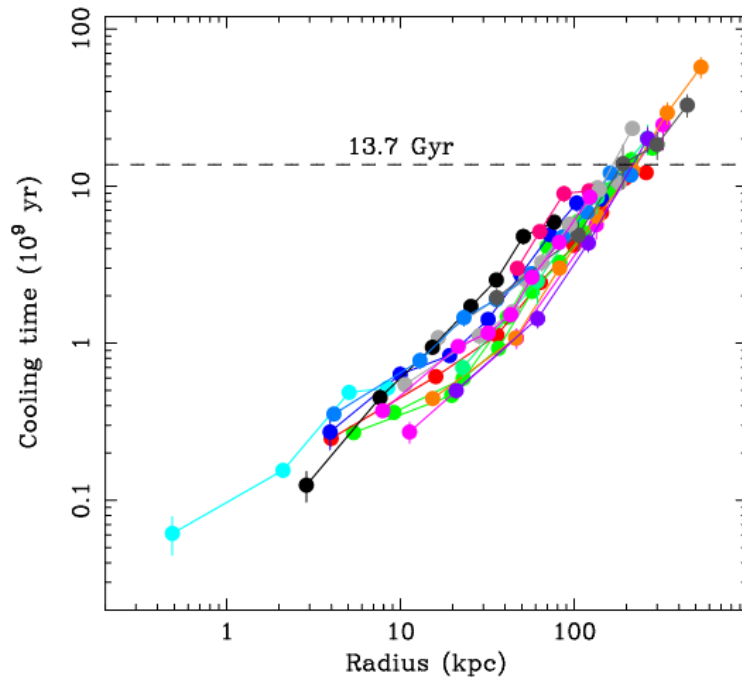
Figure 1.2: Cooling time t_{cool} as a function of radius for a sample of relaxed clusters. The undisturbed plasma within 100 to 200 kpc have sufficient time to cool. From Peterson & Fabian (2006).

1.2.1 AGN feedback

All GCs host a *brightest cluster galaxy* (BCG) in its centre, which is defined as the brightest galaxy in a GC with typical masses of $M \sim 10^{12} \mathrm{M}_\odot$ and luminosities $L \sim 10^{12} L_\odot$. The *Active Galactic Nuclei* feedback process in the BCG represents the most accredit solution to the cooling flow problem (see Gitti et al., 2012; McNamara & Nulsen, 2012, for reviews). In particular, the flowing gas into the central regions powers the AGN, which starts its activity and heats the surrounding ICM, without destroying the cool-core. This heating can be due to energetic outflows in the form of the radio jets which inflate "*cavities*" in the ICM, detectable as a deficit in the X-ray images. These features are evident in Fig. 1.3, which shows a deep Chandra X-ray image and a VLA[7] radio image, superposed onto an optical image with *Hubble Space telescope*[8] of the GC MS0735.

The cavities allow to estimate the mechanical energy output of the AGN through its enthalpy (i.e the sum of internal energy of the lobes and the jet work required to inflate the radio bubbles), which can be written as:

$$E_{cav} = E_{\mathrm{int}} + PV \tag{1.13}$$

where V is volume of the cavity and P is the pressure within the cavity assuming that the cavity is in pressure balance with its surrounding ICM.The product of these

---

[7]http://www.vla.nrao.edu
[8]https://hubblesite.org

two quantities can be derived directly by X-ray observations. From Eq. 1.13, we can estimated P_{cav} as E_{cav}/t_{cav}, where t_{cav} is the cavity age. Fig. 1.4 shows the cavity power P_{cav}, scaled to the cooling X-ray luminosity L_{cool} for different samples (Bîrzan et al., 2008; Cavagnolo et al., 2010; O'Sullivan et al., 2011). Despite the large scatter, it is evident the proportion between P_{cav} and L_{cool}. This correlation supports a self-regulated AGN feedback process, in which the cold gas is the fuel required to power the bipolar outflows and the outflows themselves heat the cooling gas. In addition to the cavity enthalpy of expanding radio bubbles, there are other possible channels of heating from AGN outbursts which include *turbulence* (Zhuravleva et al., 2014), *internal waves* (Zhang et al., 2018), *weak shocks* (Fabian et al., 2006). However, the details of how the AGN feedback process operates remain highly debated.
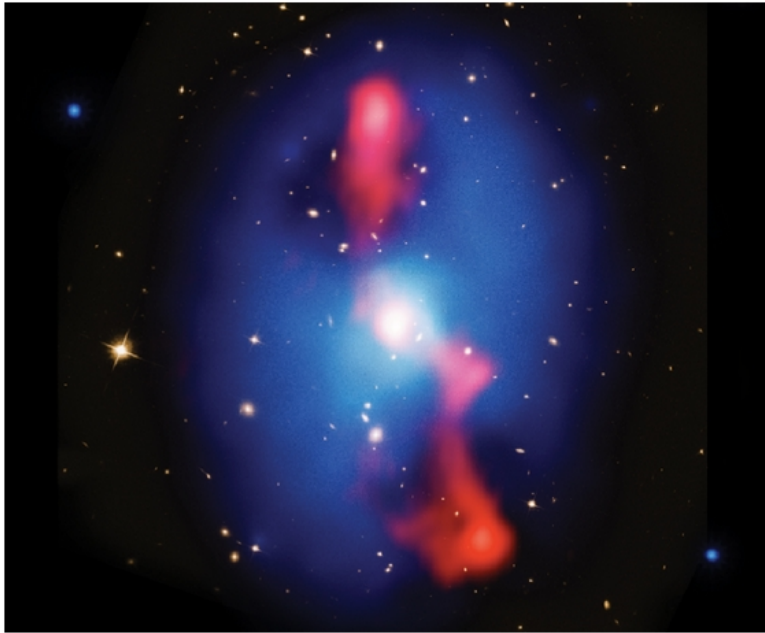
Figure 1.3: Deep Chandra X-ray image and VLA 330 MHz radio image, superposed to the *Hubble Space Telescope* optical image of the GC MS0735. The image shows an example of radio lobes (red) which fill X-ray cavities (blue). From Gitti et al. (2012).
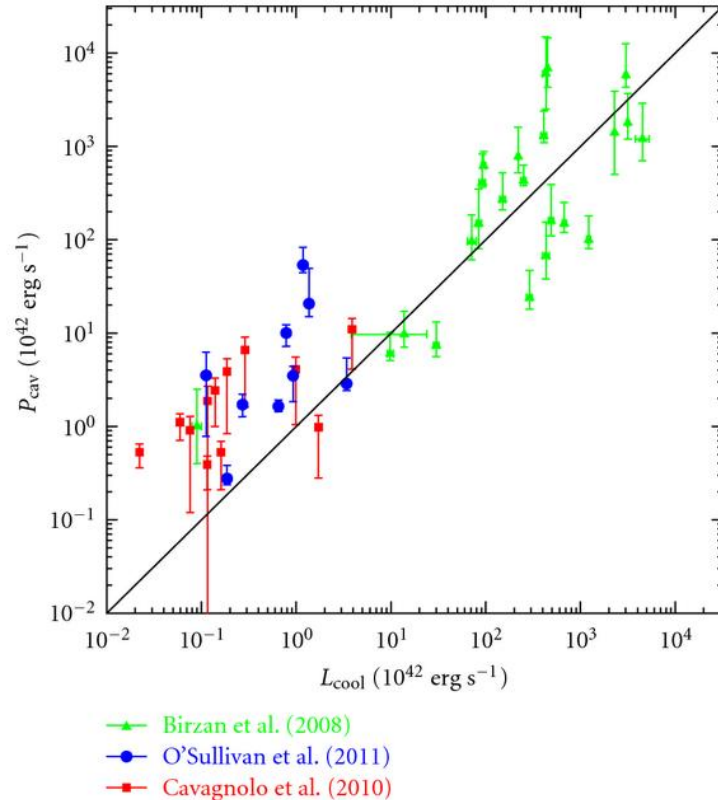
Figure 1.4: P_{cav} versus L_{cool} for a different samples (Bîrzan et al., 2008; Cavagnolo et al., 2010; O'Sullivan et al., 2011). The solid line indicates $P_{cav} = L_{cool}$. In most of the systems, heating balances X-ray gas cooling. From Gitti et al. (2012).

1.3   Brightness discontinuities in the ICM

Shocks and cold fronts are brightness discontinuities in the ICM, which are very important to understand the origin of the diffuse non-thermal emission in GCs, explained in the next section. They are commonly observed in *merging GCs*, which are dynamically disturbed systems undergoing through very energetic phenomena, called *mergers*. These energetic events generate perturbations in the ICM and dissipate the total kinetic energy up to $10^{63} - 10^{64}$ erg through weak shock in a cluster crossing time t_{cross} (Sarazin, 2002). In Fig. 1.5 we can see the so-called *Bullet Cluster*, named "Bullet" for its shape, where there is evidence of both merger shock and cold front.

These discontinuities are also observed in cool-core GC, in particular shocks can be generated by the radio bubbles of the central AGN which expand in the surrounding medium. These weak shocks can propagate almost isotropically over few hundred kpc regions from the GC center. The GC MS0735 hosts a beautiful example of this "cocoon shock", which is showed in Fig. 1.3 (Gitti et al., 2012). Cold fronts are also observed near the centers of cool-core GCs. They can be produced by the *sloshing mechanism*, in which the gas sloshes in the cluster potential well as a consequence of an interaction with an infalling sub-structures (ZuHone & Markevitch, 2010) or of a disturbance induced by the relativistic radio bubbles. However, their origin is still not fully understood indeed few sloshing cool cores has been studied so far (e.g. Johnson et al., 2010).

The high resolution (i.e. sub-arcsec) of Chandra observations allowed to study sharp

brightness discontinuities in GCs. A more detailed description of these features can be found in Markevitch & Vikhlinin (2007). Both of these discontinuities show a temperature jump across the front. Shocks are more evident in the gas pressure profile, indeed when the shock propagates in the ICM, it compresses and heats the medium, modifying the dynamical proprieties of GCs (Markevitch et al., 1999). Cold fronts represent the opposite situation of the shock front, the denser region has a lower temperature and the pressure across the edge is nearly continuous.

Shock waves are supersonic waves with a propagation speed faster than the speed of light and can be characterized by Mach number, defined as:

$$\mathcal{M} = \frac{V_{\text{sh}}}{c_{\text{s}}} \tag{1.14}$$

where V_{sh} is the shock velocity and c_{s} is the sound speed of the gas unperturbed by the shock, which can be written as:

$$c_s = \sqrt{\frac{5}{3}\frac{P}{\rho}} \tag{1.15}$$

where we assume a monoatomic gas. We can derive the "jump conditions" across the front with the Rankine-Hugoniot relations:

$$R \equiv \frac{T_d}{T_u} = \frac{5\mathcal{M}^4 + 15\mathcal{M}^2 - 3}{16\mathcal{M}^2} \tag{1.16}$$

$$C \equiv \frac{n_d}{n_u} = \frac{4\mathcal{M}^2}{\mathcal{M}^2 + 3} \tag{1.17}$$

$$P \equiv \frac{P_d}{P_u} = \frac{5\mathcal{M}^2 - 1}{4} \tag{1.18}$$

where u and d indicate the *upstream* and *downstream* gas, respectively. The temperature and the density jump can be measured directly from X-ray analysis of the regions before and after the shock front.
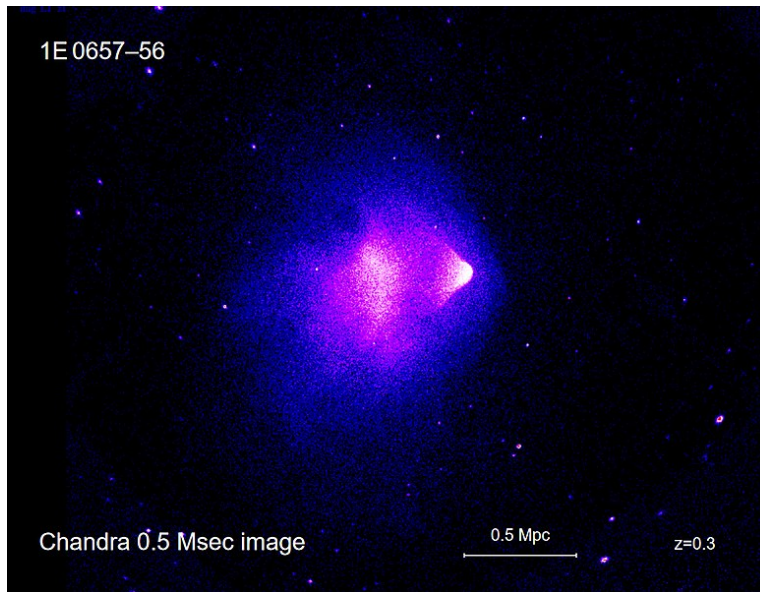
Figure 1.5: X-ray image by Chandra X-ray Observatory of the Bullet Cluster ($z = 0.3$). A shock propagates and interacts with the surrounding environment. A cold front is created in the boundary of the "bullet ". From Markevitch (2012).

1.4 Non-thermal emission from Galaxy Cluster

Radio observations have shown the presence of diffuse radio emission in some GCs. The synchrotron radiation extended up to Mpc scales is explained by the presence of magnetic field and a non-thermal component of *Cosmic Rays* (RC) in the ICM. This emission depends on energy of CR electrons and on the magnetic field strength. Before presenting the main properties of the three classes of radio diffuse emission, *radio halos*, *mini-halos* and *radio relics*, we introduce the synchrotron process and the magnetic field in the ICM, which are the main keys for understanding the diffuse radio emission in galaxy clusters (see van Weeren et al., 2019, for recent review).

1.4.1 Synchrotron radiative losses

Synchrotron emission is produced by the helical motion of a relativistic particle in the magnetic field of the cluster (e.g. Brüggen et al., 2012). The power emitted by a relativistic electron can be written as follow (see Longair, 2011, for more details):

$$\frac{\mathrm{d}E}{\mathrm{d}t} = -1.2 \times 10^{-15} \gamma^2 B^2 sin^2\theta_p \ \ [\mathrm{erg \ s^{-1}}] \tag{1.19}$$

where B is the magnetic field strength, γ is the *Lorentz factor* and θ_p is the *Pitch angle* (i.e. the angle between the magnetic field and the particle motion). The population of CR electrons can be described by a power-law energy distribution N(E) with index δ, expressed by:

$$N(E)\mathrm{d}E \propto E^{-\delta}dE \tag{1.20}$$

The total monochromatic emissivity $J(\nu)$ can be obtained integrating over the electron population:

$$J(\nu) \propto (Bsin\theta_\mathrm{p})^{1+\alpha}\nu^{-\alpha} \tag{1.21}$$

where

$$\alpha = \frac{\delta - 1}{2} \tag{1.22}$$

is the spectral index of the power-law distribution of CR electrons. From Eq. 1.21 it is evident that high energy electrons loss efficiently their energy, leading to a steepening of the synchrotron spectrum for frequencies greater than the so-called *break frequency* (e.g. $\nu > \nu_b$).

Synchrotron emitting electrons interact with the photons of the *cosmic microwave background* CMB and originate the Inverse Compton scattering (IC) emission. In this process low-energy photons are up-scattered (i.e. gain energy) by relativistic electrons. The IC emissivity is proportional to $U_{\mathrm{CMB}} = B^2_{\mathrm{CMB}}/8\pi$ (e.g. energy density in the photon field), where B_{CMB} is the equivalent magnetic field strength of the CMB at redshift z is given by:

$$B_{\mathrm{CMB}} \simeq 3.25(1 + z)^2 \tag{1.23}$$

and it is measured in µG. Since the IC the synchrotron emissivity is proportional to $U_B = B^2/8\pi$ (e.g. energy density in the magnetic fields), the ratio of the synchrotron luminosity L_{syn} and the IC luminosity L_{CMB} can be expressed by:

$$\frac{L_{\mathrm{syn}}}{L_{\mathrm{CMB}}} = \frac{U_{\mathrm{B}}}{U_{\mathrm{CMB}}} \tag{1.24}$$
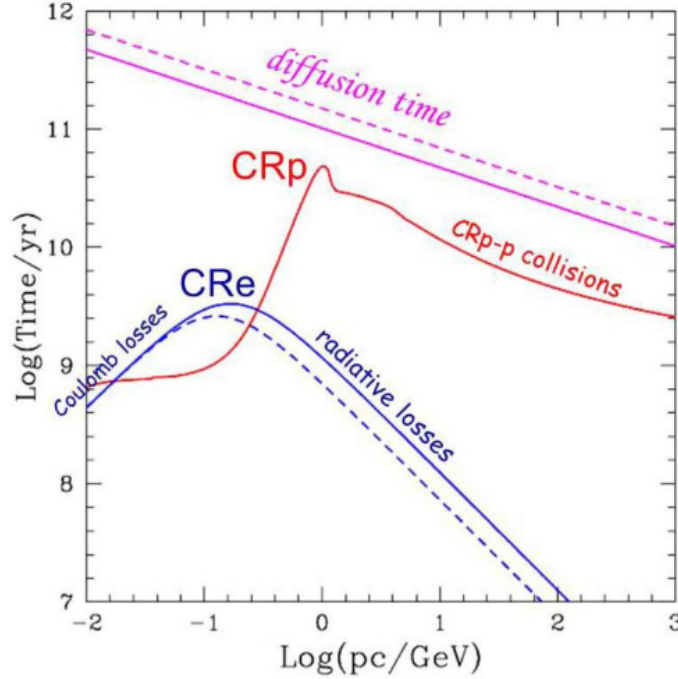
Figure 1.6: Life-time of CR protons (*red line*) and CR electrons (*blu line*) in the ICM at z= 0 compared with the CR diffusion time on Mpc scales (*magenta*). The solid lines and the dashed lines represent the life-times for a magnetic field of 1 µG and 3µG, respectively. From Brunetti & Jones (2014).

where $U_{\mathrm{CMB}} = 0.26 \mathrm{eVcm}^{-3}$. Considering both of electron energy losses (synchrotron radiation and IC radiation), the characteristic lifetime t_{loss} of emitting electrons at the break frequency ν_{b} (GHz) is:

$$t_{\mathrm{loss}} = 3.2 \times 10^{10} \frac{B^{1/2}}{B^2 + B_{\mathrm{CMB}}^2} [(1+z)\nu_{\mathrm{b}}]^{-1/2} \ \ [\mathrm{yr}] \tag{1.25}$$

where z is redshift of the source. This energy loss time for CR electrons is $t_{\mathrm{loss}} \leq 10^8$ yr. As CR protons not suffer from radiative losses as CR electrons do (the electron mass, $m_e = 9.11 \cdot 10^{31} kg$, and the proton mass is $m_p = 1.67 \cdot 10^{27} kg$), they are confined for several Gyr within the cluster volume. When CR protons interact with thermal protons produce neutral π^0 which decade in 2γ rays. The loss energy by these inelastic p-p collisions can be written as:

$$\tau_{pp} = \frac{1}{cn_{\mathrm{th}}\sigma_{\mathrm{pp}}} \tag{1.26}$$

where n_{th} is the number density of the ICM and σ_{pp} is the cross section of p-p collisions. Thus, CR protons with energy of 1 GeV - 1 TeV have a life-time of several Gyr. On the other hand, CR electrons are short-living particles, as we can see from Eq. 1.25. The CR protons and electrons life-times in the ICM are showed in Fig.1.6. At energies of $\simeq 100$ MeV, the radiative losses of CR electrons reach the maximum life-time of $\simeq 1$ Gyr. At low energies, they are dominated by Coulomb collisions (see Brunetti & Jones, 2014, for more details).

1.4.2 The role of the magnetic field

Magnetic fields are one of most important keys for the production of radio diffuse emission. The non-thermal sources in GCs provide a direct evidence for large scale magnetic fields associated with the ICM.

The origin and evolution of the magnetic field in GCs is not clearly understood. Several scenarios have been proposed to explain the presence of the magnetic fields in the ICM and we can divide them in two main classes: *cosmological origin*, in which the magnetic field is generated in the early universe before the *epoch of recombination* (Grasso & Rubinstein, 2001) and *galactic origin*, in which the magnetic field is due to ejection from galactic winds by normal galaxies or radio jets by AGNs (Furlanetto & Loeb, 2001).

Their typical value in GCs are estimated of order of µG, even if they are difficult to be measured. One method to study the magnetic field is the measurement of *Faraday rotation* of diffuse sources (Govoni & Feretti, 2004). This phenomena occurs when a linearly polarized radiation propagates in a magnetized plasma and the intrinsic polarization angle Φ_0 experiences a rotation in function of the observed wavelength λ, written as:

$$\Delta\Phi = \Phi - \Phi_0 = \lambda^2 RM \tag{1.27}$$

where RM is the *rotation measure*, given by :

$$RM = 812 \int_0^L n_e B_\parallel dl \ \ [\text{rad/m}^2] \tag{1.28}$$

with n_e the electron density in cm^{-3}, L the length of the plasma in kpc, $B_\parallel$ the magnetic field component along the line-of-sight in µG. Since the polarization angle Φ is an observable quantity, the RM of radio sources can be derived by a linear fit of Eq. 1.27. RM studies provide magnetic field strengths for about 30 objects, in particular these are of the order of a few µG for non CC GCs (e.g Feretti et al., 1995; Govoni et al., 2006; Bonafede, 2010), and of the order of a few 10 µG for CC GCs (e.g. Perley & Taylor, 1991; Taylor & Perley, 1993).

Another method to derive magnetic field in GCs is by comparing the IC emission from scattering of relativistic electron on CMB photons and the synchrotron emission. From Eq 1.24 we can find the strength of the magnetic fields by deriving U_B. However, there is not a clear detection of IC emission and therefore this method leads to lower limits of the magnetic field strengths. These are about 0.1-0.5 µG, and are obtained combining upper limits on the IC X-ray emission and the measurements of the radio flux density in radio halos (e.g. Rossetti & Molendi, 2004; Wik et al., 2014; Carilli & Taylor, 2002). The magnetic field can be also estimated under the assumption of minimum energy of the non-thermal energy in the ICM, which is the sum of the energy densities in magnetic fields U_B, CR protons U_pr and CR electrons U_el (see Govoni et al., 2002):

$$U_\text{TOT} = U_\text{el} + U_\text{pr} + U_\text{B} \tag{1.29}$$

where the magnetic field energy contained in the source volume V is given by:

$$U_B = \frac{B^2}{8\pi}\Phi V \tag{1.30}$$

which Φ is the *filling factor* (e.g. the fraction of the source volume occupied by the

magnetic field). If k is the ratio between relativistic protons and electrons, then the total energy density of both cosmic rays and magnetic field is:

$$U_{\text{TOT}} = (1 + k)U_{\text{el}} + U_{\text{B}} \tag{1.31}$$

This equation can be also expressed by considering electron energy content as a function of the synchrotron luminosity L_{syn}:

$$U_{\text{TOT}} \propto (1 + k)L_{\text{syn}}B^{-3/2} + \frac{B^2}{8\pi}\Phi V \tag{1.32}$$

The Eq. 1.32 has a minimum energy which is obtained when the contributions of the magnetic field and the relativistic particles are approximately equal (equipartition condition):

$$U_{\text{B}} = \frac{3}{4}(1 + k)U_{\text{el}} \tag{1.33}$$

Assuming $k = 1$ and $\phi = 1$, the equipartition magnetic field can finally be estimated as:

$$B_{\text{eq}} = \sqrt{\frac{24}{7}\pi u_{\text{min}}} \tag{1.34}$$

where u_{min} is the total minimum energy density. Values of magnetic fields obtained with this method are $\simeq 0.1 - 2$ µG (e.g. Feretti et al., 1999). Nevertheless, since the parameters k and Φ are not known a priori, the equipartition value of the magnetic field is uncertain. Fig. 1.7 shows the minimum of the total energy U_{TOT} in a radio source and the corresponding magnetic field B_{eq}.
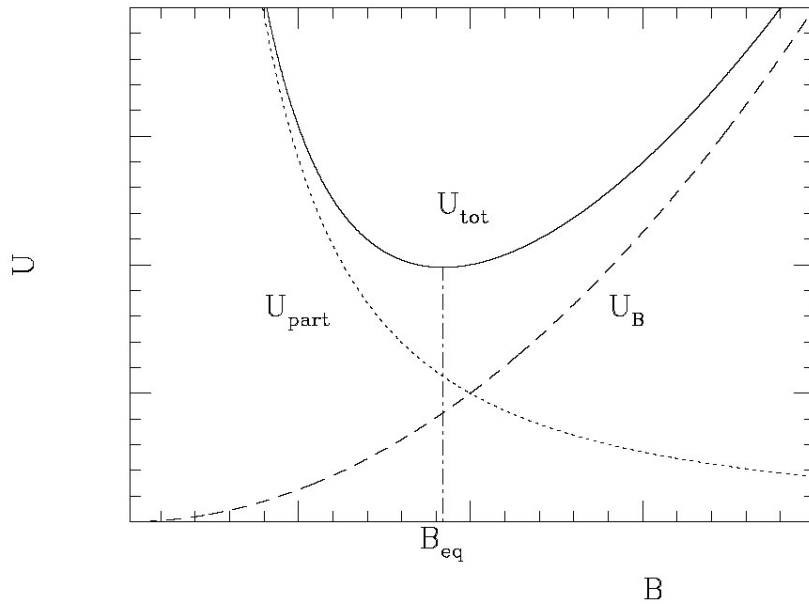
Figure 1.7: $U_{\text{B}} \propto B^2$ is the density energy in magnetic fields, $U_{\text{part}}^{-3/2}$ is the density energy of the CR particles. The minimum of the total energy U_{TOT} corresponds to the equipartition value B_{eq}. From Govoni et al. (2002).

1.4.3 Radio-halo

Radio halos are extended ($\sim 1 - 2$ Mpc) sources at the center of disturbed GCs. They exhibit low surface brightness and fairly follows the distribution of the thermal gas. Radio-halos are generally unpolarized ($< 10\%$), although significant level of polarization has been found in some cases (e.g. Bonafede et al., 2009). Historically, radio halos have been detected in the NVSS[9] (Condon & Kaplan, 1998) and WENSS [10](Rengelink et al., 1997) surveys. More recently, they have been found with GMRT [11](Venturi et al., 2007, 2008), GLEAM [12](Wayth et al., 2015), and LoTSS[13](Shimwell et al., 2017) surveys. Currently there are about 65 discovered radio halos and they are predominately hosted by merging clusters. The connection between radio-halos and merger events is confirmed from both X-ray observations (e.g. Böringer & Schuecker, 2002) and optical studies (e.g. Ferrari, 2003). X-ray morphology of GCs can provide a more quantitative measure of their dynamical state, in particular two estimators commonly adopted are the emission centroid shift w and concentration parameter c. The first one expresses how much the centroid of the X-ray surface brightness moves when the aperture used to compute it decreases in a series of circular apertures centered on the cluster X-ray peak. The centroid parameter c is defined as the ratio of the peak X-ray surface brightness with respect to that of the ambient (see Cassano et al., 2010, for more details).

An important proof of the relation between radio-halos and merging system is given by the so-called "radio bi-modality" (Brunetti et al., 2007, 2009). According to this correlation GCs can be classified into two populations: merging GCs hosting radio halos and relaxed systems without the presence of large-scale diffuse radio sources. Fig. 1.8 shows a WSRT[14] and XMM image of the Coma cluster, which hosts the best example of giant-halo. The multi-frequency study of this cluster, thanks also its high mass and vicinity($z = 0.023$), provides important information of the origin of radio diffuse emission.

Origin of Radio-halos

As we discussed before (Sec. 1.4.1), CR electrons are short-living particles ($t_{\rm loss} \leq 10^8$ yr). The lifetime of emitting electrons is much shorter than the time-scale necessary to CR electrons to diffuse on the radio emitting scale ($t_{\rm diff} > 10^9$ yr).

Two models have been proposed to solve this so-called *slow diffusion problem* (e.g. Brunetti & Jones, 2014):

- *leptonic model*, in which CR electrons are continuously re-accelerated by *magnetohydrodynamics* (MHD) turbulence in radio-emitting region.

- *hadronic model*, in which secondary electrons are produced by hadronic interactions between CR protons and thermal protons of the ICM.

Current observations mostly support the leptonic model as the main mechanism responsible for generating radio halos. A first strong argument against the secondary

---

[9]https://www.cv.nrao.edu/nvss/
[10]https://heasarc.gsfc.nasa.gov/w3browse/all/wenss.html
[11]https://heasarc.gsfc.nasa.gov/W3Browse/all/gmrtas150m.html
[12]http://www.mwatelescope.org/gleam
[13]https://lofar-surveys.org/surveys.html
[14]http://www.epta.eu/telescopes/westerbork.html

model (i.e. hadronic model) comes from γ-ray observations. CR protons are long-living particles and their inelastic p-p collisions with thermal protons produce π_0 and secondary electrons (Sec. 1.4.1). So far, *Fermi-LAT* [15] observations have been found only upper limits to the γ-ray emission of GCs (Ackermann et al., 2010, 2015, 2016).

Another important indicator to understand the particles acceleration mechanism is the observed spectrum of radio-halos. Radio halos have steep spectral indices, $\alpha \simeq$ 1.3. Steeper spectra have been found in few cases (e.g. Brunetti et al., 2008), called *Ultra Steep Spectrum Radio Halos* (USSRHs), and they have spectra steeper than -1.5, which can not be explained in the hadronic scenario. In addition, the main prediction of leptonic models is that the bulk of radio halos should have ultra-steep spectrum, that would make them undetectable at classical radio frequencies, i.e. $\simeq 1.4$ GHz (see Brunetti & Jones, 2014, for a review). Low frequency radio observations with LOFAR [16] have found some other cases of USSRH (Macario et al., 2010; Wilber et al., 2018) and upcoming LOFAR observations will be able to test the predictions of leptonic models. In the re-acceleration scenario, large scale turbulence can be generated by mergers (Vazza et al., 2006, 2017), and the already existing population of relativistic particles, the *seed electrons*, can be produced by radio galaxies, galactic winds, proton-proton interactions, and AGN activity.
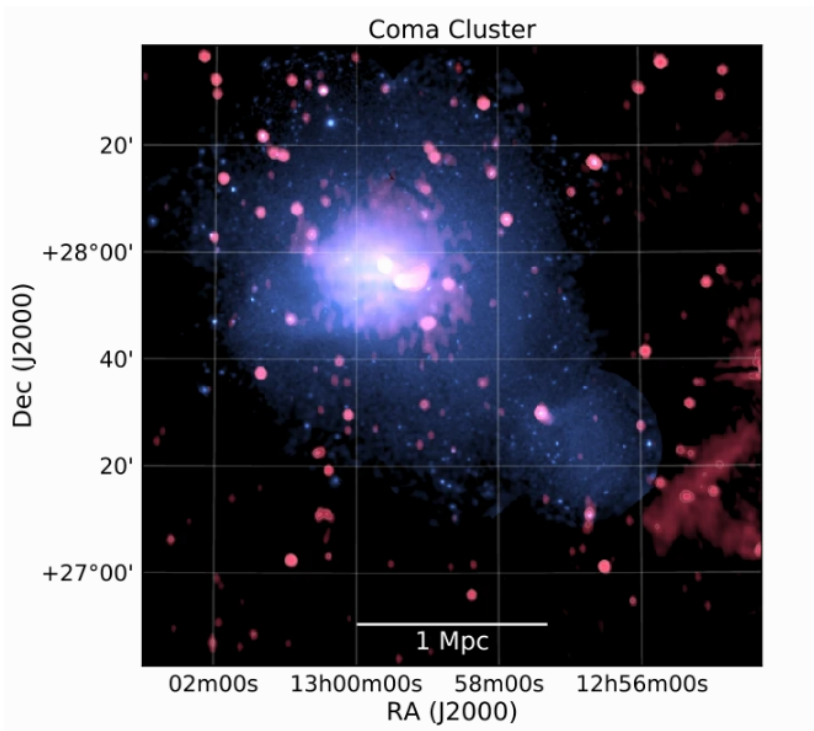
Figure 1.8: WSRT 352 MHz (red) and XMM-Newton 0.4–1.3 keV(blu) of the Coma cluster which hostes a giant halo. From van Weeren et al. (2019).

---

[15] https://fermi.gsfc.nasa.gov/
[16] http://www.lofar.org/

1.4.4 Mini-halo

Radio mini-halos are synchrotron radio source surrounding the radio-loud BCG of cool-core GCs. They have size of $\sim 100 - 500$ kpc and radio powers of $\sim 10^{23} - 10^{25}$W Hz^{-1} at 1.4 GHz. A prototype example of this object is located in Perseus cluster, shown in Fig 1.9, which has an average radius of $\simeq 111$ kpc. The most distant mini-halo is hosted by the Phoenix Cluster($z = 0.596$) (van Weeren et al., 2014). Mini-halos have a 1.4 GHz radio powers of $10^{23} - 10^{25}$ W/Hz, however they are not easy to be detected because AGN lobes emission can be difficult to separate from the mini-halo emission. Nevertheless, a significant number of mini-halo have been discovered (e.g. Gitti et al., 2006; Giacintucci et al., 2014, 2017) and they confirm that mini-halos are associated to cool-core GCs.

Origins of mini-halos

As radio halos, the re-acceleration model and the hadronic-model have been proposed to explain the origin of mini-halos. Turbulence in cool-core galaxy cluster can not be generated by a major merger event. Gitti et al. (2002) proposed a theoretical model in which cooling flow can be a possible source of the needed turbulence.
More recently, the discovery of the morphological connection between mini-halos and cold fronts in some non-major-merging clusters (Mazzotta & Giacintucci, 2008) supports the scenario in which turbulence can be produced by the sloshing motion of the core (ZuHone et al., 2013, 2015).
Bravi et al. (2016) suggested a possible link between AGN feedback and mini-halos, in which the same process that generate mini-halos can balance the radiative cooling in CC GCs.
On the other hand, the hadronic model in mini- halos can not be excluded, therefore the origin of mini- halos is still debated. Differently from radio halos, γ-ray upper limits from the Fermi[17] satellite and MAGIC [18] telescopes are not yet deep enough to support or exclude a purely hadronic scenario (e.g. Ahnen et al., 2016).
Another important discriminator for the different models is the integrated spectrum of mini-halos. In the case of a re-acceleration scenario, spectral break at high frequencies is expected in mini-halo spectrum. However, there are few detection to draw a general trend of the mini-halo spectra.

Very steep radio emission on larger scale in cool-core GCs

With the advent of LOFAR observation, a new zoology of radio sources has been discovered. Even if it was thought that radio halos only form in GC undergoing major merger, recent detection revealed the presence of steep radio emission on Mpc scale in CC GCs (Bonafede et al., 2014; Sommer et al., 2017; Venturi et al., 2017).
In this context, a peculiar case is PSZG139 (Savini et al., 2018) which is the first case of a CC CGs where a mini-halo coexists with steep-spectrum emission outside the core (Fig. 1.10). One explanation can be a situation where a massive cool-core cluster undergoes a minor merger and consequently, the sloshing motion of the core produces emission on cluster-scale. The minor merger has not disrupted the cool-core and the cluster may appear with some level of disturbances, which can be estimated by X-ray

---

[17]https://fermi.gsfc.nasa.gov/
[18]http://www.magic.iac.es/
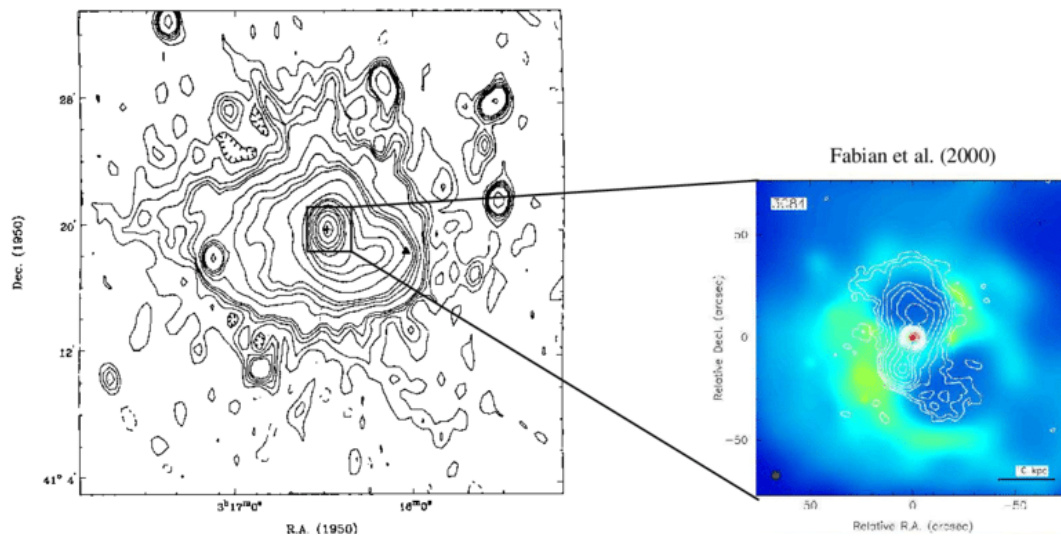
Figure 1.9: *Left panel*: 327 MHz map of the mini–halo emission in Perseus cluster. *Right panel*: X-ray (gray scale) and radio (contours) overlay for the central part of the Perseus cluster. From Gitti (2016).
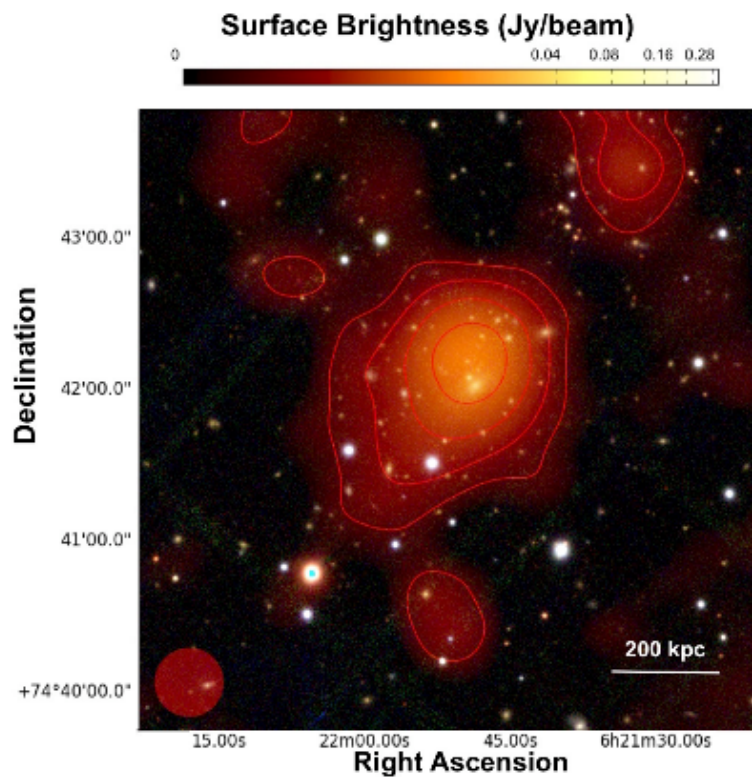
Figure 1.10: Optical emission (*white*) and radio emission from LOFAR at 144 MHz (*red*) of the cluster PSZG139. From Savini et al. (2018).
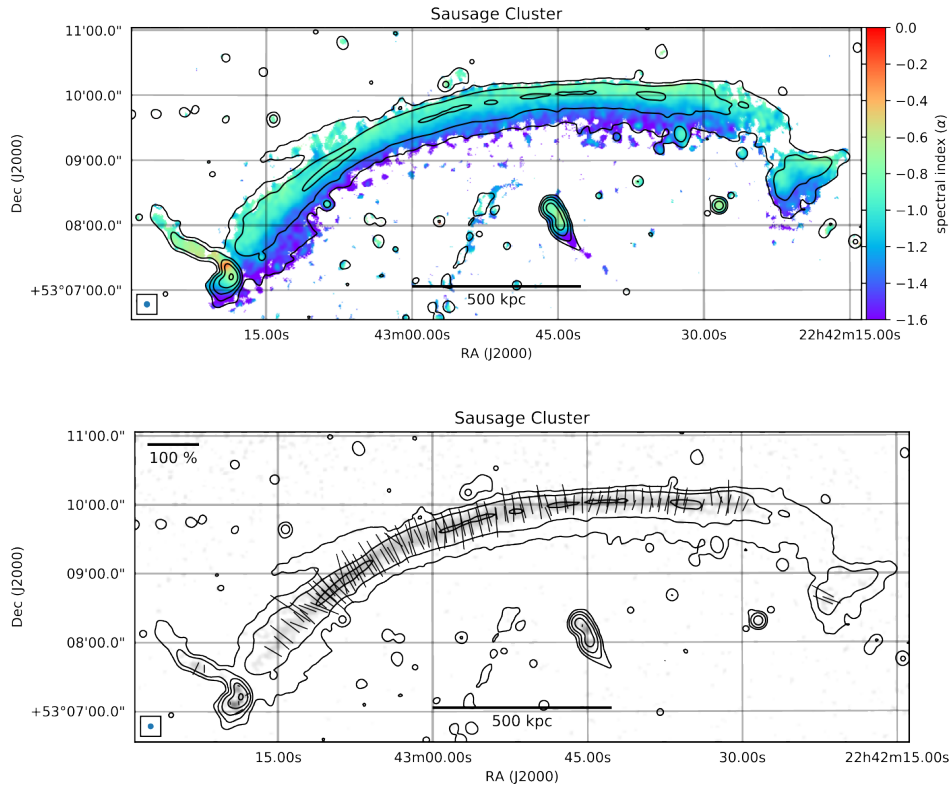
Figure 1.11: *Top panel*: Spectral index maps of Sausage cluster. Colors indicate different spectral index, in particular the Fig. shows an aging of CRs electrons toward the center of the cluster. *Botton panel*: Polarization map of Sausage cluster with electric field vectors of the polarization. From van Weeren et al. (2019).

observations (see Sec. 1.4.3). Since minor mergers dissipate lower energy than major mergers, radio halo spectra are very steep ($\alpha > 1.5$) and they can be observed at low frequencies. Ultra-steep spectrum generated by minor mergers are predicated by some models (e.g. Cassano et al., 2006).

These recent discoveries lead to a new investigation of non-thermal emission in CC GCs with LOFAR observations (Savini et al., 2019), in order to answer new questions opened by this scenario, such as if sloshing motion can create both mini-halos and emission outside the core, and which mechanism for particles acceleration can explain steep spectra.

1.4.5 Radio relics

Radio relics are diffuse radio sources observed in the outskirts of merging GCs. They have typically elongated shapes and large size ($\sim$ 1Mpc). Their morphology suggests a relation with a shock wave seen relatively edge-on, which amplify magnetic fields and accelerate CRs electrons up to relativistic energies. Moreover, X-ray observations confirm the presence of merger shocks connected to these objects. Radio relics are characterized by low surface brightness, steep spectrum ($\alpha > 1$) and high degree of polarization ($\sim$ 30 % a 1.4 GHz), suggesting that the magnetic field is aligned with the shock plane. In Fig. 1.11 is shown the polarization and spectral index maps of the so-called "Sausage" cluster.

The origin of radio relics in GCs is still under debate. The first model proposed to

explain the acceleration mechanism was the *Diffuse shock acceleration* (DSA) theory (Bell, 1978), in which particles are scattered up and downstream the shock, gaining energy when they cross the shock front. According to this theory, the Mach number can be estimated from the radio injection spectral index α_{inj} as:

$$\mathcal{M}_{radio} = \sqrt{\frac{2\alpha_{\mathrm{inj}} - 3}{2\alpha_{\mathrm{inj}} + 1}} \tag{1.35}$$

Since GCs are characterized by weak merger shocks with a $\mathcal{M} \sim 2 - 4$, DSA model predicts very steep energy spectra. However, the synchrotron spectra of some radio relics are much flatter than those expected from the observed shock Mach numbers. Another observational feature against DSA model is the lack of γ-ray emission (Vazza & Brüggen, 2014; Wittor et al., 2017). Indeed, merger shocks may accelerate also CR protons, which undergo to inelastic collision with the thermal gas.

Additional mechanisms for the particles acceleration have been suggested, such as a re-acceleration of a already existing population of relativistic electrons, which can be efficiently re-accelerated by low Mach number shocks (e.g. Bonafede, 2014; van Weeren et al., 2017) .
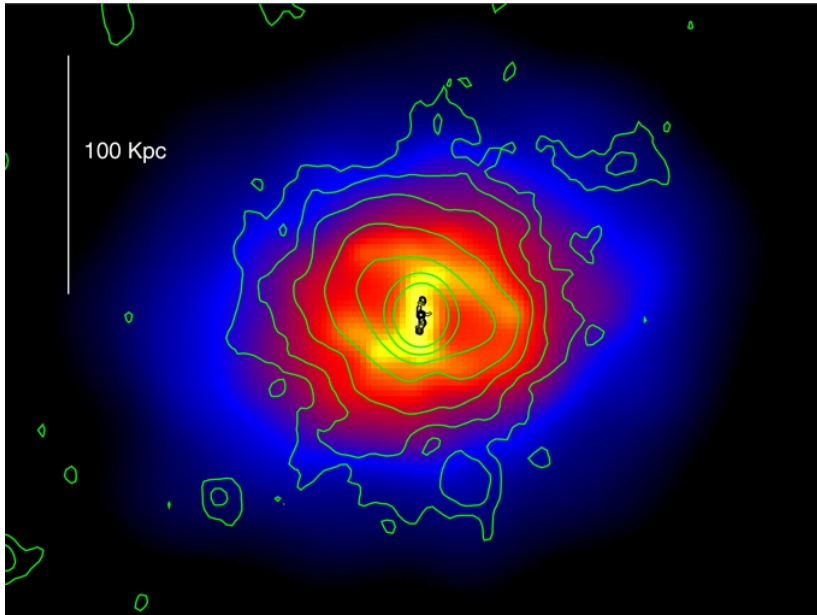
Figure 1.12: 1.4 GHz VLA radio contours (green) at 3″ and 4.8 VLA radio contours at 0.4″ (black) overlaid onto the X-ray *Chandra* image of the central region of RBS797. 1.4 GHz VLA contours show the diffuse mini-halo emission. From Doria et al. (2012).

1.5   This thesis: a new study of the cluster RBS797

In this thesis work, we present a multi-wavelength investigation of the central region of the cool-core cluster RBS797 (z=0.354).

This cluster has been selected for its dense core, for the presence of a mini-halo and by assessing the dynamical state of the cluster (see Sec. 1.4.3). The LOFAR observation of this cluster wants to explore the new scenario of a very steep diffuse emission outside the cool-core. Indeed, as we explained before, one possibility of this new steep detection on larger scale can be due of a minor merger event, which produces sloshing motion of the core and dissipates low energy in the ICM, leading to steep spectra which can be observed in the low frequencies. The high sensitivity and resolution of LOFAR observations provide for the first time a detailed study of the spectral properties of this mini-halo in the low radio frequencies($\simeq 140$ MHz).

RBS797 was widely studied in both X-ray and higher radio frequencies ($\simeq 1$ GHz), as we briefly describe in this section. RBS797 was firstly discovered with ROSAT[19] All-Sky Survey, and a later snapshot Chandra observation revealed the presence of two pronounced X-ray cavities (Schindler et al., 2001). These X-ray depressions with diameters $\simeq 20$kpc confirmed with follow-up Chandra observations, suggesting an interaction between the central radio-loud galaxy and the ICM.

In particular, Doria et al. (2012) confirmed that AGN outflows are capable of balancing the radiative losses, and they estimated the power of the cavity system $P_{\text{cav}} \sim 2.5 \times 10^{45}$erg s^{-1}(see Sec. 1.2.1) and the X-ray luminosity within the cooling-region $L_X = 1.33 \times 10^{45}$erg s^{-1}.

Furthermore, in addition to the X-ray observation, relevant radio discoveries of this cluster have been detected. Radio emission on different orientations has been found with multi-frequency VLA observations (Gitti et al., 2006). From Fig. 1.12, we can

---

[19]https://heasarc.gsfc.nasa.gov/docs/rosat/rass.html

see the 1.4 GHz and 4.8 GHz radio contours overlaid onto a Chandra image, which reveal this peculiar structure. In particular, radio bubbles at 1.4 GHz excavate X-ray depressions, as we can see in Fig. 1.13, instead the innermost 4.8 radio jets are oriented in a direction perpendicular to these cavities.

A possible scenario proposed is that different outbursts correspond to different episodes of the Super Massive Black Hole (SMBH) activity, with a precession of the jet axis of $\simeq 90°$ in 10^7 yr. Doria et al. (2012) support this scenario because they revealed the possible presences of an inner and outer edge by means of unsharp masked images. Indeed, the inner at $\simeq 8''$ from the center can correspond to an intermediate outbursts ejected by the central AGN, and the outer, at $\simeq 16''$, can be associated to an oldest outbursts. However, due to the lack of a detailed morphological and spectroscopic analysis, they could not confirm their detection. The same authors found bright rims surrounding the main system of cavities, which are brightness discontinuities probably produced by the compression of the radio lobes expanding in the ICM, and classified the diffuse emission surrounding the central region of this cool-core cluster as a mini-halo, due to its shape and size comparable to the cooling region.

As discussed above, a detailed morphological and spectroscopic X-ray analysis can lead to the discovery of edges in the ICM. Therefore, in this thesis we focus on researching X-ray brightness discontinuities, such shocks and cold fronts, in order to investigate their possible association with the new radio diffuse emission images of LOFAR observation. Indeed, the presence of a shock or a cold front provides important information of the origin of the mini-halo.
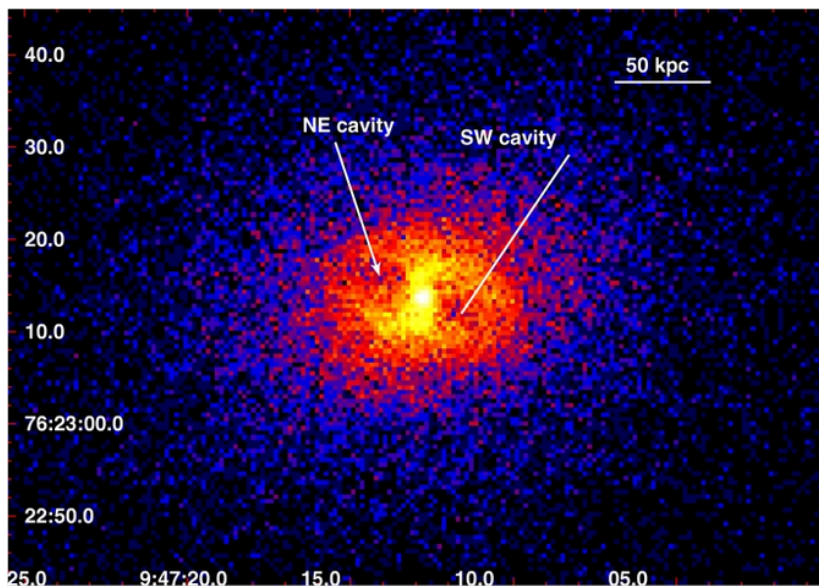
Figure 1.13: Raw Chandra ACIS-S image of RBS 797 in the 0.5–7.0 keV energy band. Two prominent cavities are evident in the northeast-southwest direction. From Doria et al. (2012).

Chapter 2

LOFAR data analysis

LOFAR is the first of a new generation of radio interferometers, exploring for the first time the radio emission between 20 and 240 MHz with arcsecond resolution. Being sensitive to steep and diffuse emission, it is going to increase the detections and properties of diffuse emission in GCs.
In the first section of this chapter we explain the basic concepts of radio interferometry, in the second one we provide an overview of the LOFAR radio telescope and in the third one we describe the techniques used for processing and analysing our data.

2.1 Radio interferometry

The radio astronomy is the study of the celestial emission in the 10MHz - 1THz range. In this frequency range the atmosphere is partially transparent and it is possible to observe the radiation from the ground. From Fig. 2.1 we can see the variation of the atmospheric opacity with the wavelength. In particular, the longest wavelength are blocked due to free electrons in the ionosphere. Therefore, the new generation of low frequencies interferometers, such as LOFAR, which exploring the sources in the 20 and 240 MHz frequency range, need to take account of the effects produced by the ionosphere.
Radio telescopes are ground-based instruments which allow us to detect and study radio sources from the Earth surface. Conventional *single dishes* are constituted by the parabolic reflector antenna, that collects and reflects the radio waves to a receiver, called *feed*, which amplifies and converts them to electrical signals. Recently, radio telescope in the low frequencies have been developed new efficient techniques for *dipole* antennas.

The antenna response to the incoming radiation is represented by its *effective collecting area*, which decreases with increasing distance from the axis of the antenna. For an unpolarized source with a flux density S_ν the total power P_ν received by the antenna is related to the effective area A_e as follows:

$$A_e = 2\frac{P_\nu}{S_\nu} \tag{2.1}$$

In Fig. 2.2 is shown the *power pattern* or *beam* of the antenna that represents the diffraction figure of a point source and it measures the variation of the instrumental response. It is characterized by a *main beam* corresponding to the Airy disc (Airy, 1835) and the so-called minor sidelobes. The angular dimension of the main beam
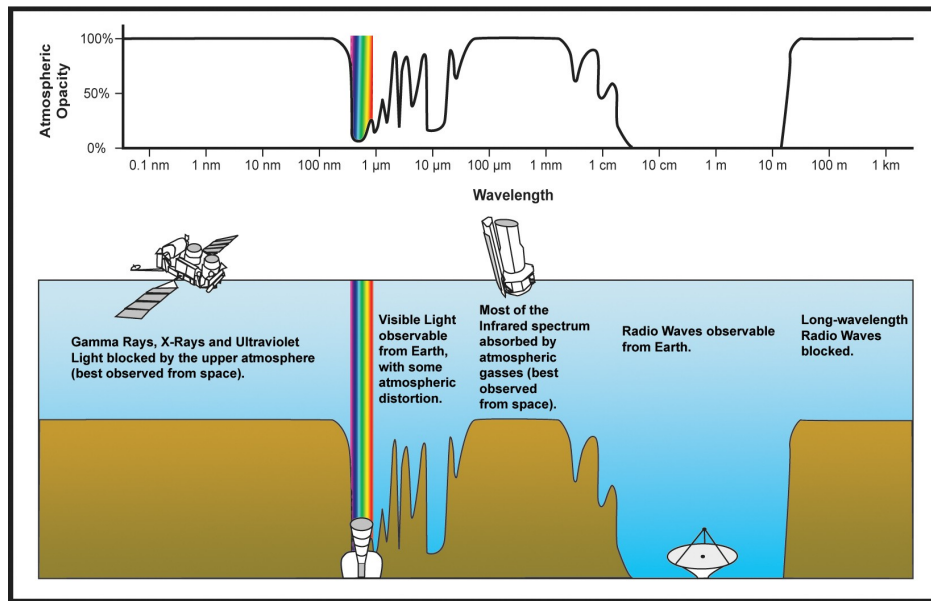
Figure 2.1: The electromagnetic spectrum. Radio waves observable from Earth span the range from 1 THz and 10 MHz. The lowest frequencies are blocked due to free electrons in the ionosphere. From https://commons.wikimedia.org.
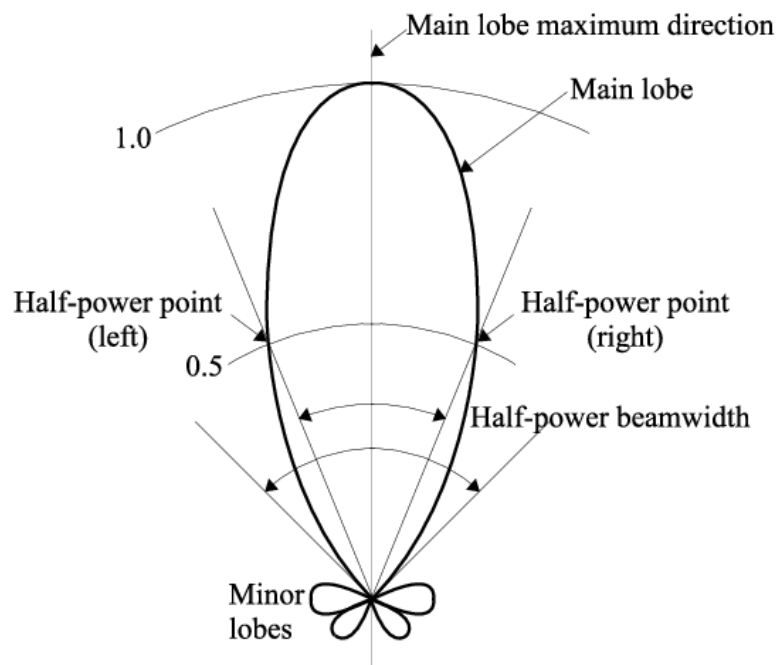
Figure 2.2: Power pattern or beam of a single dish. It is characterized by a main lobe and minor sidelobes. The half-power beam width is the angular dimension of the main lobe. From Zúñiga et al. (2009).

is commonly described by the *half power beam width* (HPBW) and gives the angular resolution of the radio telescope:

$$\theta = 1.22 \, \frac{\lambda}{D} \tag{2.2}$$

where λ is the radio wavelength and D is the the antenna diameter. Better resolution needs larger diameter, however the size of the antenna is restricted by cost and construction issues.

An interferometer is an array of N antennas, called elements, developed to overcomes the low angular resolution of a single dish. An array of N elements can be treated as N(N-1)/2 independent two-element arrays, which are formed by two antennas with a resolving power (i.e. the inverse of the resolution) given by Eq. 2.2 with $D = b$. The baseline of the interferometer b corresponds to the maximum distance between two antennas. In Fig. 2.3 is shown this basic interferometer where two identical antennas are separated by the baseline vector $\vec{b}$ and point the same cosmic source along the direction $\hat{s}$. An incoming wave from a distance point source at angle θ from $\vec{b}$ does not reach the two antenna simultaneously. In particular, the left antenna receives the signal with a *geometric time delay* τ_g, defined as:

$$\tau_g = \frac{\vec{b} \cdot \hat{s}}{c} \tag{2.3}$$

where c is the light speed. The signal voltages V_1 and V_2 for a quasi-monochromatic interferometer (see Condon & Ransom, 2016, for more details) are:

$$V_1 = V cos[2\pi\nu(t - \tau_g)] \quad V_2 = V cos(2\pi\nu t) \tag{2.4}$$

where V_1 takes into account the time delay. These voltages are then combined by the *correlator*, which multiply and time-average them. The output of the correlation is a sinusoidal signal gives by the product of the antennas voltages and $cos(2\pi\nu\tau_g)$ and it is known as *fringe pattern*. The sinusoidal oscillation is due to the motion of the source in the sky with respect to the baseline vector.

However, we can not consider only the geometric delay due to the positions of the antenna, indeed other shifts of the signal path need to take account. These are the phase variation due to the atmosphere, in particular the troposphere at high frequency and the ionosphere at low frequency, as is shown in Fig. 2.3 , the phase shift caused by the wide-bandwidth, and the phase and amplitude shifts generated by the electronics in the receiver system of each antenna. These effects can be corrected by the calibration process as we described in Sec. 2.1.1 .

Since the two antennas of the interferometer are generally identical, the *Field of View* (FoV) of the system is given by the power patter of the individual antenna and it is also called *primary beam* of the interferometer. A larger diameter of the antenna corresponds to a smaller FoV.

If we consider N antennas, the output of the all two-element interferometers can be combined and the response of a point source is the so-called *synthesized beam* or *dirty beam*, which approaches to a Gaussian profile as N increases.

An interferometer does not measure directly the source brightness distribution I_ν but a complex function known as visibility. The visibility is defined as the Fourier transform of the sky brightness:

$$V_\nu(u, v, w) = \int \int I_\nu(l, m) \, e^{-2\pi i[ul + vm + w(\sqrt{1 - l^2 - m^2} - 1)]} \frac{dl \, dm}{\sqrt{1 - l^2 - m^2}} \tag{2.5}$$
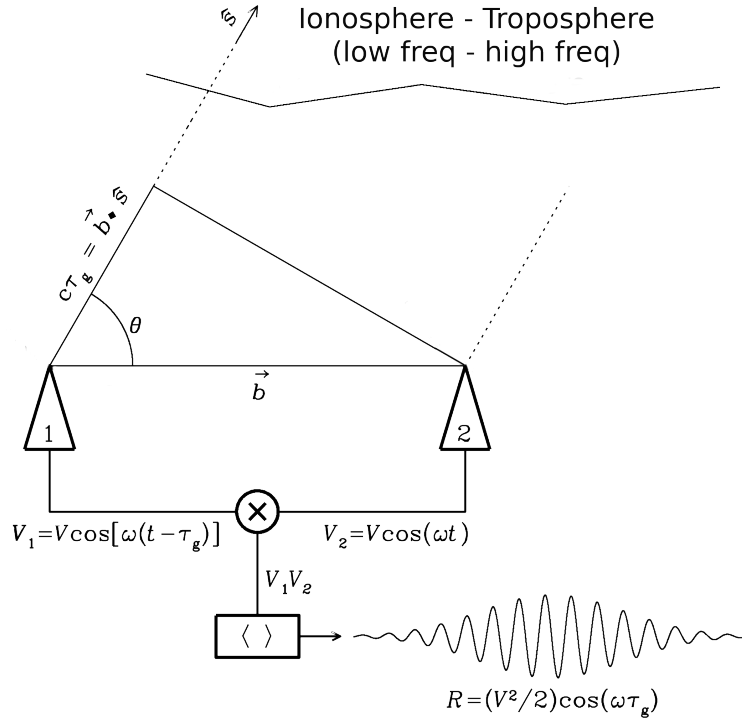
Figure 2.3: Components of a two-element interferometer with a baseline vector $\vec{b}$ observing in a frequency range centered on $\nu = \omega/2\pi$. The output of the correlator is obtained considering the voltage V_2 with a geometric delay τ_g. However, this represents an ideal case, and other effects need to take account, such as the phase shifts on the signal path due to the presence of the atmosphere. In particular, the ionosphere produces variation in the low frequencies regime, while the troposphere affected the high radio frequencies.

where u, v are the baseline vector components,i.e. $u = b_x/\lambda$, $v = b_y/\lambda$,which define a plane, normal to the coordinate w pointing the target direction $\hat{s}_0$.
The w-term, i.e. $2\pi w(\sqrt{1 - l^2 - m^2} - 1)$, is greater than 1 in the case of large FoV, like in LOFAR. While, in the flat field approximation the equation is a 2D Fourier trasform, indeed the w-term is ≤ 1 .
The (l, m) coordinates, with $l = sin\theta_x$ and $m = sin\theta_y$, are called *direction cosines* and define a plane tangent to the celestial sphere. In the small-angle approximation, the direction cosines correspond to the sky coordinates θ_x, θ_y.
A two-element interferometer samples the visibility function in a point of the (u, v) plane and in its Hermitian conjugate, with coordinates $(-u, -v)$. An array of N antennas increases the (u, v) plane coverage, indeed it is composed by N(N-1)/N baselines with different lengths and orientations. Furthermore, in order to fill the (u, v) plane, interferometers use the *aperture synthesis technique* (Ryle & Hewish, 1960), which takes advantage of the Earth rotation motion and therefore traces an ellipse in the uv-plane. Astronomical sources are generally weak sources and their signal can be influenced by the noise coming from a radio telescope.
The lowest emission detected by interferometer is a measure of its sensitivity and it can be derived from the radiometer equation (Wrobel & Walker, 1999):

$$\sigma_T \approx \frac{T_{sys}}{A_e\sqrt{\Delta\nu \ \tau}} \tag{2.6}$$

where $\Delta\nu$ is the observation bandwidth, τ is the integration time, A_e is the effective area, and T_{sys} is the system temperature in Kelvin, which can be expressed as $T_{sys} = T_A + T_R$ where T_R is the receiver noise and T_A is the antenna temperature. The last one, T_A, is not a physical temperature but represents the temperature of an ideal resistor with a power equal to the one received by the antenna.

New generation of radio interferometers, such as LOFAR and SKA [1], are designed to reach high sensitivity by increasing the collecting area.

The *root main square* (RMS) variations in the flux density of the radio images we present in Chap. 3 are given by σ_T.

2.1.1 Basic concepts of calibration

The actual source visibilities $V_{i,j}^{real}$ are modified while reaching the receiver by propagation effects and receiver electronics. The interferometer measures the complex visibility function $V_{i,j}^{obs}$:

$$V_{real}^{ij} = G^i G^j V_{obs}^{ij} \quad \text{with} \quad i, j = 1...N \tag{2.7}$$

where N is the number of the antennas, G^i and G^j are the the gain factors for the antenna i and j, respectively. Since the gain factors are complex quantities as the visibilities, the Eq. 2.7 can be written as:

$$A_{obs}^{ij} e^{-i\phi_{obs}^{ij}} = A_{real}^{ij} g^i g^j e^{-i(\phi_{real}^{ij} + \theta^i - \theta^j)} \tag{2.8}$$

where A^{ij} are the visibilities amplitude, g^i, g^j are the gains amplitude, ϕ^{ij}, θ^i, θ^j are the phase of visibilities and gains, respectively.

The calibration is the process to find the amplitude and phase of the gain. The calibration solutions are derived by the *closure relation* (Thompson et al., 2017), in particular for the phase calibration are necessary only three antennas i, j, k with the corresponding baseline ij, jk and ki :

$$\phi_{real}^{ij} = \phi_{obs}^{ij} + \theta^i - \theta^j$$
$$\phi_{real}^{jk} = \phi_{obs}^{jk} + \theta^j - \theta^k$$
$$\phi_{real}^{ki} = \phi_{obs}^{ki} + \theta^k - \theta^i$$

The sum of these equations leads to:

$$\phi_{real}^{ij} + \phi_{real}^{jk} + \phi_{real}^{ki} = \phi_{obs}^{ij} + \phi_{obs}^{jk} + \phi_{obs}^{ki} \tag{2.9}$$

The gain factors that contain atmospheric and instrumental effects do not appear in the equation which is independent of the antenna gain phases.

A similar relation for the amplitude leads to:

$$\frac{|V_{obs}^{ij}||V_{obs}^{kl}|}{|V_{obs}^{ik}||V_{obs}^{jl}|} = \frac{|V_{real}^{ij}||V_{real}^{kl}|}{|V_{real}^{ik}||V_{real}^{jl}|} \tag{2.10}$$

where we add the antenna l, indeed in this case four antenna are required to resolve the amplitude closure relation.

---

[1]https://www.skatelescope.org/

Classical interferometry using a point-like source calibrator with constant and known flux. Then, a point-like phase calibrator near the source is chosen to correct the phase fluctuations due to the perturbations in the atmosphere.

For the low frequencies arrays, like LOFAR, Eq. 2.5 is also used to find the calibration solutions, however unlike at higher frequencies, we can not use an external phase calibrator. Indeed, the main challenge of LOFAR array is the presence of the ionosphere, which is highly variable in time and we can not simply transfer the solutions from a phase calibrator to the target field. Therefore, a sky model is required to consider the ionosphere effects, that are corrected by the *self-calibration* process, which is described in the next section.

2.1.2   Basic concepts of imaging and self-calibration

As we have seen in Sec. 2.1, the interferometer measures the complex visibility $V(u, v, w)$ which is the Fourier transform of the sky brightness. Then, the brightness distribution $I_\nu(l, m)$ can be obtained by inverse Fourier transform of the visibility.

Even if in the case of large field of view, as we explained before, the the w-term is greater than 1 and we have not a simple 2D Fourier transform of the visibility, for simplicity, we describe the basic of the standard imaging by consider a flat-sky approximation (see Offringa et al., 2014, for more details on the wide-field imaging effects).

Thus, the brightness distribution can be written as:

$$I_\nu(l, m) = \int \int V_\nu(u, v) e^{2\pi i (ul + vm)} du dv \tag{2.11}$$

However, a realistic array has many gaps in the measuring of visibilities and this lead to the *"dirty image"* I_ν^D:

$$I_\nu^D(l, m) = \int \int S_\nu(u, v) V_\nu(u, v) e^{2\pi i (ul + vm)} du dv \tag{2.12}$$

where $S_\nu(u, v)$ is the *sampling function* corresponding to the uv-covarege (S=1 at points where visibilities are measured and S=0 otherwise).

According to the *convolution theorem*, the dirty image is obtained by the convolution between the true distribution and the Point spread function (PSF) response of a point source (for simplicity we omitted the notation on ν, l, m):

$$I^D = I * B^D \tag{2.13}$$

where B is the "dirty beam", defined as the inverse Fourier transform of the sampling function:

$$B = \int S(u, v) e^{2\pi i (ul + um)} du dv \tag{2.14}$$

In order to obtain the real brightness distribution from interferometric data, it is necessary to deconvolve this equation. Imaging can be performed by means of the clean algorithm (Högbom, 1974; Clark, 1980), which is based on the priori assumption that the $I(l, m)$ can be considered as a collection of point sources. It finds the position of the brightest point in the dirty image and subtracts a fraction γ (loop gain) of intensity peak convolved with the dirty beam in that position:

$$I^D - \gamma [CC(\delta) * B] = I^R \tag{2.15}$$

where $CC(\delta)$ are the clean components, which are the delta-function associate to the position of the brightest point, and I^R is the residual map obtained. The operation is repeated several times considering the residual map as the new dirty image. At the end of process, the clean components found are convolved with the clean beam, which is obtained fitting a Gaussian profile to the main lobe of the dirty beam. This last step is known as *restoring*.

The standard calibration which uses bright calibrators is not sufficient to calibrate adequately the data. In particular, there are amplitude and phase residual errors on the data which need to be corrected. Thus, to improve the quality of the final image, the self-calibration process is required.

The self-calibration is an iterative process which uses a sky model from the calibrated visibilities. The first step is to search the clean components from the dirty image and create the sky model. Applying the gain obtained from the residual visibilities, we generate the calibrated visibilities and hence a new dirty image, with a lower noise level. From that, a more accurate sky model is found and the whole process is repeated until the noise reaches a minimum value.

2.2 LOFAR

LOFAR, the low-frequency array (van Haarlem et al., 2013), is a very large radio telescope operating in the frequency range between 10 MHz to 240 MHz (i.e. corresponding to 30-1.2 m). This interferometric array is formed by 51 dipole antenna station, of which 38 are located in the Netherlands and the others 13 *international* are distributed in Europe, precisely in Germany, UK, France, Sweden, Poland and Ireland. There are also other two in-construction stations in Latvia and Italy, the last one will be installed in 2021.

According to the distance of the center of the array (i.e. near the Dutch town of Exloo), LOFAR stations in the Netherlands are classified as *core* stations and the *remote* station. The core consists of a central concentration of 24 stations located within a radius of 2 km from the center stations. The *remote* stations are an approximately logarithmic spiral distribution of the remaining 14 stations extended over an area of about 180 km from the center.

Fig. 2.4 shows the "Superterp " which hosts the six central core stations.

LOFAR antennas do not physically move and the signals from each antenna are combined through a beam-forming technique. The data from all the stations are transported by a high-speed fiber network to a *central processing* (CEP) facility which combines and correlates them, producing the visibilities.

There are two different types of LOFAR antenna, the *High Band Antennas* (HBAs) cover the 110-250 MHz range and the *Low Band Antennas* in the (LBAs) the 10-90 MHz range. However, this range is limited to 30-80 MHz due to strong *radio frequency interference* (RFI). This interference can dominate over the radio signal and then reduce the sensitivity of a radio telescope. For the same reason, the HBA has been optimized to operate in the 110-250 MHz range.

LOFAR antenna can be arranged with different configurations which can be selected by the observer according to the aim of its science. The observation in this thesis used the `HBA_DUAL` configuration.

HBA elements are grouped in 16 dipole antennas elements, laid out in a 4x4 grid to

Figure 2.4: The central Superterp with a diameter of 320 m containing six core stations. From van Haarlem et al. (2013).

form single HBA "tile", whose signals are combined into a "tile" beam. The HBA core stations are distributed over two sub-stations of 24 tiles each. In Fig. 2.5 we show a single HBA tile and a median averaged spectrum for all HBA tiles of a station.

2.2.1   LoTSS

The LOFAR Two-meter Sky Survey, LoTSS (see Shimwell et al., 2017, 2019), is a sensitive, high-resolution survey of the northern sky using the HBA system in a frequency range of 120-168 MHz. This survey reaches high resolution of $\simeq 5''$ and high sensitivity of $\simeq 100$ µJy/beam and the shortest baseline can provide an exceptional study of radio diffuse emission with steep spectral indices in GCs.

Fig. 2.6 compares the high sensitivity and high resolution of LoTSS to those of other recent low-frequency surveys, such as NRAO VLA Sky Survey (NVSS) [2], Faint Images of the Radio Sky at Twenty cm (FIRST) [3], Sydney University Molonglo Sky Survey (SUMSS) [4].

---

[2] https://heasarc.gsfc.nasa.gov/W3Browse/all/nvss.html
[3] https://heasarc.gsfc.nasa.gov/W3Browse/all/first.html
[4] https://heasarc.gsfc.nasa.gov/W3Browse/all/sumss.html
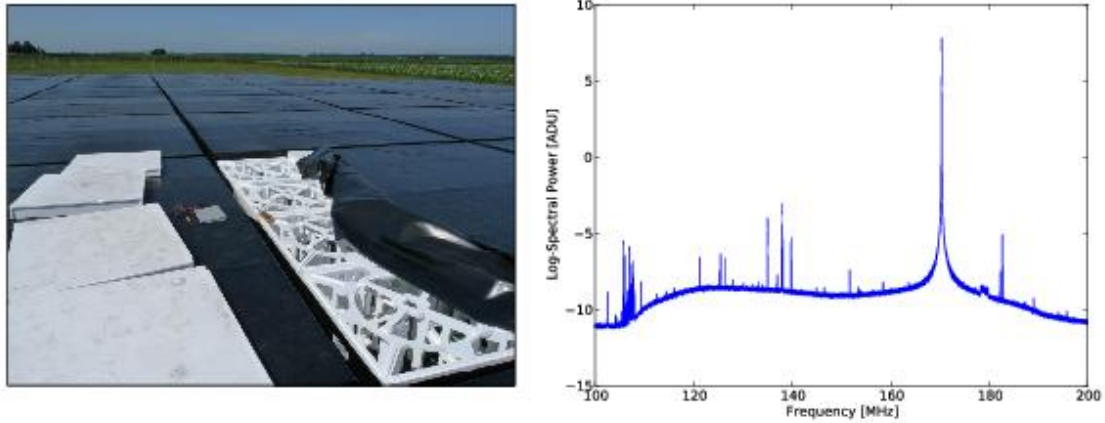
Figure 2.5: *Left panel*: single LOFAR HBA tile. The protective polypropylene foil has been partially removed to expose the actual dipole assembly. *Right panel*: median averaged spectrum for all HBA tiles of a station. RFI sources are clearly visible distributed across the band including the strong peak near 170 MHz corresponding to an emergency pager signal. From van Haarlem et al. (2013).
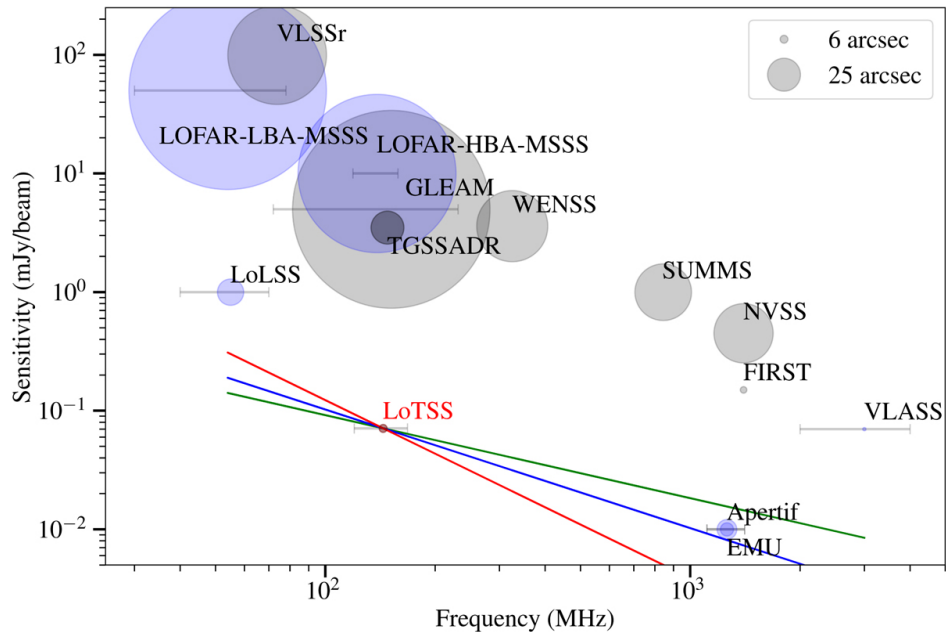
Figure 2.6: Sensitivity, frequency, and angular resolution of LoTSS-DR1 in comparison to a selection of existing wide-area completed (*grey*) and upcoming (*blue*) radio surveys. The lines represent an equivalent sensitivity to LoTSS for compact radio sources with spectral indices of -0.7 (*green*), -1.0 (*blue*) and -1.5 (*red*). From Shimwell et al. (2019).

2.3   Data analysis

The new low frequency observation of RBS797 was performed with the LoTSS observing and processing setup. The `HBA_DUAL` mode was used with 48 MHz bandwidth in the frequency range of 120-168 MHz. Each 8h observation per target was followed by a 10 min observation for a flux calibrator, leading to a total observing time of 8h20m per target.

The standard data reduction for LOFAR data uses two main steps: directional-independent calibration and directional-dependent calibration. These are carried out by automatic pipelines and the first one was already run in Leiden. Therefore, our pre-processed data was ready for the second step.

We describe briefly the direction independent calibration as follows.

Firstly, the target data are mitigated for RFI with `AOFLAGGER` (Offringa et al., 2012), which is an automatic pipeline for detecting and ignoring the contaminated data.

The amplitude calibration is done using an absolute flux density calibrator model from Scaife & Heald (2012). A clock offset correction between the core stations and the remote stations needs to be considered. Then, the gain and clock offset solutions are transferred to the target. The amplitude and phase self-calibration is obtained using a sky model based on catalogues sources of NRAO, VLSS [5], WENSS[6].

Images at medium resolution and high resolution are produced with `WSClean` (Offringa et al., 2014) to detect sources with the PYthon Blob Detector and Source Finder, PYBDSF (Mohan & Rafferty, 2015) software and they are subtracted directly from the visibilities using the clean component models (see Sec. 2.1.2).

The two different resolution images are produced in order to subtract both extended and compact sources and obtain the visibility (uv) dataset for performing the direction dependent calibration.

2.3.1   DDF calibration

Our uv-dataset was formed by 24 bands (120-168 MHz) and it was ready to run the Direction Dependent Facet (DDF) pipeline (Shimwell et al., 2019). We used 23 bands since the last file was corrupted.

As we discussed before, a dependent calibration is necessary because the visibilities are often affected by the so-called *direction-dependent effects* (DDEs), which need to take account in the case of large array. A first effect is the distortions due to the ionosphere, which produces phase fluctuations which differ from station to station. A second effect is related to small differences in station beam models since LOFAR has no moving part. To correct for all the DDEs, the sky seen by the interferometer can be tessellated in "facet", as is shown in Fig 2.7. The number of the facets depends on the bright sources in the FoV, which are used to calibrate phase and amplitude in each facet.

In Fig. 2.8 we evidence the facet that includes RBS797.

The procedure to find the solutions for the DDEs is not a simple, and many technical challenges had to be overcome.

The `ddf pipeline` is a very fast and accurate pipeline which produces images with a resolution of 6″ and 100 μJy/beam. A sky model is created to define 45 facets, then the pipeline solves the DDEs using the `kill MS` algorithm (Smirnov & Tasse, 2015), which

---

[5]https://heasarc.gsfc.nasa.gov/W3Browse/all/vlss.html
[6]https://heasarc.gsfc.nasa.gov/w3browse/all/wenss.html

provides an amplitude and phase solution of the data for each facet. To improve the accuracy of the flux density estimations the *bootstrapping technique* is performed, which uses the VLSS and WENSS catalogues (Hardcastle et al., 2016). The deconvolution is done by the synthesises of a single image with the DDFacet imager (Tasse et al., 2018). For more details of the steps of the pipeline see Shimwell et al. (2019).

2.3.2 Extraction and self-calibration

The output of the DDF pipeline is the whole field of view of LOFAR HBA observations. If one is interested in a specific target rather than in the whole field of view, it is possible to obtain ad-hoc solutions in a specific direction using the procedure of extraction and self-calibration (Van Weeren 2020, in prep).

We select a region of $1' \times 1'$ with ds9 centred on the cluster and all sources outside this region are subtracted from the visibility data using the DDE calibration solutions. The top panel of Fig. 2.9 shows the extracted image before the self-calibration and the bottom panel the last image obtained after this iterative process. From these images, it is evident the improvement on the quality of the image thanks to the self-calibration cycles.

LOFAR HBA beam model presents inaccuracies, and the errors can propagate into the self-calibration solutions. The facet dependent PSF can have different amplitude corrections to the other. This leads to uncertainties in the measurement of the flux density in the images produced.

To rescale the LOFAR flux we can use the TIFR GMRT Sky Survey, TGSS [7], comparing the same point sources. We measured the flux of both images and we found that these are consistent.

---

[7]http://tgssadr.strw.leidenuniv.nl/doku.php
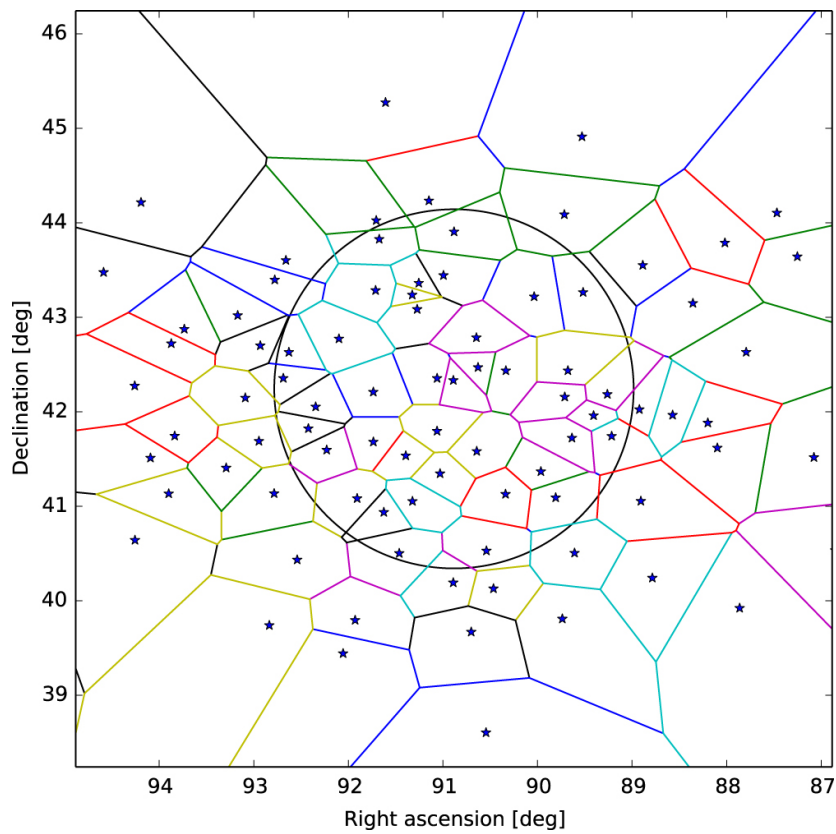
Figure 2.7: Example of tessellation of the Toothbrush cluster field. The black circle indicates the HPBW of the station beam at 150 MHz. Stars indicate the position of the bright sources. From van Weeren et al. (2016).
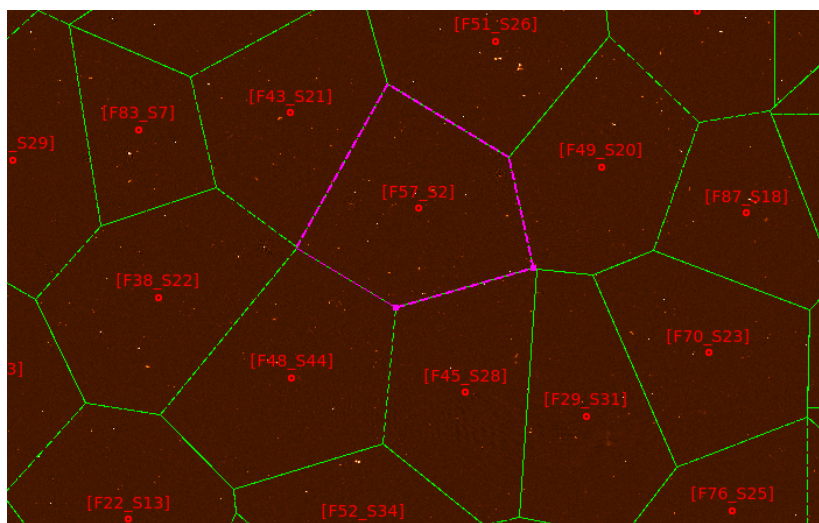
Figure 2.8: Tassellation into faced by the DDF pipeline. The image is zoomed in the facet (*magenta*) that includes RBS797.
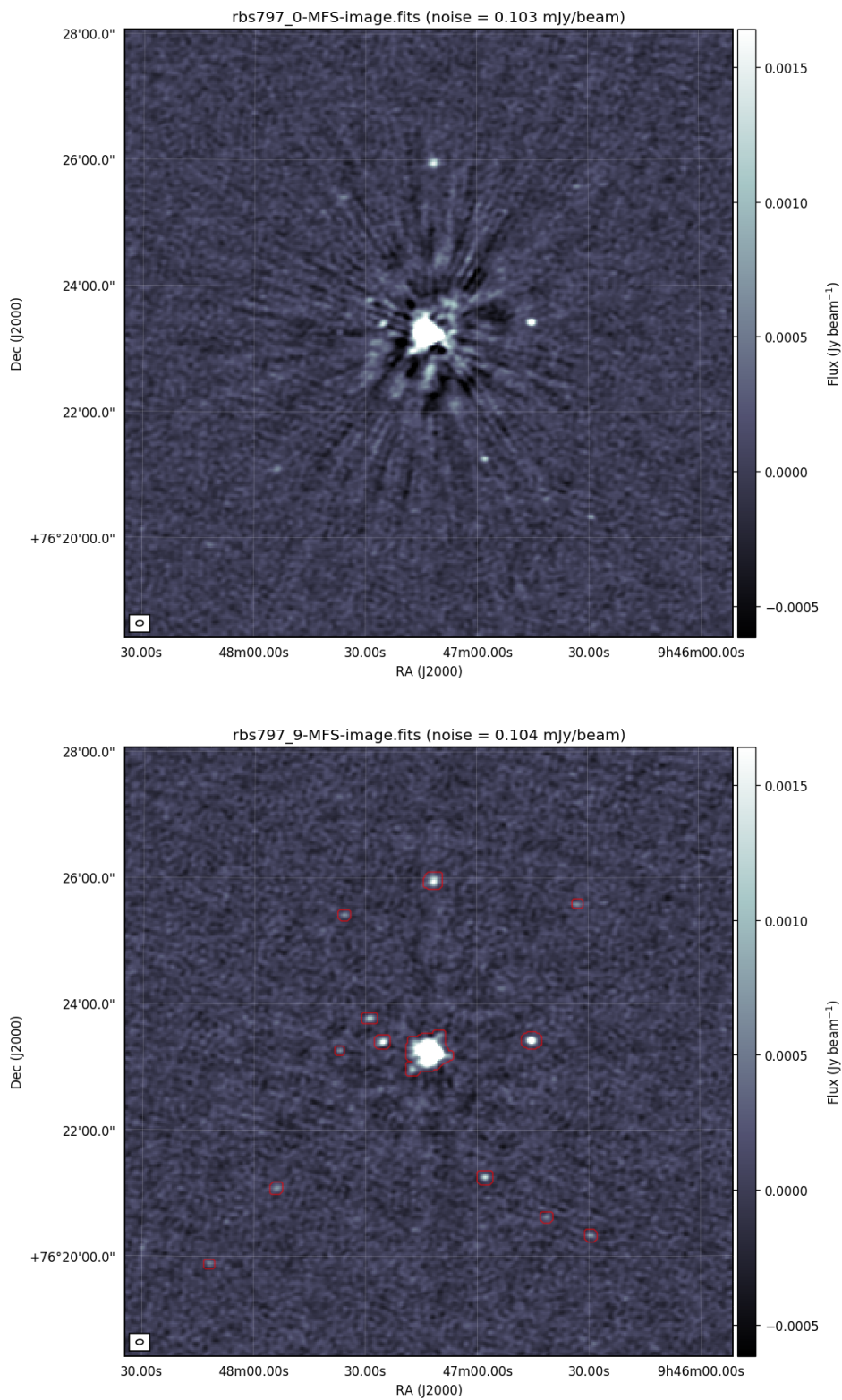
Figure 2.9: *top panel*: Image obtained from extraction. The beam size is $4.7'' \times 6.8''$ *bottom panel*: Image produced after the last cycle of self-calibration. The beam size is $4.6'' \times 6.8''$.

2.3.3   WSClean

As we have evidenced, the imaging was performed with `WSClean` (see Offringa et al., 2014, for details). The abbreviation means "w-Stacking Clean" because of this fast algorithm taking account of the w-term. Indeed, in the case of large FoV as in LOFAR, the two-dimensional Fourier transform in Eq. 2.5 it can not be used and the w-coordinate is not zero.

The Högbom clean algorithm discussed in Sec. 2.1.2 considers the sky as a collection of point sources. An improvement of this method for extended objects is to use a multi-scale approach (Cornwell, 2008), in which the sky is composed by components with different angular scales. `WSClean` performs efficiently the multiscale deconvolution. We describe the main parameters of this algorithm:

- `robust`: this parameter changes the weighting of the visibilities. Typical values are between -1 and 1. A robust value of -2 produces the most uniform weighting on the uv-plane and generally, the longer baselines result with more weight, leading to a better resolution. A robust parameter of 2 gives approximately equal weights to all the visibilities, providing a lot of weighting towards the short baseline and decreasing the resolution.

- `uvtaper`: This parameter multiplies the uv-weights with a Gaussian function. It can be used to reveal extended emission decreasing the weight of long baselines.

- `uvrange`: this parameter changes the data selection removing the short or the long baselines. Long baselines increase the resolution but decrease the sensitivity to the diffuse emission.

Chapter 3

Results from LOFAR observations

In this chapter, we present the radio results obtained during this thesis work. In the first section, we show the low resolution and the high resolution LOFAR images of RBS797. In order to properly study the diffuse emission of the cluster, we combined the new LOFAR images at 140 MHz and VLA archival observation at 1.4 GHz and we performed the spectral index analysis, presented in the second section. From the spectral map and spectral radial profile, we found a flattening of the spectra index toward the external region of the cluster.

3.1 New LOFAR observation

The high sensitivity and resolution of LOFAR array provide excellent imaging of diffuse radio objects and allows us to detect new properties of these sources in the low frequency range.

The new LOFAR observation of RBS797 lets us to investigate the presence of steep radio emission extending beyond the mini-halo region. Indeed, as we discussed before, ultra-steep ($\alpha \simeq -1.7$, $S_\nu \propto \nu^\alpha$) diffuse radio emission on Mpc scale in cool-core GCs have been recently discovered (Savini et al., 2019, 2018; Raja et al., 2020). Motivated by this new result, we created a low resolution image and a spectral index map (Sec. 3.2). Since previous VLA observations have detected the emission of two radio lobes filling the X-rays cavities, we produced the high resolution image to reveal them in the low radio frequencies.

The low resolution image was obtained changing the Briggs weighting of visibilities in `WSClean`. As we explain in Sec. 2.3.3, different robust values provide images with different resolution. We used a `robust` $= -0.5$, which gives uniform weighting to the baseline visibilities and generally leads to a better resolution.

In Fig. 3.1 we show the low resolution image with a restoring beam of $4.7'' \times 6.9''$ and RMS noise of 132 μJy/beam. Black contours are spaced by a factor of 2 starting from $3 \times$ RMS noise. The radio flux density computed inside $3 \times$ RMS contours is 186 ± 28 mJy, whose flux density errors Δ_S is estimated as:

$$\Delta_S = \sqrt{(\sigma_c \times S)^2 + \mathrm{RMS}^2 \times n_{\mathrm{beam}}} \tag{3.1}$$

where n_{beam} is the number of beams in the source area. The systematic calibration error on the flux density is indicated as σ_c, whose value is typical 15% for LOFAR HBA observations (Shimwell et al., 2019) and 5% for VLA observations (Condon et al., 1998).

Figure	robust	beam	RMS	$S_{140\text{MHz}}$
		($''$)	(µJy/beam)	(mJy/beam)
Fig. 3.1	-0.5	4.7×6.9	132	186 ± 28
Fig. 3.2	-2	2.4×3.3	448	158 ± 24

Table 3.1: Restoring beam, RMS and flux density of the high resolution image and the low resolution image obtained changing the `robust` parameter in `WSClean`. Fluxes are measured inside $3\times$ RMS contours.

From this radio map, we measured the extension of the diffuse emission corresponding to $\simeq 30''$, i.e 150 kpc, in the north-south direction, and of $\simeq 40''$, i.e. 200 kpc in the east-west direction.

Gitti et al. (2006) have previously detected with VLA observation a mini-halo with steep spectrum extended on a scale of hundreds of kpc. Therefore, the diffuse emission at 140 MHz can be associated to the mini-halo emission surrounding the cool-core cluster. However, the low resolution image does not show any sign of emission on Mpc scale, as recently found in clusters that hosts a cool-core. In particular, we compare our undetected emission with that revealed by Savini et al. (2018). To derive the upper limit in according to the detection of these authors, we estimated it considering a region of 1 Mpc, and imaging the data at a resolution of $26'' \times 28''$ with RMS=140µJy. We obtained an upper limit on the flux density, computed at $3\times$ RMS, of $\simeq 5.4$ mJy, which leads to a radio power at 140 MHz of $\simeq 1.4 \times 10^{24}$ W/Hz. Comparing this upper limit with the radio power on the diffuse radio emission measured by Savini et al. (2018), i.e. 4.4×10^{24} W/Hz, we can conclude that in our case there is not extended radio emission outside the mini-halo.

A `robust` $= -2$, gives uniform weighting on the uv-plane and allows us to obtain the high resolution image shown in Fig. 3.2. This image has a restoring beam of $3.3'' \times 2.4''$, the RMS noise of 448µJy/beam and the flux density inside $3\times$RMS contours corresponds to 158 ± 24 mJy. As we expected, we revealed the presence of two radio lobes which extend to $15''$, i.e 75 kpc, in the northeast-southwest direction. The high resolution image does not provide details of the central AGN.

We report the main quantities of the low resolution image (Fig. 3.1) and high resolution image (Fig. 3.2) in Tab 3.1.
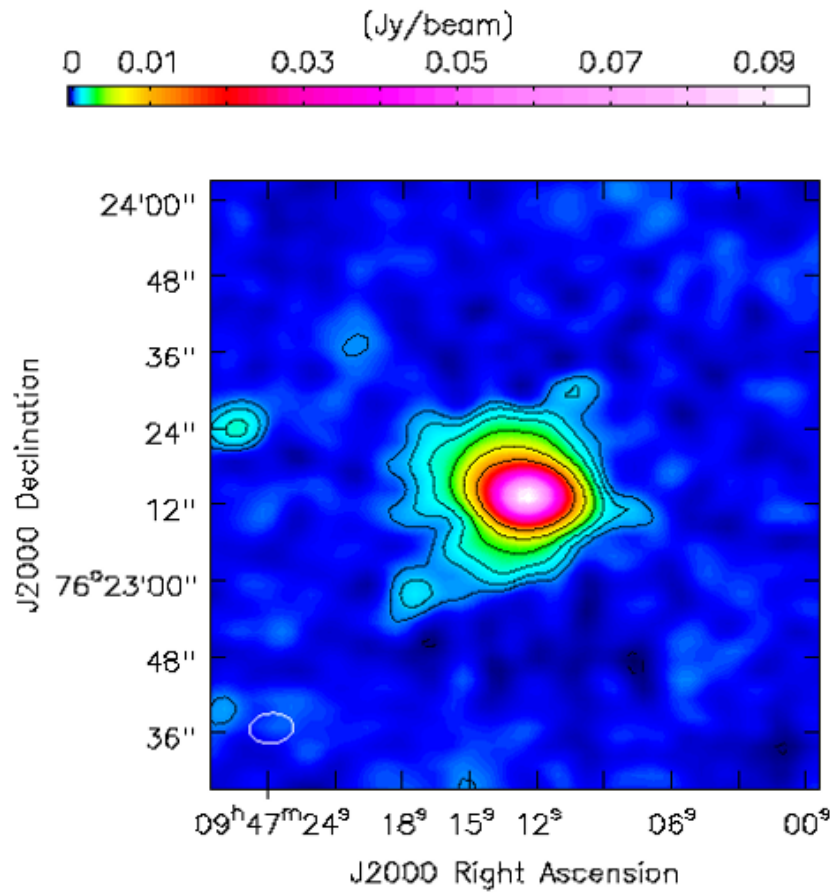
Figure 3.1: Low resolution image of the cluster at 140 MHz. Contours (*black*) are spaced by a factor of 2 starting from $3 \times$ RMS, where RMS$= 132\mu$Jy/beam. The restoring beam of $4.7'' \times 6.9''$ is shown in white. The first negative contour is dashed.
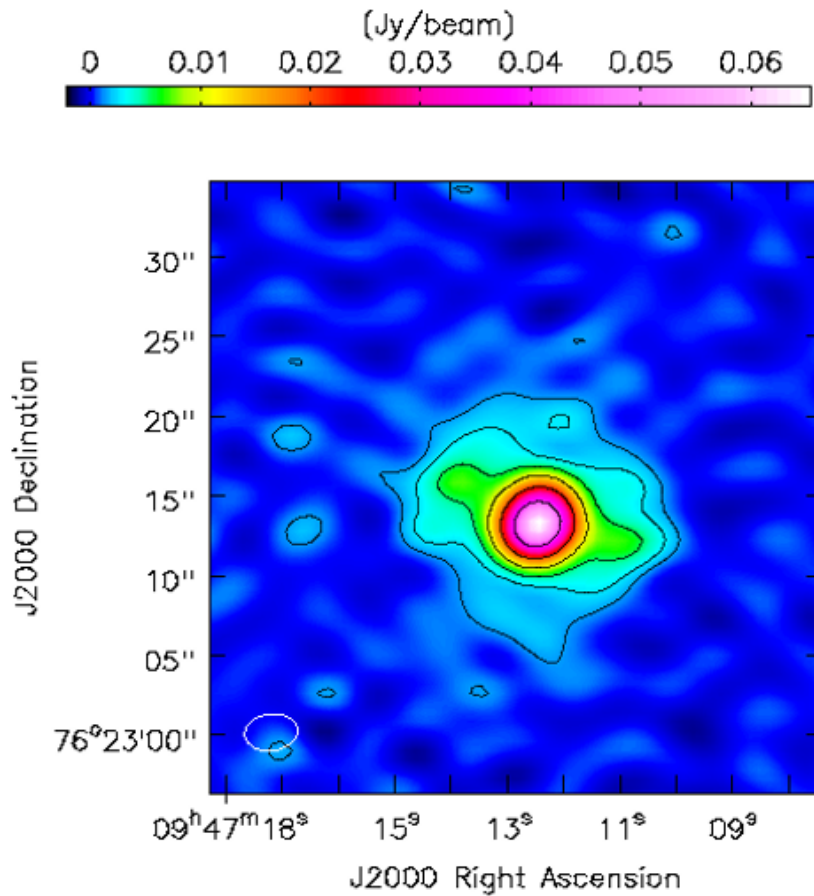
Figure 3.2: High resolution image of the cluster at 140 MHz. Contours (*black*) are spaced by a factor of 2 starting from $3 \times$ RMS, where RMS= 448μJy/beam. The restoring beam of $2.4'' \times 3.3''$ is shown in white. The first negative contour is dashed.

3.2   Spectral index analysis

The spectral index analysis provides information on the acceleration mechanism of relativistic particles emitting synchrotron radiation. Mini-halos are characterised by steep radio spectrum ($S_\nu \propto \nu^\alpha$, with $\alpha < $ -1) and hence, they are brighter at lower frequencies. The new LOFAR observation allow us to investigate the spectral properties of the diffuse radio emission in RBS797.

We produced the spectral index map between 1400 MHz and 140 MHz combining the LOFAR observation with the existing VLA data in C-array. In order to be consistent between the two observations, we set uniform weighting and matched their uv-range. We chose the uv-cut parameters considering the shortest and the longest baselines of the observations, which correspond to `minuv − l = 160λ` and `maxuv − l = 50000λ`. Since LOFAR image presents a phase-shift of the center respect to the VLA image, we aligned the two images before computing the spectral index, which is described as follows. Using `uvtaper = 4″` we obtained the image at 140 MHz with a beam-size of $4.3″ \times 4.5″$ and the image at 1400 MHz with a resolution of $3.2″ \times 4.3″$. Therefore, through the task `imsmooth` in `CASA`, we convolved the images with a circular PSF of $5″$ and regridded to identical pixel size with the task `imregrid`. The 140 MHz and 1400 MHz images are tabulated in Tab. 3.2 and they are shown in Fig. 3.3 and in Fig. 3.4, respectively. From these images we observe that the VLA diffuse emission covers a larger scale than the LOFAR radio emission, especially considering the $3 \times$ RMS radio contours in the north-south direction. The maximum radius of the 1400 MHz emission in this direction is $\simeq$ 190 kpc, instead LOFAR diffuse emission extends to $\simeq$ 136 kpc. Before combining the two images with the task `immath`, we have masked out pixels values below $3\times$ RMS radio noise. The spectral index map is obtained using the standard expression [1]:

$$\alpha = \frac{\log(S_{1400\text{MHz}}/S_{140\text{MHz}})}{\log(\nu_{1400\text{MHz}}/\nu_{140\text{MHz}})} \tag{3.2}$$

and the spectral index error is estimated as:

$$\Delta\alpha = \frac{1}{\left|\ln\frac{\nu_{1400\text{MHz}}}{\nu_{140\text{MHz}}}\right|} \times \sqrt{\left(\frac{\Delta S_{1400\text{MHz}}}{S_{1400\text{MHz}}}\right)^2 + \left(\frac{\Delta S_{140\text{MHz}}}{S_{140\text{MHz}}}\right)^2} \tag{3.3}$$

where errors on the flux densities are calculated as in Eq. 3.1. The spectral index map and the corresponding error map are shown in in Fig. 3.5 and Fig. 3.6, respectively. From these maps, we estimated a spectral index in the inner region (i.e. 12 kpc from the center) of $\alpha \simeq -0.94 \pm 0.07$ and it gradually becomes flatter toward the external regions. They also highlight a steepening of the spectral index in the regions which correspond to the radio lobes, with $\alpha \simeq -1.04 \pm 0.07$. Spectral index of mini-halo should present steep spectra as the radio halos, however few detailed studies exist so far. Indeed, high resolution in the low frequencies are required to better understand the spectral properties of the objects. A prototypical example is the one found in the Perseus cluster, which presents a steep spectrum with $\alpha = $ -1.4 and a progressive steepening with increasing distance (Gitti et al., 2003). In the mini-halo of RBS797, we do not observe this steepening of the spectral index. To better quantity the trend, we have computed a spectral index profile analysis, explained in next subsection.

---

[1]To compute the spectral index in our work, we adopted a different convention of Eq. 1.21, and we used $J(\nu) \propto \nu^\alpha$.

Figure	ν	beam	RMS	S
	(MHz)	($''$)	(μJy/beam)	(mJy/beam)
Fig. 3.3	140	5×5	258	183 ± 28
Fig. 3.4	1400	5×5	27	25.4 ± 1.3

Table 3.2: Restoring beam, RMS noise and flux density of the 140 MHz and 1400 MHz images which are convolved in a circular beam of $5'' \times 5''$. Flux densities are measured above $3\times$ RMS contours.
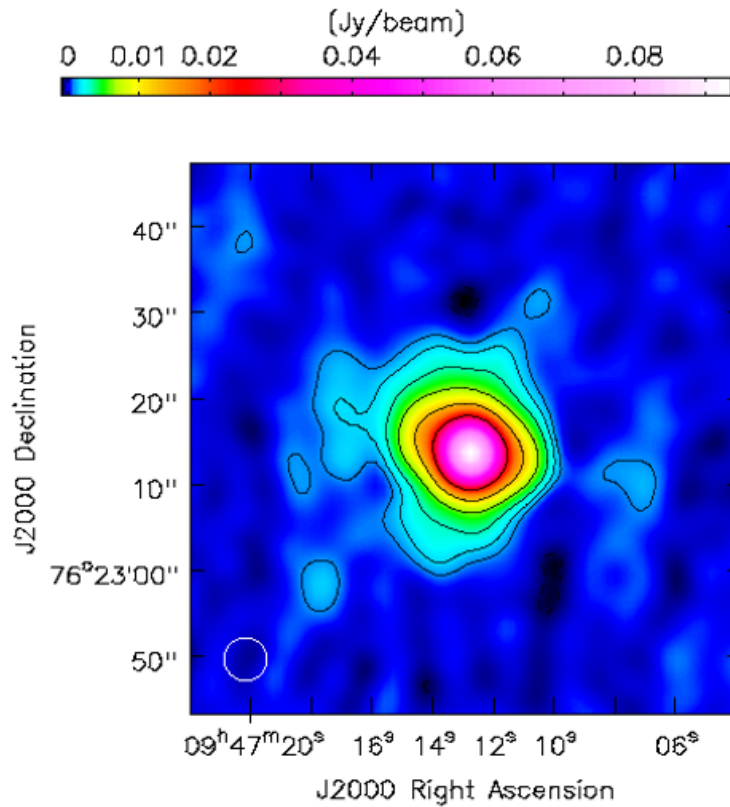
Figure 3.3: Image of the cluster at 140 MHz convolved with a circular beam of $5''$ (*white*). Contours (*black*) are spaced by a factor of 2 starting from $3 \times$ RMS, where RMS= 258 µJy/beam.The first negative contour is dashed.
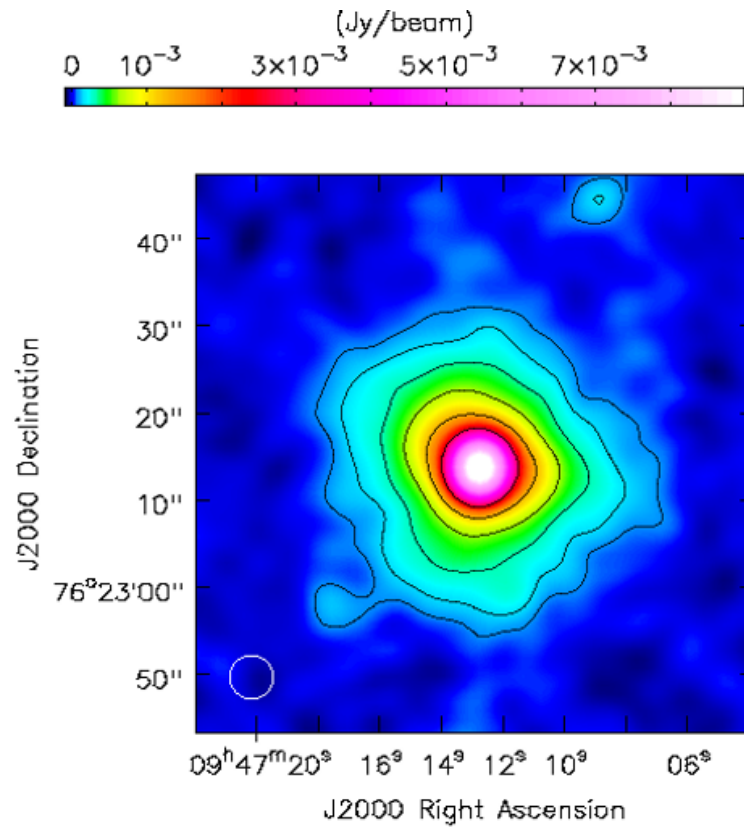
Figure 3.4: Image of the cluster at 1400 MHz convolved with a circular beam of 5″ (*white*). Contours (*black*) are spaced by a factor of 2 starting from 3×RMS, where RMS= 27 µJy/beam. The first negative contour is dashed.
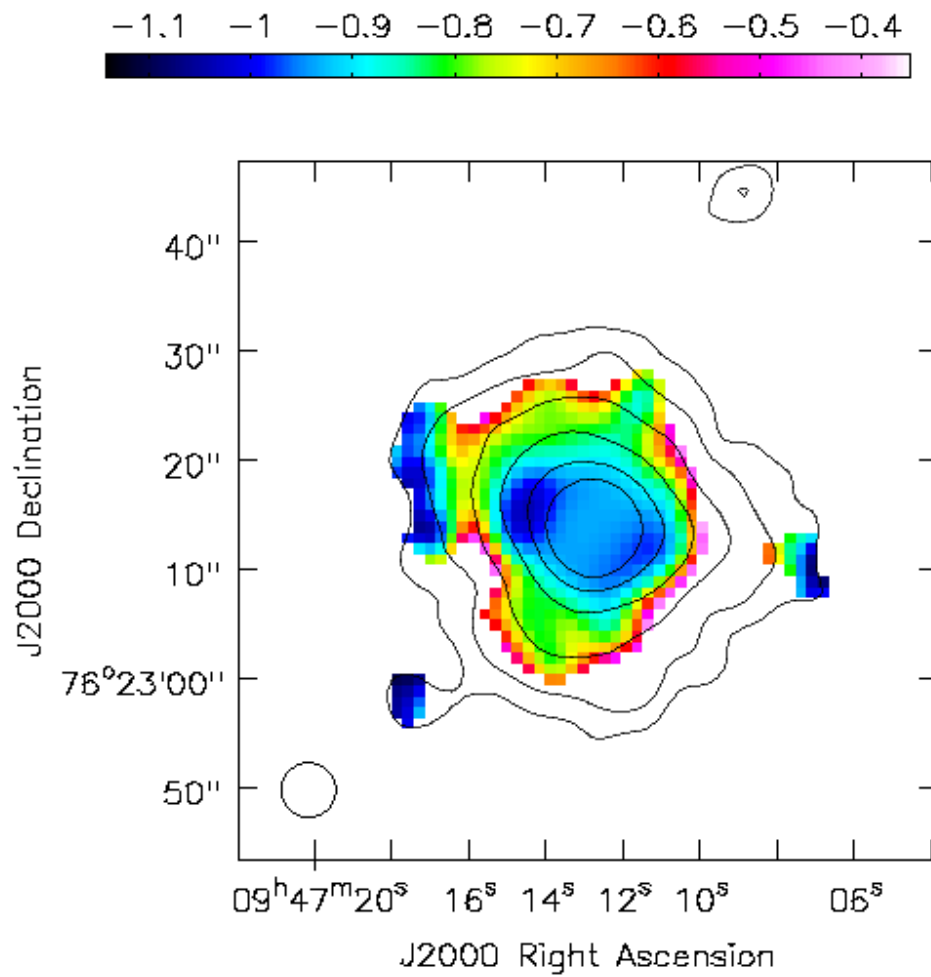
Figure 3.5: Spectral index map of RBS797 between 140 MHz and 1400 MHz at a resolution of $5'' \times 5''$ overlaid on the $3 \times$ RMS VLA contours (*black*).
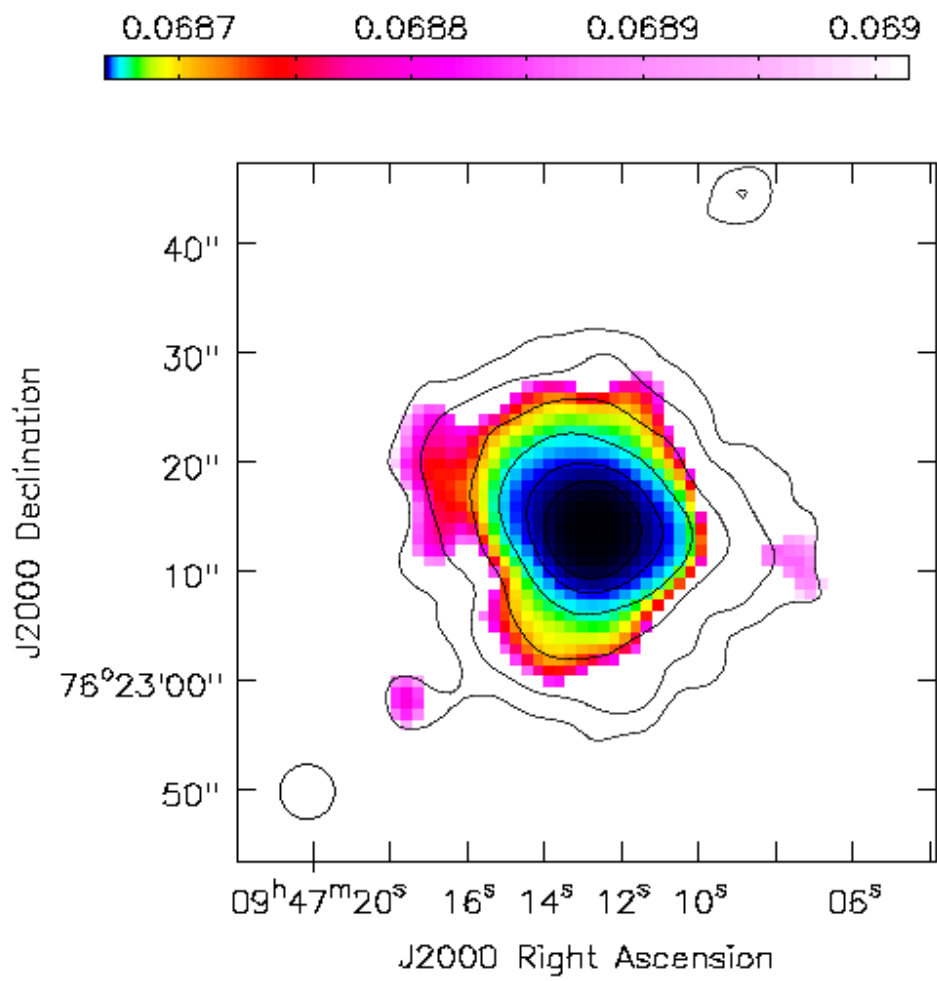
Figure 3.6: Spectral index error map corresponding to the map in Fig. 3.5.

3.2.1 Spectral index profile

Thanks to the high sensitive of LOFAR array, we could create a spectral index profile of the mini-halo. Before the advent of the low frequency radio observations, few spectral index radial studies of these objects have been carried out. As we discussed before, a relevant example is the analysis of the radial spectral steepening of the mini-halo in the Perseus cluster (Gitti et al., 2002)

To produce the spectral index profile, we have measured the flux densities inside six concentric annuli centered on the cluster, RA(J2000): 09h47m12.7s, DEC(J2000)76° 23′ 13.6″, whose thickness dr was chosen to be half of the beam size, as is shown in Fig. 3.7. We measured the flux density from each annulus and the corresponding error (Eq. 3.1). Since LOFAR emission is less extended than the VLA emission, in the last annulus we estimated the upper limit of LOFAR flux density. In particular, S_{up} is given by:

$$S_{\mathrm{up}} = 3 \times \mathrm{RMS} \times A_{\mathrm{annulus}} + S_{\mathrm{L}} \qquad (3.4)$$

with S_{L} the LOFAR flux density of the last annulus, RMS is 27 μJy/beam and A_{annulus} is the area, measured in beam units, corresponding to the part of the annulus in which we do not detect the emission. Since the flux density below $3 \times \mathrm{RMS}$ in respective images were masked, we gave a lower limit on the flux obtained, and it corresponds to 1.3 mJy. Therefore, the interval values of the flux density in the last annulus is [1.3 mJy,149.6 mJy]. The flux density profile declines from the centre to the outer regions of the cluster for both frequencies, as we show in Fig. 3.8, in particular S_{1400MHz} is indicated in red colours, S_{140MHz} in blue colours.

Knowing these quantities, we computed the spectral indices using Eq. 3.2 and their errors with Eq. 3.3. From the lower and upper limit of the flux density, we calculated the lower and upper limit of the spectral index[2], which correspond to $[-2.06, 0.06]$. In Tab. 3.3 we report the inner and outer radius of each annulus, the averaged radius, the flux densities, and the spectral indices. The flattening of the spectral index in the outer regions which we observed from the spectral index map, is also evident in the spectral index profile, which is shown in Fig. 3.9. Therefore, we had a further check that the diffuse non-thermal emission in RBS797 presents a spectral index which becomes flatter moving outwards from the cluster center. A possible explanation is the presence of a shock wave propagating in the outer region of the cluster, which accelerates particles to higher energies. We investigate this scenario with X-ray analysis, reported in Chap. 4. From this study, we confirm that this cool-core GC does not suggest the presence of ultra-steep large scale emission. As we discussed before, the upper limit to the radio power indicates that in our case we can exclude an extended emission outside the mini-halo, furthermore from the spectral analysis we do not detected steep spectra as in the case found by Savini et al. (2018), i.e. $\alpha \simeq -1.7$.

---

[2]Spectral index flatter than -0.7 are not realistic for synchrotron emission.
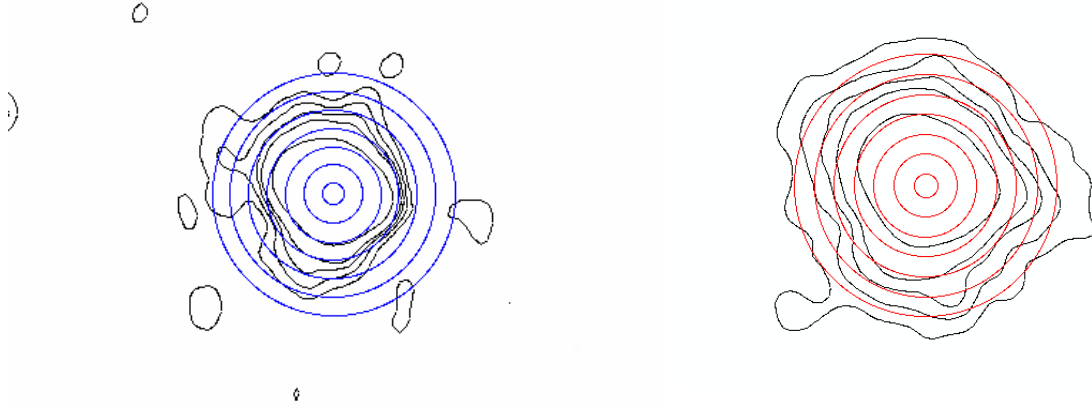
Figure 3.7: Six concentric annuli used for the spectral radial profile analysis. *Left panel*: LOFAR contours spaced by a factor of 2 starting from 3σ, where $\sigma = 258$ µJy/beam. *Right panel*: VLA contours spaced by a factor of 2 starting from $3\times$ RMS where RMS$= 27$ µJy/beam.

R_1	R_2	$\bar{R}$	$S_{140\mathrm{MHz}}$	$S_{1400\mathrm{MHz}}$	α
($''$)	($''$)	(kpc)	(mJy)	(mJy)	
1.5	4.0	13.75	72 ± 11	8.2 ± 0.4	-0.94 ± 0.07
4.0	6.5	26.25	48 ± 7	5.4 ± 0.3	-0.95 ± 0.07
6.5	9.0	38.75	23 ± 3	3.1 ± 0.2	-0.87 ± 0.07
9.0	11.5	51.25	11 ± 2	2.4 ± 0.1	-0.67 ± 0.07
11.5	14.0	63.75	5 ± 1	1.7 ± 0.1	-0.45 ± 0.09
14.0	16.5	76.25	$[1.3, 149.6]$	1.4 ± 0.1	$[-2.06, 0.06]$

Table 3.3: Details of the profile index analysis. For every annuli (Fig. 3.7) we report the inner R_1 and outer R_2 radius, the averaged radius in kpc $\bar{R}$, the flux density $S_{140\mathrm{MHz}}$, the flux density $S_{1400\mathrm{MHz}}$, the spectral index α. For the last annulus, we give the intervals of flux density and spectral index values.
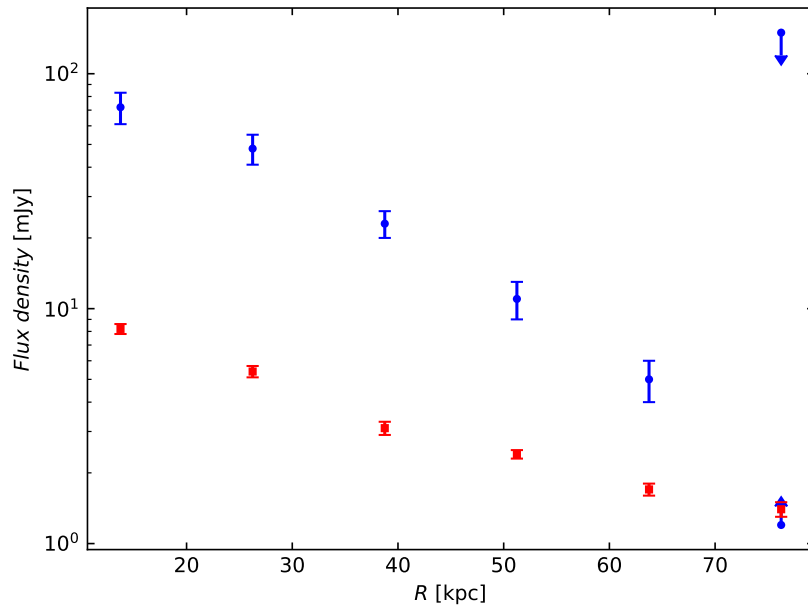
Figure 3.8: Flux density profile computed in the six annuli (Fig. 3.7) . *Red* round marks represent $S_{1400MHz}$ flux density and *blue* mark represent $S_{1400MHz}$ flux density. The vertical bars are the flux density errors. The arrows represent the lower and upper limits of the LOFAR flux density in the last annulus.
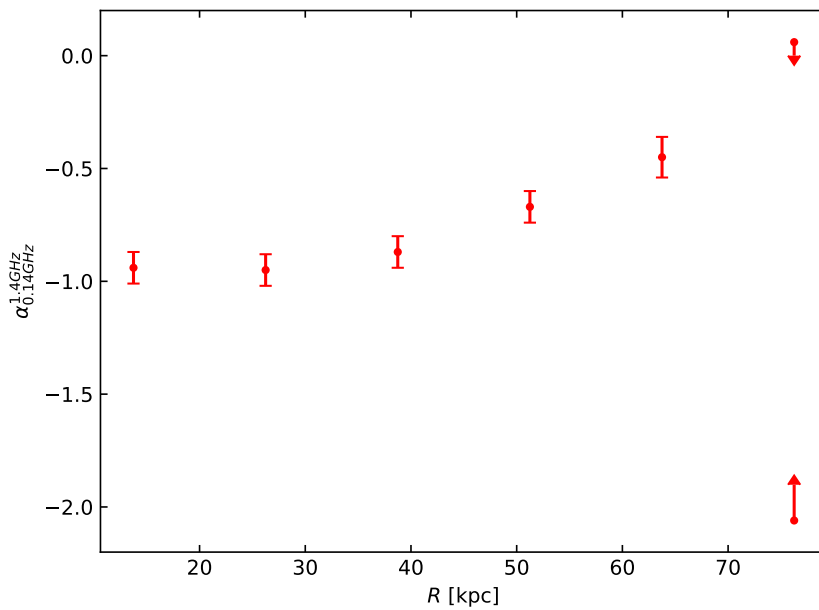
Figure 3.9: Spectral index profile between 140 and 1400 MHz. The vertical bars are the spectral index errors. The *red arrows* indicate the upper and lower limit of the spectral index in the last annulus (Fig. 3.7).

Chapter 4

Results from the Chandra analysis

In this Chapter we present the results obtained from the X-ray analysis of the archival Chandra data (ObsID2202, ObsID7902). In the first section we describe the main features of this satellite, in the second one we present the steps of the data reduction we carried out for the observations of RBS797. In the third and fourth sections, we investigate the presence of X-ray discontinuities in the ICM possibly associated to the radio emission discussed in the previous chapter, by means of detailed morphological and spectroscopic analysis.

4.1 Chandra X-ray observatory

Unlike the radio waves, the atmosphere is completely opaque to the X-ray emission. In order to study celestial sources emitting in the $3 \cdot 10^{19}$ - $3 \cdot 10^{16}$ Hz frequency range, many satellites have been launched.

The *Chandra X-ray observatory* (CXO) was launched on 23th July 1999, and it is the current X-ray satellite which reaches the highest angular resolution, about $0.5''$.

A schematic representation of the observatory is shown in Fig. 4.1. Chandra telescope is composed of the *High Resolution Mirror Assembly* (HRMA) which reflects X-rays onto one of two detectors, the *Advanced CCD Imaging Spectrometer* (ACIS) or the *High Resolution Camera* (HRC). The *High-Energy Transmission Grating* (HETG) is also present on the satellite to perform high resolution spectroscopy.

The observations of RBS797 that we discuss in this thesis were obtained with the ACIS detector. The ACIS instrument is composed by 10 CCDs, of which four chips are arranged into a square (ACIS-I) and the other six are distributed in a row (ACIS-S). The high spatial and spectral resolution (i.e. 130 eV at 1.49 keV) of ACIS CCDs provides good images and spectra of GCs.

4.2 Chandra data reduction

RBS797 was observed in *very faint* [1] (VFAINT) mode with ACIS-I on October 20th 2000 (ObsID 2202), for a total exposure of 12 ksec (Schindler et al., 2001) and on July 9th 2007 with ACIS-S (ObsID 7902), for a total exposure of 38.3 ksec (Doria et al., 2012; Cavagnolo et al., 2011). The details of the observations are listed in Tab. 4.1.

We analyzed both observations with `CIAO v.11` e `CALDB v.4.8.5`. Information of energy,

---

[1]https://cxc.cfa.harvard.edu/ciao/why/aciscleanvf.html
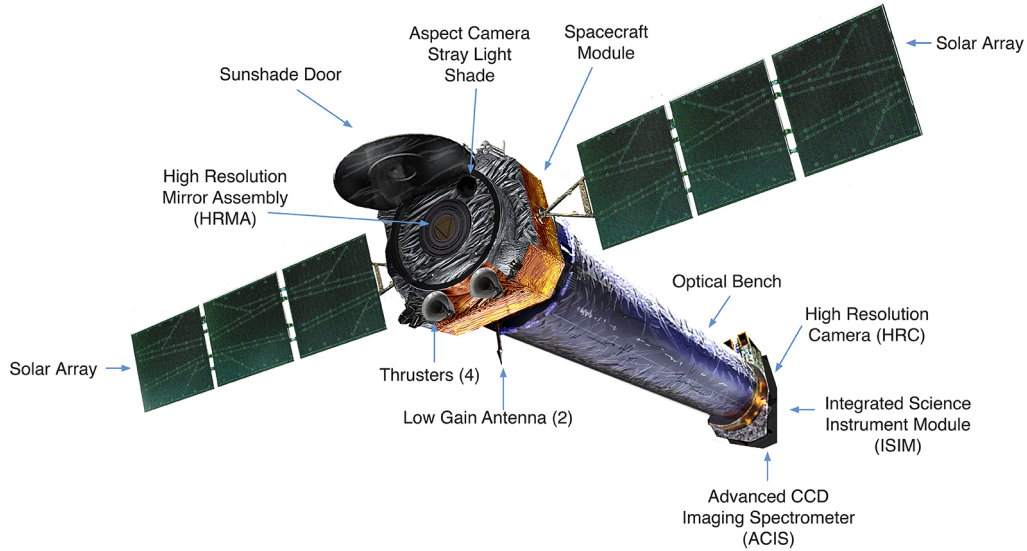
Figure 4.1: Schematic representation of the Chandra observatory. RBS797 observations were carried out with the ACIS detectors, which are placed in the focal plane of the instrument. From https://www.nasa.gov/.

Detector	date	ObsID	Exp(s)	$\text{Exp}_{\text{flare}}$
ACIS-I	October 20th 2000	2202	11749	9702
ACIS-S	July 9th 2007	7902	38306	37283

Table 4.1: Details of the ACIS-I and ACIS-S observations of RBS797. The last column, $\text{Exp}_{\text{flare}}$ indicates the exposure time after the flare removal.
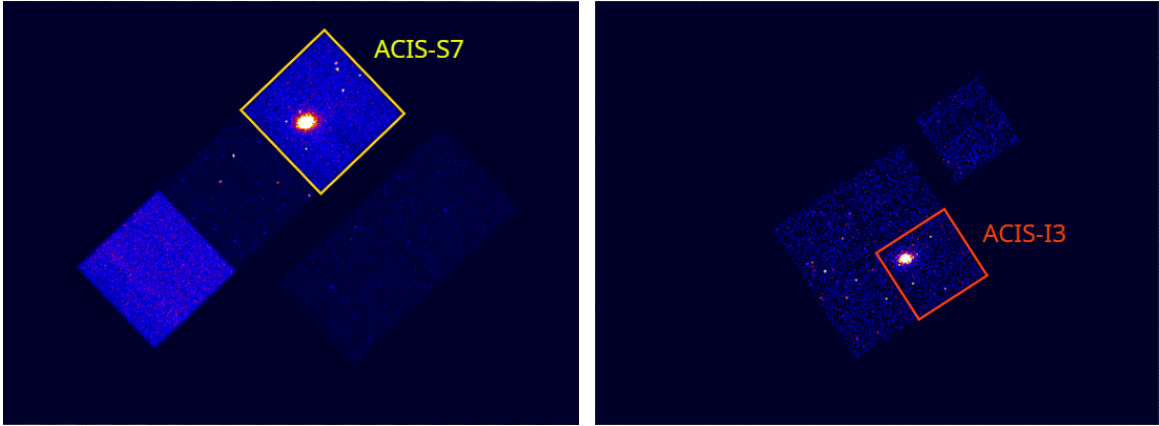
Figure 4.2: *Left panel*: Raw image which includes all ACIS-S chips of the 38.3 ksec observation (ObsID7902). The cluster RBS797 is located in the chip S7. *Right panel*: Raw image which includes all ACIS-I chips of the 12 ksec observation (ObsID2202). The chip I3 hosts RBS797.

position and time of the X-ray photons are contained in the *event file*. In order to re-calibrate the data, we run the `chandra_repro` script, which removes bad pixel and creates a new level=2 event file.

We improved the Chandra absolute astrometry by cross matching the long Chandra observation(ObsID 7902) with the short observation(ObsID 2202), indeed ObsID 7902 has a better detection of the point sources.

For both observations, point sources have been identified using the task `wavedetect`. In the observation with ACIS-I, the cluster is located in the chip I3, meanwhile in the observation with ACIS-S is found in the chip S7, as we show in Fig 4.2. As we are interested to analyze the core region, we proceeded with the data reduction of the central chip only.

In order to analyze the emission of the GC, a subtraction of the X-ray background contribution is required. The quiescent ACIS background consists of high energy particles and the *Cosmic X-ray Background* (CXB). Moreover, the Chandra orbit is disturbed by non-quiescent background periods, called *flares*, which need to be removed. We describe in the following steps the procedures to produce an the ACIS background tailored to the specific observation.

- *Removing ACIS Background Flares*: To identify these cycle events we extracted the light curves from the ACIS-I3 in the 3-12 keV band and ACIS-S7 in the 0.5-7 keV band. The procedure creates a *good time interval* (gti) file and then generates a cleaned event file. After subtracting the flare background times, we derived a total exposure for ObsID 7902 of 37 ksec and for ObsID 2202 of 9.7 ksec. We report the exact values in Tab. 4.1, in particular the total exposure for ObsID 7902 is decreased less than 3 %, and for ObsID 2202 less then 17 %.

- *normalization of the blank-sky background*: When the source is large and it is difficult to estimate a background from the dataset, it is possible to use the *blank-sky* background template, provided by the ACIS calibration team. The blank-sky datasets were obtained by combining selected observations and removing point sources from individual observations. Thus, in order to obtain the ACIS blank-sky background tailored to the observation, we re-projected the background

	Counts$_{obs}$	Exp(s)	Counts$_{bs}$	Exp$_{bk}$(s)	Q
ObsID 7902	36811	37283	434038	450000	1.02
ObsID 2202	609	9702	45886	450000	0.61

Table 4.2: Exposure times, counts of both observations and the corresponding blank-sky Exp_{bk}. They are measured in the energy range 9-12 keV after subtracting the sources. From these values, we derived the normalization factor Q, which is reported in the last column.

template to the coordinates of the observation. To perform the normalization of the blank-sky background, we subtracted the same sources in both dataset and measured the count rates in the energy band of 9-12 keV. Indeed, the photons of the observations in this energy range should be only originated from the quiescent background. Therefore, calling C_{obs} and C_{bs} the net counts of the observation and blank-sky, respectively, we calculated the normalization factor Q by the following equation:

$$Q = \frac{C_{obs} \cdot t_{bs}}{C_{bs} \cdot t_{obs}}$$

which represents the ratio of the count rates of the observation and blank-sky. The exposure time of the observation is indicated as t_{obs} and the exposure time of the blank-sky as t_{bs}. In order to match the count rate of the observation to the count rate of the blank sky (i.e. $Q = 1$), we scaled the exposure time of the blank-sky, in the full energy range, by dividing the t_{bs} by Q. The values of net counts and exposure times used to find the normalization factor Q are tabulated in Tab. 4.2. Then, the observation and background images are produced from the event files. Since we have already normalized for the count rate, to correct the background image we multiplied the net count of the observation to the ratio of the exposure times.

4.3   Radial surface brightness profiles

Thanks to the high angular resolution, Chandra is the best instrument capable to resolve surface brightness discontinuities in the ICM. The X-ray observations of RBS797 have already been analyzed by Cavagnolo et al. (2011) and Doria et al. (2012) revealing a pronounced system of cavities.

In this thesis, the X-ray analysis focused on researching brightness discontinuities in the ICM, such as shocks and cold fronts, and relate them with the morphology of radio diffuse emission.

Therefore, the first step in our analysis was to perform a detailed morphological analysis by producing surface brightness profiles of the ICM.

Firstly, we merged ObsID 7902 and ObsID 2202 with the task `merge_obs` and we use the task `reproject_image` to match background images to the corresponding merged image. To study the surface brightness profiles in the unit of flux, i.e. photons/cm^2/arcsec^2/s, it is necessary to correct for the exposure map. This is done by providing as input
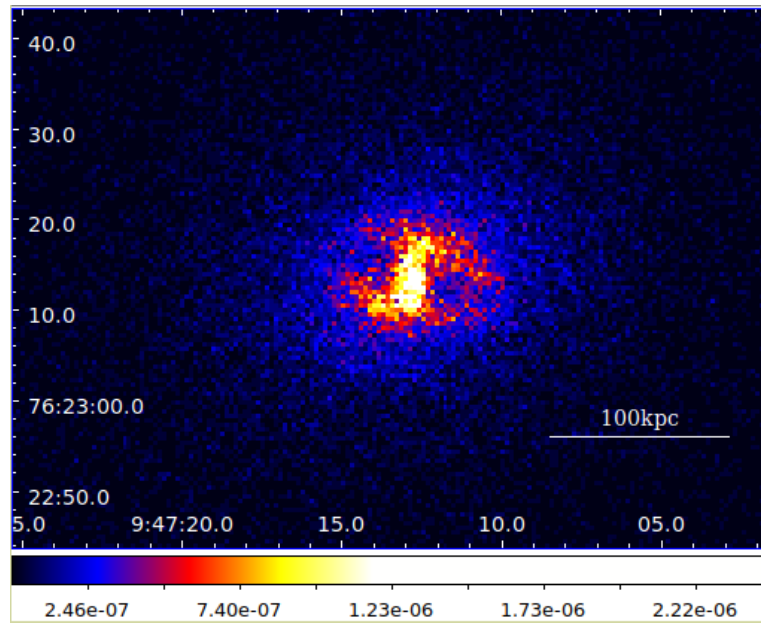
Figure 4.3: Exposure-corrected and background-subtracted image of the merge observation in the energy band 0.5-2 keV. The color bar represents the flux density in unit of phot/cm^2/s.

to `dmextract` the image in units of counts with the point sources removed, and the corrected *exposure map*, which performs the counts-to-flux conversion. The exposure-corrected and background-subtracted image in the range 0.5-2 keV is shown in Fig. 4.3.

We extracted the brightness profiles in different sectors with amplitude of 30°, 60° and 45°, as is shown in Fig. 4.4, and each sector is composed of 30 annuli spaced by 1″. The center of curvature of the annuli is chosen at the center of the cluster. We adopted a broken power-law density model to fit the surface brightness profile obtained from each annulus. This hydrodynamic model for a shock, explained in the details by Nulsen et al. (2005), assumes the point of the explosion at the center of an initially isothermal, hydrostatic atmosphere with a power-law density profile. From the best fits of broken power-law, we have information on the shock position, the expected Mach Number and the density jumps in a confidence range of 90%. An example of our this systematic analysis is shown in Fig. 4.5 where we report all the fronts we found around the entire cluster from brightness profile analysis considering sectors of 30°.

According to this morphological study, we detected surface brightness discontinuities at different distances, corresponding to density jumps varying from $\simeq 1.12$ to $\simeq 1.92$. In particular, we identified discontinuities associated to two possible fronts, one at $\simeq 8.7″$, referred to as "inner ", and one at $\simeq 16.7″$, referred to as "outer ". The positions of the inner discontinuity trace almost a circle around the cluster, instead the outer discontinuity is found in the northwest and southeast direction. As an example, we show in Fig. 4.6 some typical fitted broken power-law to the surface brightness profile obtained. The best fits of the inner and the outer jump are reported in the left and right column, respectively.
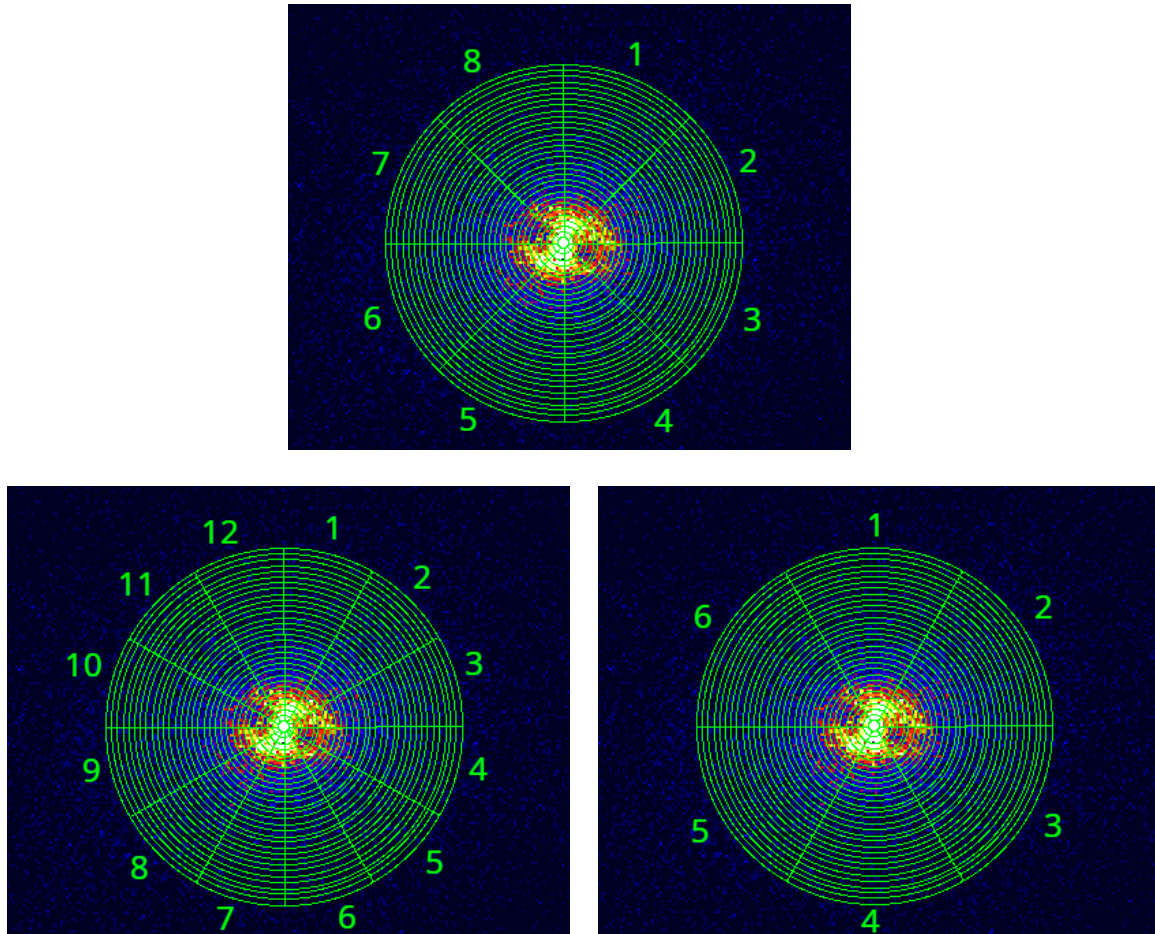
Figure 4.4: 60° sectors (*top*), 30° sectors (*bottom left*) and 45° sectors (*bottom right*) used for the brightness profile analysis. The numbers identified each sector.
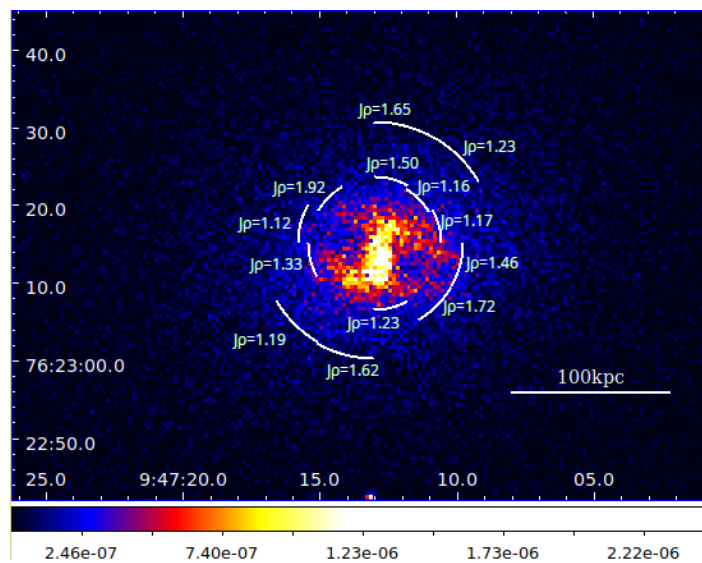
Figure 4.5: Fronts and density jumps of the discontinuities found from brightness profile analysis considering sectors of 30° around the cluster. The color bar represents the flux density in unit of phot/cm^2/s.
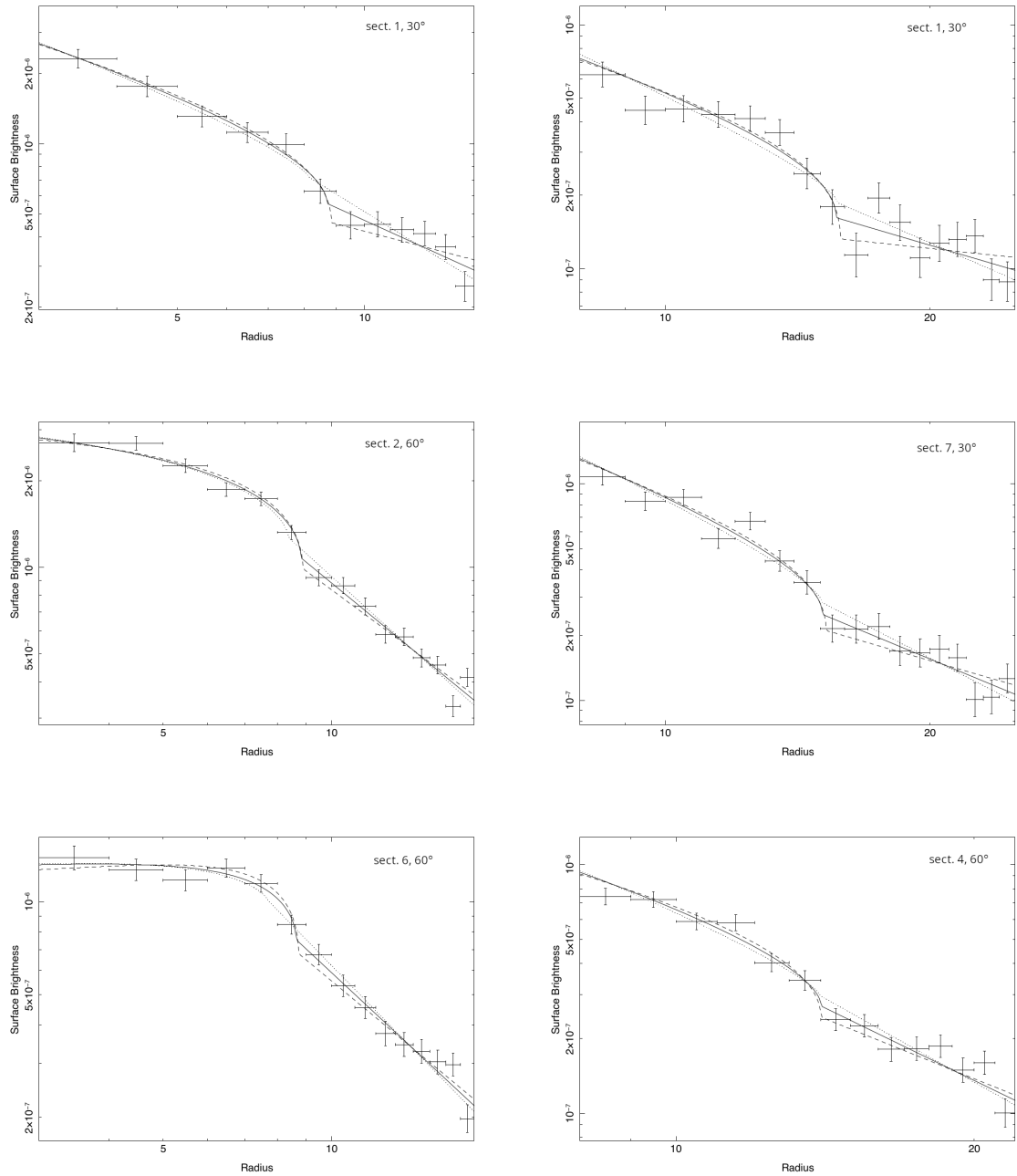
Figure 4.6: Broken power-law models to the surface brightness profiles. The numbers indicate the number of the sector from which we extract the profile (Fig. 4.5). The radial axis indicates the distance from the center of curvature of the sectors which corresponds to the center of the cluster. The radius is in unit of arcsec and the brightness profile unit is of photons/cm^2/arcsec^2/s. *Left*: Inner brightness discontinuities obtained considering 30° and 60° sectors. *Right*: Outer brightness discontinuities obtained considering 30° and 60° sectors.

4.4   X-rays Spectra

Thermodynamical properties of the ICM, such as temperature, density, abundance, pressure, can be derived from X-ray spectra. In particular, these quantities are very important to properly describe the nature of the brightness discontinuities. As we introduced in Sec. 1.3, both shock and cold front show a temperature jump across the front. The region after the shock is characterized by an increase of temperature, density, and pressure. For a cold front, the denser region has a lower temperature and the pressure across the edge is nearly continuous. We denote as *outer* and *inner* the regions before and after the discontinuities, respectively. Therefore, after the edge detection in the brightness profile analysis, we carried out a spectral study from dedicated regions to obtain a more physical interpretation of the nature of these jumps. We extracted the spectra separately from ACIS-S7 ad ACIS-I3 observations with the script `spacextract` in `CIAO`, which provides the source spectra, the background spectra, and the response matrices. Then, spectra of the two ObsIDs in the same region are jointly fitted in the energy range $0.5 - 7.0$ keV with the `XSPECv12.10.1f`. Firstly, we have considered sector regions and proceeded with the analysis of the two fronts, separately. Then, in order to derive the azimuthally-averaged profile of the entire cluster, we extracted spectra from 360 degree concentric annuli.

4.4.1   Inner discontinuity

In this section, we present the spectral results identified from the the brightness analysis, in which we obtained the position of the inner discontinuity, corresponding $8.7''$ from the center. We considered four sectors, two in the outer region and two in the inner region of the front, as we show in Fig. 4.7 .
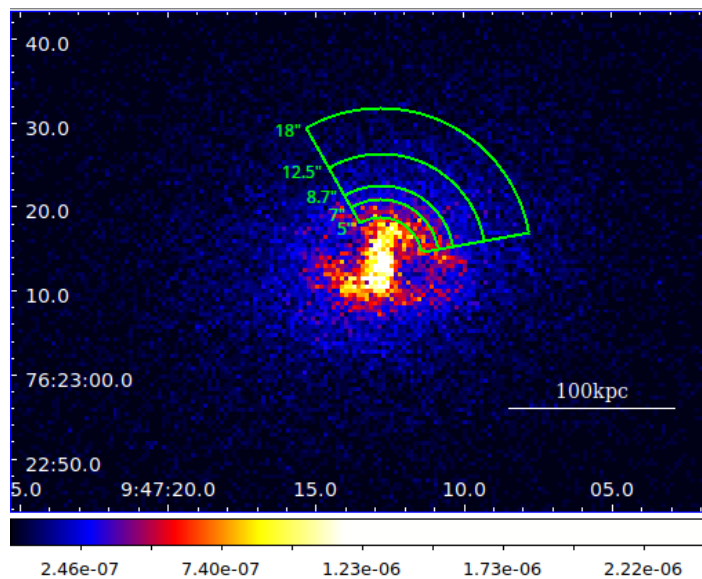
Figure 4.7: Four sectors chosen for the inner discontinuity spectral analysis.The color bar represents the flux density in unit of phot/cm^2/s.

Projected analysis

We performed a projcted analysis using the model `tbabs * apec`, where `tbabs` accounts of the absorption of X-rays in the *interstellar medium* (ISM) and `apec` accounts for the ICM thermal emission, whose parameters are temperature kT, normalization N, the metallicity Z in solar value, and redshift z. We fixed the redshift to $z = 0.35$, and the hydrogen column density n_H at the Galactic value of $2.28 \times 10^{-20} \text{cm}^{-2}$(Kalberla et al., 2005), whereas the others parameters are free to vary.

The values obtained by the projected analysis are tabulated in Tab. 4.3, where we listed the inner R_1 and outer R_2 radius of each sectors, the averaged radius in kpc, the total spectral counts, the temperature in keV, and the χ^2/dof (i.e. chi-square per degree of freedom) by fitting the model on each region. The temperature values obtained are plotted as in Fig. 4.8. The temperature of the regions before $(7'' - 8.75'')$ and after $(8.75'' - 12.5'')$ the front are $T_{\text{in}} = 4.77 \, ^{+0.52}_{-0.50}$ keV and $T_{\text{out}} = 5.88 \, ^{+0.55}_{-0.51}$ keV respectively. From this values, we obtained $T_{\text{out}}/T_{\text{in}} = 1.23 \, ^{+0.18}_{-0.17}$, and the significance of this jump corresponds to $\simeq 1\sigma$. However, we can not derive information on density and pressure of the plasma across the edge. Indeed, the spectral properties at any point on the plane of the sky are the emission-weighted superposition of radiation from all points along the line of sight through the cluster and hence, a deprojected analysis is required (see Russell et al., 2008, for more details).
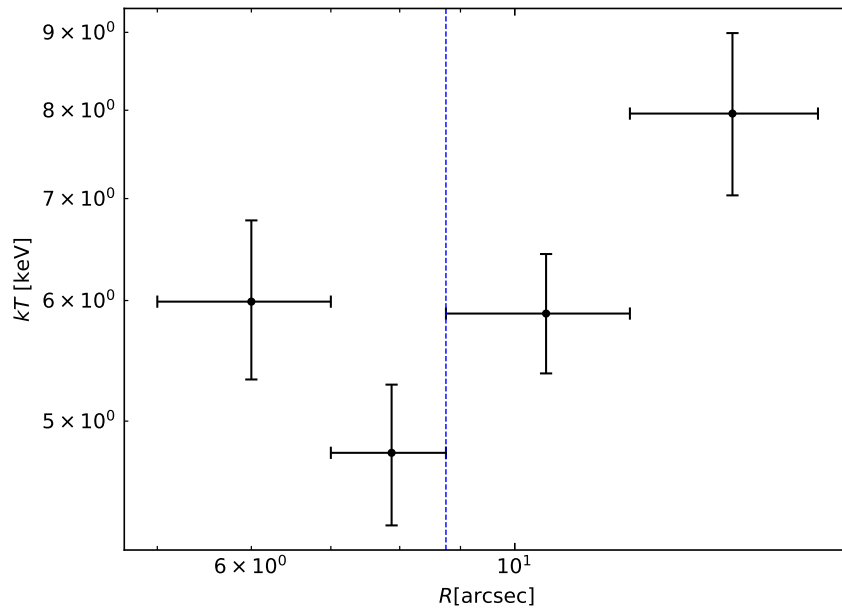
Figure 4.8: Temperature profile of the four sectors (Fig. 4.7) selected for the analysis. In *dashed blu* we indicate the position of the front, i.e. 8.7 ″ from the center. Vertical bars indicate errors which are estimated at 1σ. Horizontal bars indicate the radius of the annulus of each bin.

R_1	R_2	$\bar{R}$	Source	kT	Z	χ^2/dof
($''$)	($''$)	(kpc)	(counts)	(keV)	($Z_\odot$)	
5	7	30	1404	$5.99\,^{+0.78}_{-0.67}$	$0.22\,^{+0.33}_{-0.23}$	42.07/45
7	8.7	39	1040	$4.77\,^{+0.52}_{-0.50}$	$0.28\,^{+0.38}_{-0.28}$	41.89/33
8.7	12.5	53	1660	$5.88\,^{+0.55}_{-0.51}$	$0.67\,^{+0.42}_{-0.35}$	43.31/59
12.5	18	76	1905	$7.96\,^{+1.03}_{-0.93}$	$0.39\,^{+0.36}_{-0.36}$	68.74/63

Table 4.3: Inner radius R_1, outer radius R_2, the averaged radius in kpc, the total spectral counts, the temperature in keV, and the χ^2/dof of each sectors chosen for the projected analysis (Fig. 4.7).

Deprojected analysis

The deprojected analysis can be performed by adopting the `projct` model, which considers regions of spherical shells, and projects the flux computed from the other components onto circular annuli. We extracted spectra from the same four sectors used for the projected temperature profile, and fitted them with the `projct * tbabs * apec` model, which is a complex model with many parameters and can produce higher errors in the spectral values. Therefore, we decided to freeze $Z = 0.6$, according to the metallicity value measured in the same region of the cluster from the global profile. The values obtained are listened in Tab. 4.4, where we also reported the electronic density n_e and the pressure P. Indeed, in this case we derived n_e from normalization parameter $N(r)$ of the `apec` model, which is defined as:

$$N(r) = \frac{10^{-14}}{4\pi[D_A(1+z)]^2} \int n_e n_p dV \qquad (4.1)$$

with n_p the proton density, V the spherical shell volume and, D_A the angular diameter distance to the source, which can be written as $D_L/(1+z)^2$ with a luminosity distance D_L of 1940 Mpc for RBS797. Therefore, we can estimate n_e as:

$$n_e = \sqrt{10^{14} \cdot \frac{4\pi \cdot N(r) \cdot (\frac{D_L}{1+z})^2}{0.82 \cdot V}} \qquad (4.2)$$

where we assumed a collisionally ionized plasma. Consequently, the pressure can be calculated as follows:

$$P = 1.82 \cdot n_e \cdot kT \qquad (4.3)$$

in which we considered $n_p = 1.2\, n_e$.

In Fig. 4.9 we report the temperature, density and pressure profiles obtained. Also in this case there is a temperature jump, in particular $T_{\rm in} = 3.96\,^{+0.89}_{-0.59}$ keV and $T_{\rm out} = 4.88\,^{+0.88}_{-0.70}$ keV, which lead to $T_{\rm out}/T_{\rm in} = 1.23\,^{+0.36}_{-0.26}$ with a significance of $\simeq 1\sigma$. In this case we can analyze the density and pressure jumps, in particular these spectra suggest that the denser region has a lower temperature, as we expected from a cold front. Nevertheless, we can not confirm the presence of a cold front in the inner region of the cluster, i.e. $8.7'' - 12.5''$, because it can be related to the cool-core. As we discussed before, Doria

et al. (2012) studied in details the cavity system of this cluster and they analyzed the rims surrounding the two X-ray deficiencies. These brightness discontinuities are produced by the expansion of the radio lobes which displace and compress the ICM. These authors found the inner bright rims surrounding the prominent cavities extending to $\simeq 8'' - 10''$ from the center of the cluster, and hence they cover the region chosen in our analysis. Therefore, even if from the deprojcted analysis we found a denser region with a lower temperature, the compression we detected across the front can be associated to the presence of the inner rims generated by the cavities.

R_1	R_2	$\bar{R}$	kT	N	n_e	P
$('')$	$('')$	(kpc)	(keV)	$(\times 10^{-4})$	$(\times 10^{-3} \text{cm}^{-3})$	$(\times 10^{-9} \text{erg cm}^{-3})$
5	7	30	$7.47\,^{+3.35}_{-2.14}$	$7.33\,^{+0.50}_{-0.50}$	$81.37\,^{+2.79}_{-2.79}$	$1.11\,^{+0.50}_{-0.32}$
7	8.75	39	$3.96\,^{+0.89}_{-0.59}$	$7.70\,^{+0.50}_{-0.50}$	$67.84\,^{+2.21}_{-2.21}$	$0.49\,^{+0.11}_{-0.08}$
8.75	12.5	53	$4.88\,^{+0.88}_{-0.70}$	$8.77\,^{+0.50}_{-0.50}$	$36.57\,^{+1.04}_{-1.04}$	$0.33\,^{+0.06}_{-0.05}$
12.5	18	76	$7.61\,^{+0.77}_{-0.76}$	$20.16\,^{+0.46}_{-0.46}$	$31.87\,^{+0.36}_{-0.36}$	$0.44\,^{+0.45}_{-0.45}$

Table 4.4: Inner radius R_1, outer radius R_2, the averaged radius $\bar{R}$ in kpc, the temperature in keV, the normalization N, the electronic density n_e, and the pressure P obtained from each sectors chosen for the deprojected analysis (Fig. 4.7).
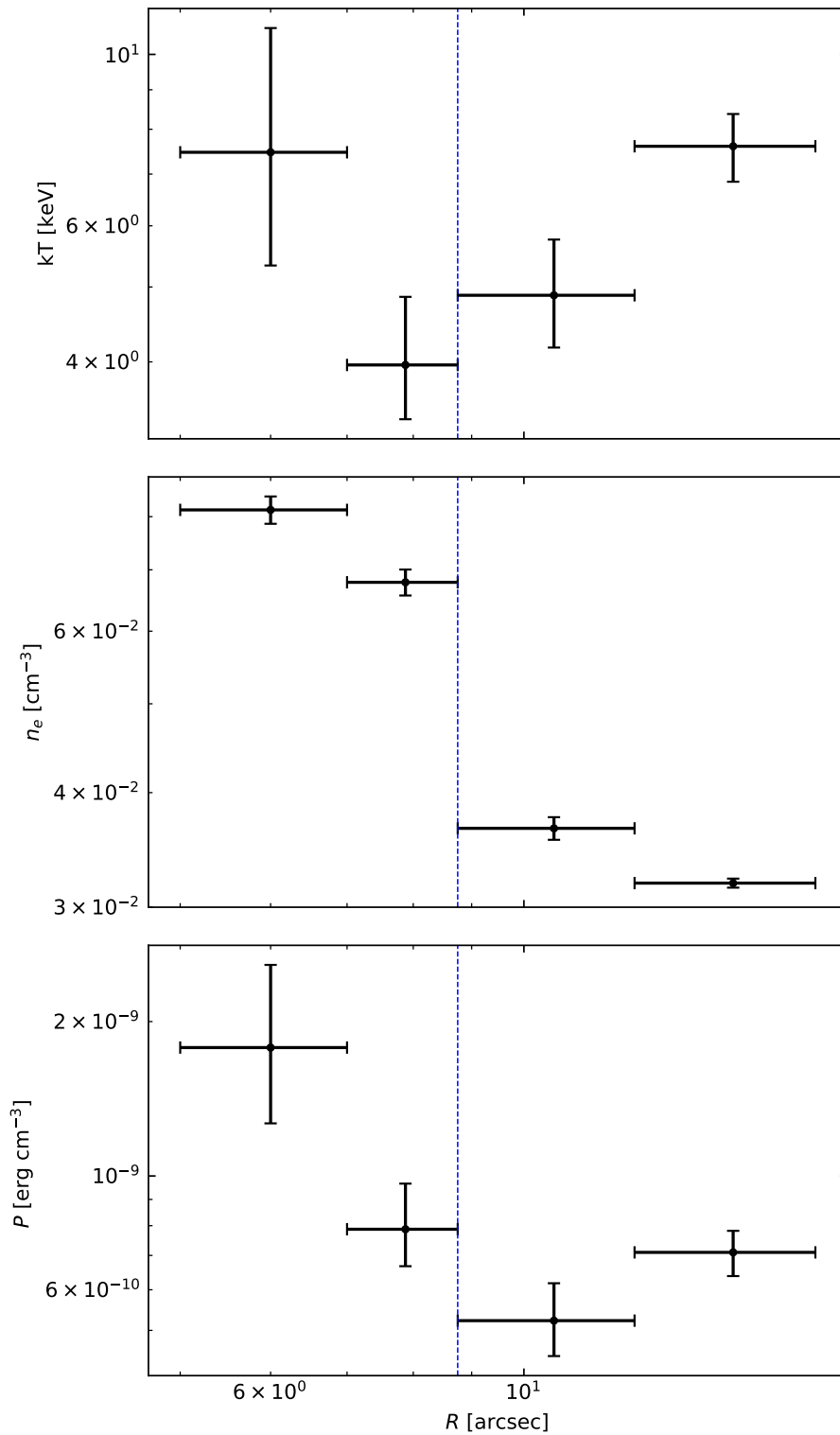
Figure 4.9: Temperature (*top*), density (*middle*), and pressure (*bottom*) profiles from the deprojected analysis from the sectors in Fig. 4.7. The jump is found at 8.7 ″ from the center. The *blue dashed* line represents the position of the front. Vertical bars indicate errors which are estimated at 1σ. Horizontal bars indicate the radius of the annulus of each bin.

4.4.2 Outer discontinuity

After studying the inner discontinuity, we performed the same projected and deprojected analysis for the outer edge. From the surface brightness detection, the jump is located at $16.7''$ from the center. The spectra were extracted by the four sectors shown in Fig. 4.10.

Projected analysis

Adopting the `tbabs * apec` and freezing the value of $z = 0.35$ and $n_H = 2.28 \times 10^{-20} \mathrm{cm}^{-2}$, we obtained the values reported in Tab. 4.5 and the temperature profile in Fig. 4.11. In this case, the inner region $(13 - 16.7'')$ has higher temperature than the outer region $(16.7 - 24'')$, in particular they are $T_{\mathrm{in}} = 8.27 ^{+1.70}_{-1.29}$ and $T_{\mathrm{out}} = 6.76 ^{+0.93}_{-0.59}$, thus we obtained $T_{\mathrm{in}}/T_{\mathrm{out}} = 1.22 ^{+0.30}_{-0.22}$. The temperature jump as a significance of $\simeq 1\sigma$. In order to understand the nature of this edge we performed the deprojected analysis.

Deprojected analysis

As in the case of the inner discontinuities, we used the `projct * tbabs * apec` model, and also in this case we decided to freeze $Z = 0.5$ according to the value obtained from the global profile. From the Eq. 4.2 and Eq. 4.3, we computed the density and pressure values for each sectors. These quantities are listed in Tab. 4.6 and they are plotted in Fig. 4.12. Also from the deprojected analysis, we found a temperature jump across the front with a significance of $\simeq 1\sigma$, with $T_{\mathrm{in}} = 8.66 ^{+3.06}_{-1.47}$ and $T_{\mathrm{out}} = 5.98 ^{+1.24}_{-0.87}$, corresponding to $T_{\mathrm{in}}/T_{\mathrm{out}} = 1.45 ^{+0.59}_{-0.32}$. In particular, we noted a interesting pressure jump, with a significance of $\simeq 2\sigma$, with $P_{\mathrm{in}}/P_{\mathrm{out}} = 2.81 ^{+1.13}_{-0.61}$, where $P_{\mathrm{in}} = 0.45 ^{+0.16}_{-0.08}$ and $P_{\mathrm{out}} = 0.16 ^{+0.03}_{-0.02}$. Therefore, this spectral analysis suggests the presence of a shock wave which are propagating toward the external region, compressing the ICM and leading to a pressure jump. To investigate whether these properties are also present in the global ICM, we performed an azimuthally-averged analysis, as we explain in the next section.
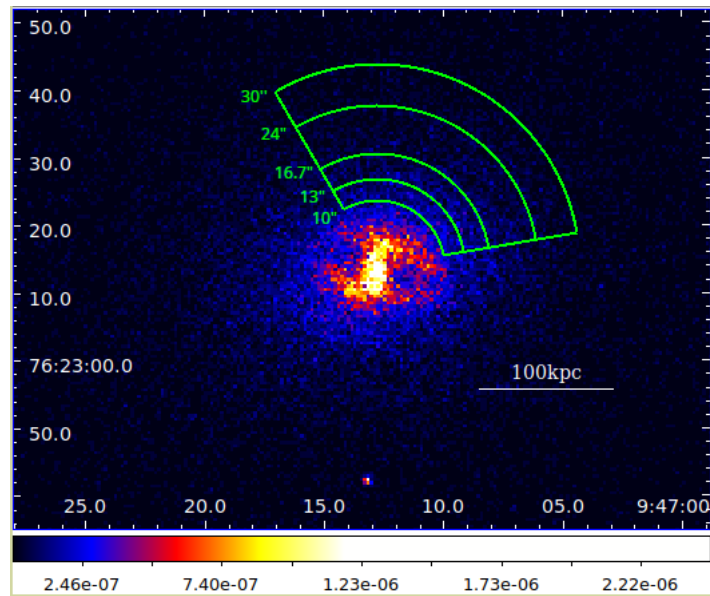
Figure 4.10: Four sectors chosen for the outer discontinuity spectral analysis. The color bar represents the flux density in unit of phot/cm^2/s.
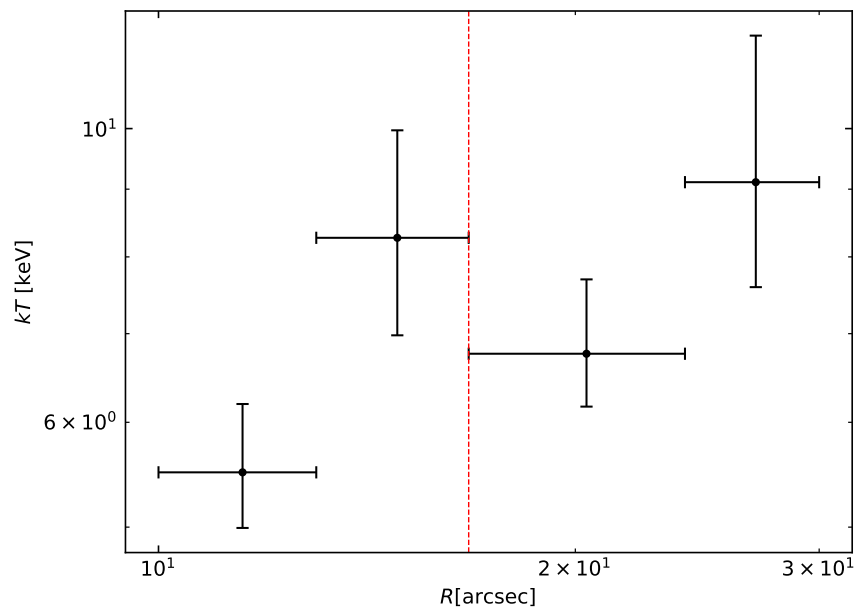
Figure 4.11: Temperature profile of the four sectors (Fig. 4.10) selected for the analysis. In *dashed red* we indicate the position of the front, i.e. 16.7 $''$ from the center. Vertical bars indicate error which are estimated at 1σ. Horizontal bars indicate the radius of the annulus of each bin.

R_1	R_2	$\bar{R}$	Source	kT	Z	χ^2/dof
($''$)	($''$)	(kpc)	(counts)	(keV)	($Z_\odot$)	
10	13	58	1234	$5.50\,^{+0.69}_{-0.51}$	$0.59\,^{+0.41}_{-0.34}$	$41.31/43$
13	16.7	74	1470	$8.27\,^{+1.70}_{-1.29}$	$0.18\,^{+0.57}_{-0.18}$	$63.98/49$
16.7	24	102	1959	$6.76\,^{+0.93}_{-0.59}$	$0.47\,^{+0.37}_{-0.35}$	$91.37/68$
24	30	135	969	$9.11\,^{+2.65}_{-1.52}$	$0.17\,^{+0.56}_{-0.17}$	$29.59/36$

Table 4.5: Inner radius R_1, outer radius R_2, the averaged radius in kpc, the total spectral counts, the temperature in keV, and the χ^2/dof of each sectors chosen for the projected analysis (Fig. 4.10).

R_1	R_2	R_{mid}	kT	N	n_e	P
($''$)	($''$)	(kpc)	(keV)	($\times 10^{-4}$)	($\times 10^{-3}\text{cm}^{-3}$)	($\times 10^{-9}\text{erg cm}^{-3}$)
10	13	58	$3.71\,^{+0.83}_{-0.59}$	$6.83\,^{+0.55}_{-0.55}$	$33.35\,^{+1.35}_{-1.34}$	$0.23\,^{+0.05}_{-0.04}$
13	16.7	74	$8.66\,^{+3.06}_{-1.47}$	$10.23\,^{+0.52}_{-0.51}$	$28.25\,^{+0.71}_{-0.71}$	$0.45\,^{+0.16}_{-0.08}$
16.7	24	102	$5.98\,^{+1.24}_{-0.87}$	$10.46\,^{+0.52}_{-0.52}$	$14.96\,^{+0.38}_{-0.37}$	$0.16\,^{+0.03}_{-0.02}$
24	30	135	$8.52\,^{+1.46}_{-1.20}$	$13.25\,^{+0.43}_{-0.43}$	$14.02\,^{+0.23}_{-0.23}$	$0.22\,^{+0.04}_{-0.03}$

Table 4.6: Inner radius R_1, outer radius R_2, the averaged radius $\bar{R}$ in kpc, the temperature in keV, the normalization N, the electronic density n_e, and the pressure P obtained from each sectors chosen for the deprojected analysis (Fig. 4.7).
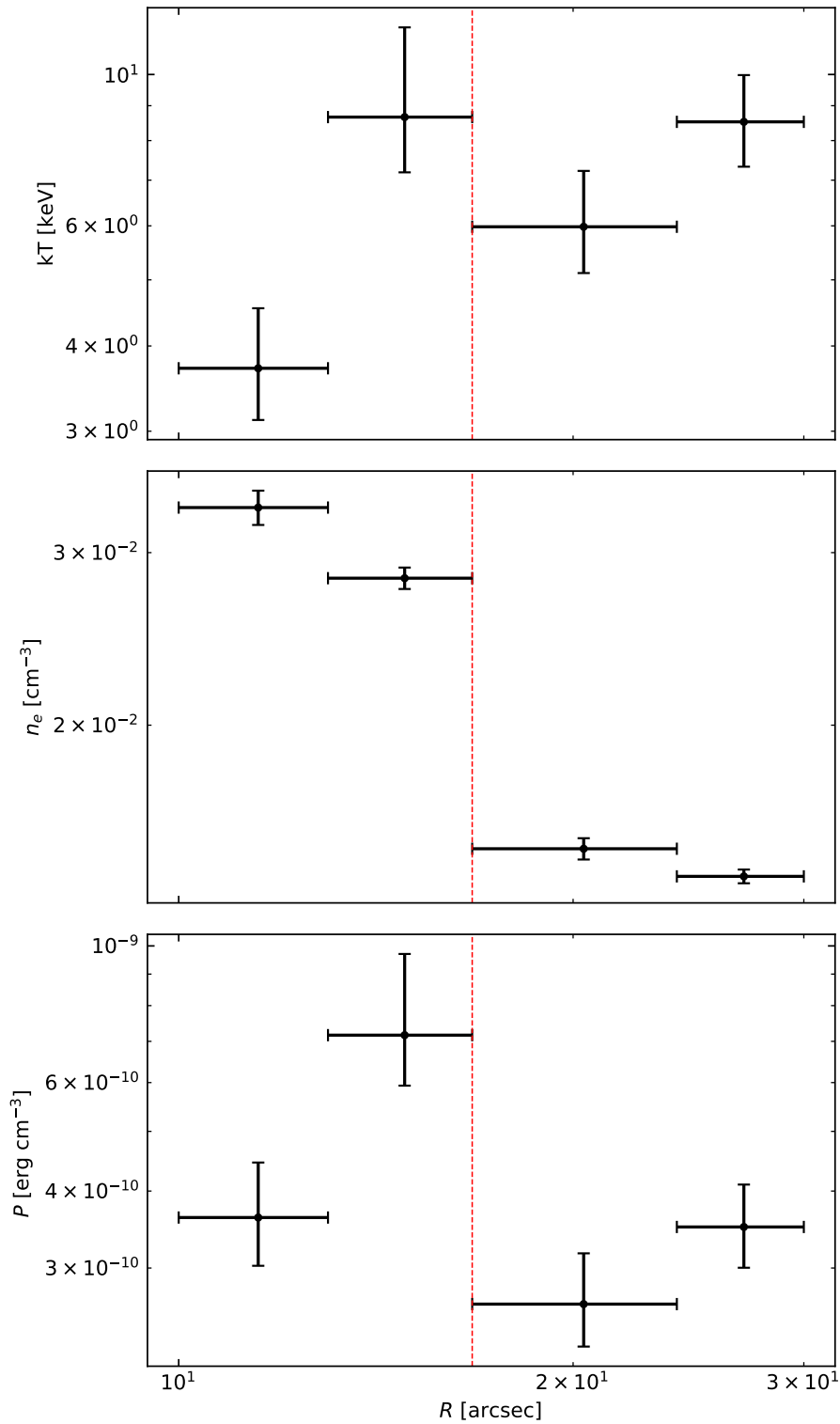
Figure 4.12: Temperature (*top*), density (*middle*), and pressure (*bottom*) profiles from the deprojected analysis from the sectors in Fig. 4.10. The jump is found at 16.7 ″ from the center. The *red dashed* line represents the front. Vertical bars indicate error which are estimated at 1σ. Horizontal bars indicate the radius of the annulus of each bin.
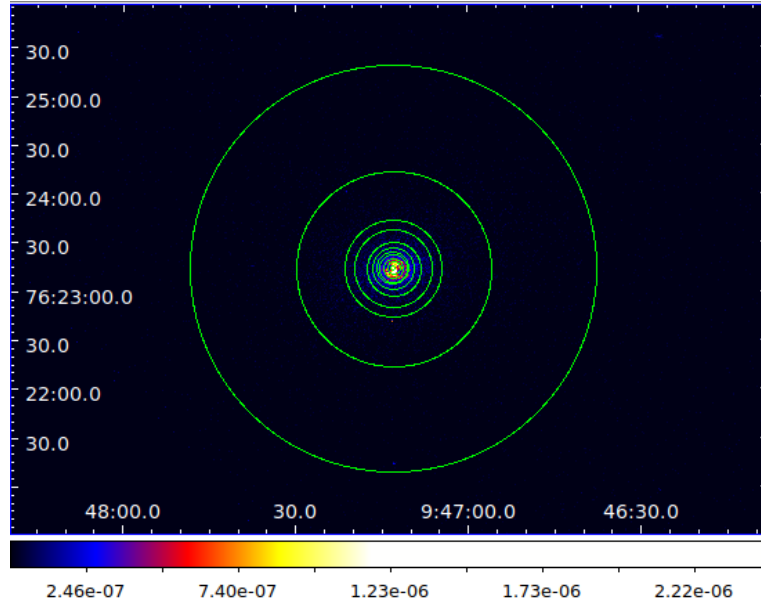
Figure 4.13: Ten circular sectors from the center of the cluster selected for the analysis.The color bar represents the flux density in unit of phot/cm^2/s.

4.5 Azimuthally-averaged study of the discontinuities

The analysis we carried out by extracting spectra from dedicated sectors has revealed interesting features of the inner and outer jumps. To increase the statistic of our spectra and perform a global study of the nature of these discontinuities, we considered ten concentric annuli from the center of the cluster, which are showed in Fig. 4.13. These regions are chosen in order to exclude the central annulus with radius of $\simeq 7.2$ kpc which contains the central X-ray AGN, and include annuli with radius corresponding to the inner and outer region of the fronts at $8.7''$ and $16.7''$.

Projected analysis

The values obtained by adopting the `tbabs * apec` model are tabulated in Tab. 4.7, and the temperature radial profile is shown in Fig.4.15. From this, we observe an internal temperature jump with $T_{\text{in}} = 5.33\,^{+0.23}_{-0.20}$, $T_{\text{out}} = 6.35\,^{+0.53}_{-0.50}$ and thus with $T_{\text{out}}/T_{\text{in}} = 1.19\,^{+0.11}_{-0.10}$, and significance of $\simeq 2\sigma$, and an the external jump with $T_{\text{in}} = 7.99\,^{+0.69}_{-0.65}$ and $T_{\text{out}} = 7.00\,^{+0.41}_{-0.35}$, which lead to $T_{\text{in}}/T_{\text{out}} = 1.14\,^{+0.12}_{-0.11}$ with a significance of $\simeq 1\sigma$. Therefore, the temperature trend found from the sectors analysis for the inner and outer discontinuities is maintained. The projected temperature profile gradually rises going outwards, except the last value which represents the typical temperature decline observed at larger radii in CC GCs. To confirm the general shape of the temperature profiles observed for relaxed cluster, we created a scaled temperature profiles showed in Fig. 4.14. This profile was computed by estimating the emission-weighted cluster temperature $\langle T_X \rangle = 8.5 \pm 0.3$ keV, obtained after excluding the central 100 kpc region affected by the radiative cooling, and the virial radius R_{vir} as follows (Evrard, 1997):

$$R_{\text{vir}} = 2.74 \text{ Mpc } \sqrt{\frac{T_X}{10 \text{ keV}}} \tag{4.4}$$
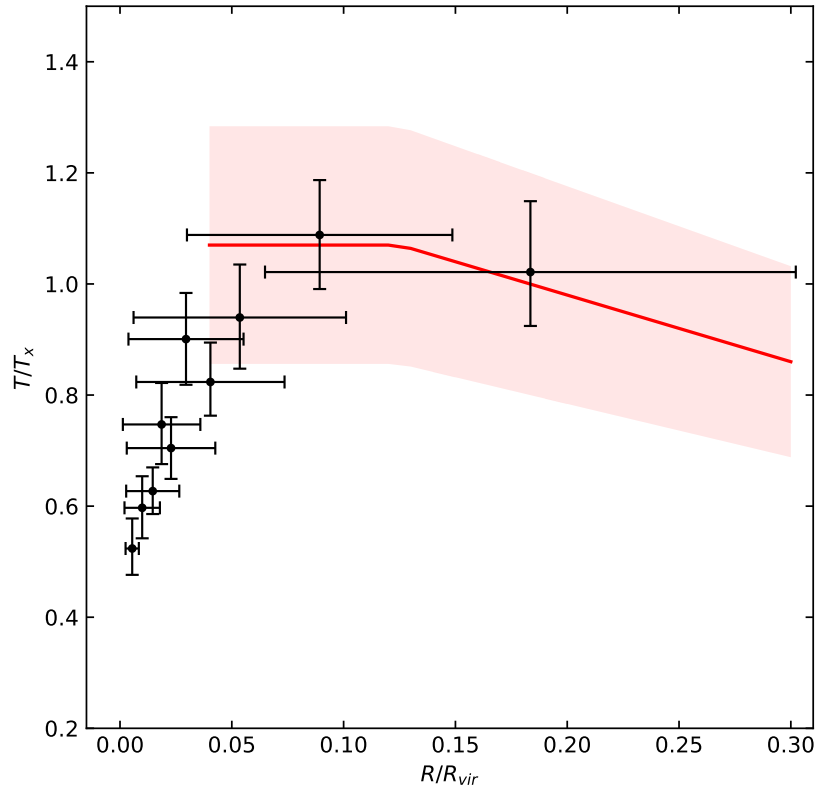
Figure 4.14: Projected temperature profile obtained by extracting spectra from the ten circular annulus from the center (Fig. 4.13). The temperature T is scaled to cluster emission-weighted temperature $\langle T_X \rangle$ and the radius R is scaled to the virial radius R_{vir}, calculated as in Eq. 4.4. The *red line* is computed using Eq. 4.5 and represents the general trend of relaxed clusters for $R \geq 0.15 R_{\mathrm{vir}}$. The *red area* indicates the 15% of scatter.

which corresponds to 2.52 Mpc. In particular, the red line in Fig. 4.14 was computed by following the functional form presented by Vikhlinin et al. (2005), which describes the almost identical trend of relaxed GCs for $R \geq 0.15 R_{\mathrm{vir}}$, and it can be written as:

$$T/\langle T_X \rangle = \begin{cases} 1.07, & 0.035 < R/R_{\mathrm{vir}} < 0.125 \\ 1.22 - 1.2 R/R_{\mathrm{vir}}, & 0.125 < R/R_{\mathrm{vir}} < 0.6 \end{cases} \qquad (4.5)$$

with a scatter of 15% (the red area). Therefore, we note that this temperature profile is in good agreement with the other profile obtained from relaxed GCs (Vikhlinin et al., 2005).

R_1	R_2	$\bar{R}$	Source	kT	Z	χ^2/dof
($''$)	($''$)	(kpc)	(counts)	(keV)	($Z_\odot$)	
1.5	4	14	4101	$4.45\,^{+0.24}_{-0.21}$	$0.47\,^{+0.10}_{-0.09}$	$111.97/122$
5	6	28	3961	$5.07\,^{+0.24}_{-0.23}$	$0.53\,^{+0.11}_{-0.10}$	$107.55/127$
6	8.7	37	5869	$5.33\,^{+0.23}_{-0.20}$	$0.43\,^{+0.08}_{-0.08}$	$181.84/162$
8.7	10	47	2252	$6.35\,^{+0.53}_{-0.50}$	$0.59\,^{+0.18}_{-0.17}$	$75.46/71$
10	13	58	4374	$5.99\,^{+0.35}_{-0.34}$	$0.51\,^{+0.11}_{-0.10}$	$130.91/132$
13	16.7	75	4339	$7.66\,^{+0.57}_{-0.56}$	$0.29\,^{+0.11}_{-0.11}$	$141.40/132$
16.7	24	102	6054	$7.00\,^{+0.41}_{-0.35}$	$0.24\,^{+0.08}_{-0.07}$	$141.18/170$
24	30	135	3411	$7.99\,^{+0.69}_{-0.65}$	$0.26\,^{+0.13}_{-0.12}$	$87.36/102$
30	60	225	8780	$9.25\,^{+0.67}_{-0.65}$	$0.26\,^{+0.09}_{-0.09}$	$238.00/219$
60	125	463	7748	$8.68\,^{+0.98}_{-0.68}$	$0.68\,^{+0.17}_{-0.17}$	$205.27/222$

Table 4.7: Values obtained from spectral fitting of the 10 concentric annuli centered on the cluster center using `tbabs * apec` model. The inner edge corresponds to 8.7$''$ and the outer to 16.7 $''$. Errors are calculated at 1σ.
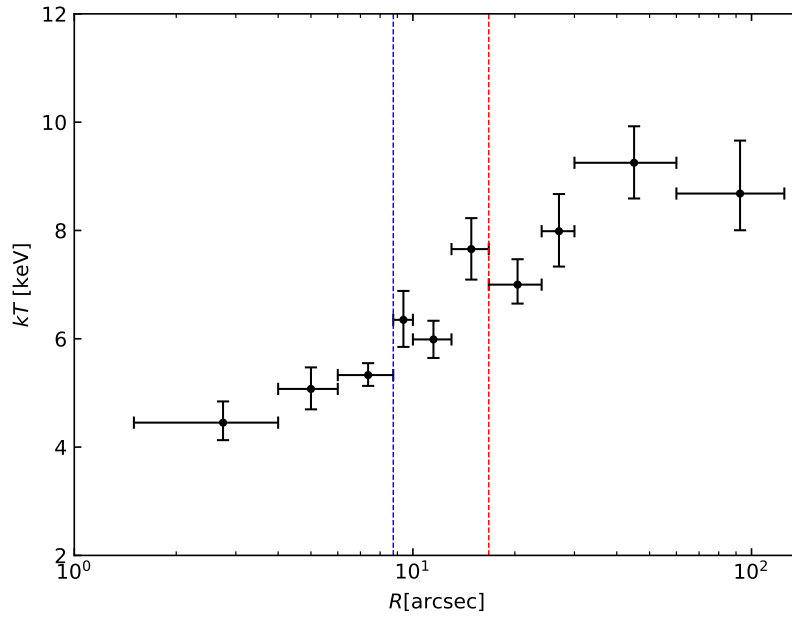
Figure 4.15: Temperature profile from the protected analysis. The dashed lines represent the inner (*blue*) and the outer (*red*) jumps. Vertical bars indicate error which are estimated at 1σ. Horizontal bars indicate the radius of the annulus of each bin.

Deprojected analysis

We used the `projct * tbabs * apec` model to obtain the values listened in Tab. 4.8 and plots reported in the Fig. 4.16. The spectra suggest two jumps in the positions of the brightness discontinuities. We obtained for the inner jump $T_{\text{in}} = 4.60^{+0.55}_{-0.46}$ and $T_{\text{out}} = 6.77^{+2.43}_{-1.39}$, with $T_{\text{out}}/T_{\text{in}} = 1.47^{+0.56}_{-0.34}$ and hence a significance of $\simeq 1\sigma$, instead for the external jump $T_{\text{in}} = 8.00^{+1.27}_{-1.13}$ and $T_{\text{out}} = 6.56^{+0.77}_{-0.66}$, thus $T_{\text{in}}/T_{\text{out}} = 1.22^{+0.24}_{-0.21}$, with a significance of $\simeq 1\sigma$. As in the sectors analysis, we found the outer edge with typical feature of a shock front, and also in this case we have an evident pressure jump with a significance of $\simeq 2\sigma$, where $P_{\text{in}} = 0.62^{+0.10}_{-0.09}$ and $P_{\text{out}} = 0.31^{+0.04}_{-0.03}$, leading to $P_{\text{in}}/P_{\text{out}} = 2.00^{+0.41}_{-0.35}$.

In the assumption of shock, the Mach number predicted from the broken power-law brightness profile fit of the outer discontinuity (see Fig. 4.6) is $\simeq 1.4^{+0.9}_{-0.3}$, with a density jump of $\simeq 1.6$. Therefore, the expected temperature jump can be estimated as (Markevitch & Vikhlinin, 2007):

$$\frac{T_{\text{in}}}{T_{\text{out}}} = \frac{[(5\mathcal{M}^2 - 1)(3 + \mathcal{M}^2)]}{16\mathcal{M}^2} \tag{4.6}$$

which corresponds to $\simeq 1.4^{+0.9}_{-0.3}$. The temperature jump observed from the deprojected analysis is $\simeq 1.1^{+0.1}_{-0.1}$, and thus is consistent within errors with that predicted. These numbers suggest the presence of a weak shock propagating in the outer regions of the cluster.

In Fig. 4.17 and in Fig.4.18 we show the surface brightness profile best fit of the inner and outer discontinuities, and the temperature profiles subsequently obtained extracting spectra from the outer and inner regions of the two fronts. As we explained before, even if the inner discontinuity presents typical properties of cold fronts, we can not exclude that the compression revealed in this edge is due to the presence of the bright rims previously studied by Doria et al. (2012).

From the spectral analysis of the outer brightness discontinuity at 16.7 ″, we favour the interpretation of this edge as a shock front since we found a heated and compressed surrounding ICM. This detection is consistent with our prediction of the presence of a shock front from the radio spectral analysis, in which we found a flattening of the spectral index moving towards the outer region of the cluster. The Mach number of the shock can be obtained also using the radio integral spectral index. Indeed, from the DSA theory (see Sec. 1.4.5),the Mach number of shock wave can be written as:

$$\mathcal{M}_{\text{radio}} = \sqrt{\frac{-\alpha_{\text{inj}} + 1}{-\alpha_{\text{inj}} - 1}}$$

where α_{inj} is the injection spectral index. In our case, it corresponds to $\alpha_{\text{inj}} = -0.77 \pm 0.25$ (which is azimuthally averaged spectral index, Sec. 3.2.1), and therefore we obtain an unphysical value for $\mathcal{M}_{radio}$. This result is not surprising, and it is found also in other clusters, in particular it suggests a deviation from this simplistic model which assumes stationariety. Moreover, the measurement of α_{inj} can be affected by many uncertainties, for example it can be reflect a mixing of different electron populations due to projection effects (van Weeren et al., 2019).
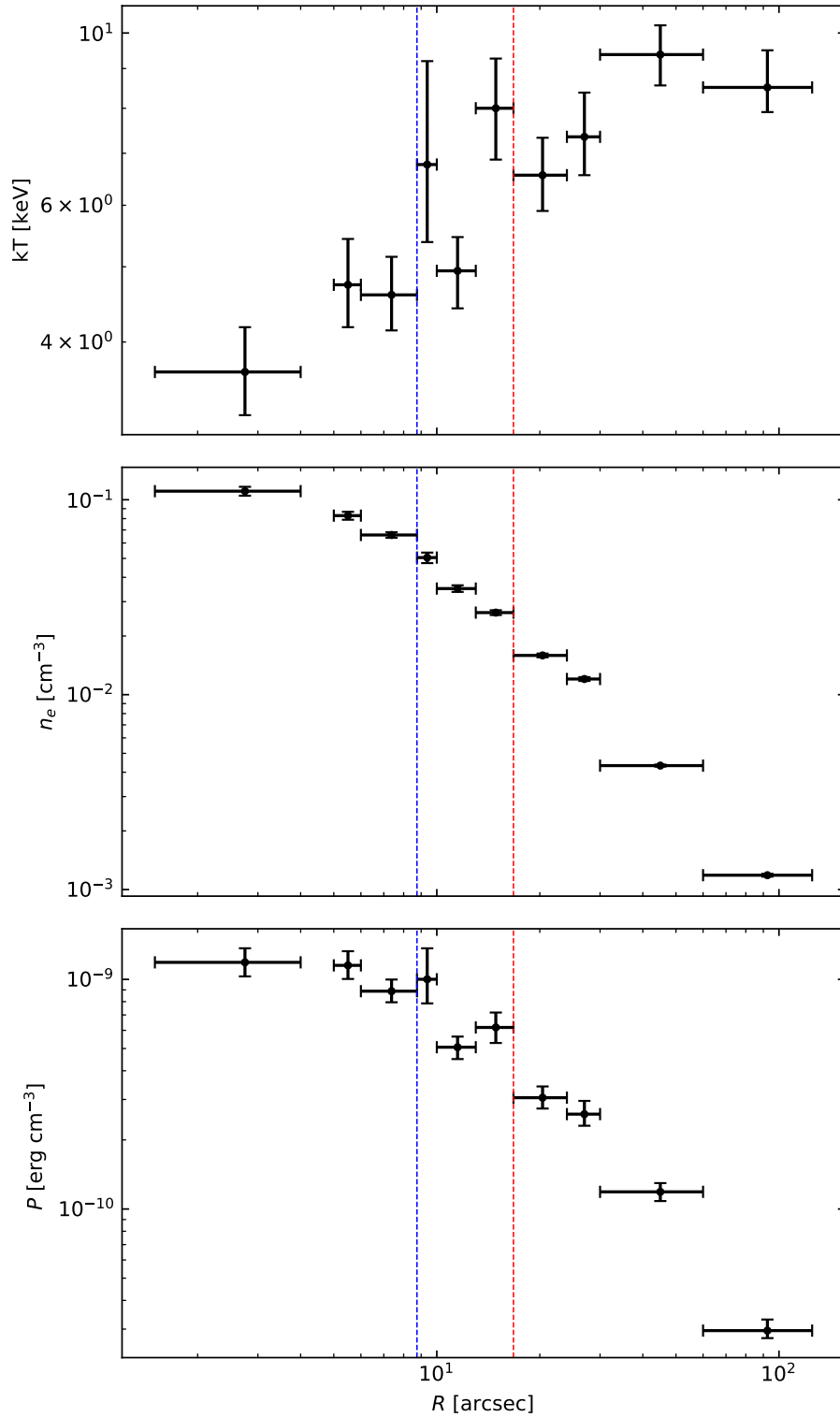
Figure 4.16: Temperature (*top*), density (*middle*), and pressure (*bottom*) profiles from the deprojected analysis. The dashed lines represent the inner (*blue*) and the outer (*red*) jumps. Vertical bars indicate error which are estimated at 1σ. Horizontal bars indicate the radius of the annulus of each bin.

R_1	R_2	$\bar{R}$	kT	Z	N	n_e	P
($''$)	($''$)	(kpc)	(keV)	($Z_\odot$)	($\times 10^{-4}$)	($\times 10^{-3}$cm^{-3})	($\times 10^{-9}$erg cm^{-3})
1.5	4	14	$3.66^{+0.52}_{-0.44}$	$0.45^{+0.29}_{-0.25}$	$3.80^{+0.40}_{-0.40}$	$110.67^{+5.85}_{-5.81}$	$1.19^{+0.18}_{-0.16}$
5	6	28	$4.74^{+0.69}_{-0.56}$	$0.68^{+0.35}_{-0.30}$	$5.35^{+0.49}_{-0.51}$	$82.92^{+3.83}_{-3.94}$	$1.15^{+0.18}_{-0.15}$
6	8.7	37	$4.60^{+0.55}_{-0.46}$	$0.33^{+0.20}_{-0.19}$	$10.10^{+0.67}_{-0.66}$	$65.95^{+2.17}_{-2.15}$	$0.89^{+0.11}_{-0.09}$
8.7	10	47	$6.77^{+2.43}_{-1.39}$	$0.65^{+0.58}_{-0.48}$	$4.31^{+0.52}_{-0.54}$	$50.50^{+3.06}_{-3.18}$	$1.00^{+0.36}_{-0.22}$
10	13	58	$4.94^{+0.52}_{-0.52}$	$0.74^{+0.28}_{-0.25}$	$7.53^{+0.59}_{-0.58}$	$35.02^{+1.38}_{-1.35}$	$0.51^{+0.06}_{-0.06}$
13	16.7	75	$8.00^{+1.27}_{-1.13}$	$0.35^{+0.24}_{-0.23}$	$8.91^{+0.50}_{-0.50}$	$26.36^{+0.74}_{-0.74}$	$0.62^{+0.10}_{-0.09}$
16.7	24	102	$6.56^{+0.77}_{-0.66}$	$0.24^{+0.16}_{-0.14}$	$11.80^{+0.53}_{-0.52}$	$15.90^{+0.35}_{-0.35}$	$0.31^{+0.04}_{-0.03}$
24	30	135	$7.35^{+1.03}_{-0.79}$	$0.27^{+0.14}_{-0.18}$	$9.76^{+0.45}_{-0.45}$	$12.03^{+0.27}_{-0.27}$	$0.26^{+0.04}_{-0.03}$
30	60	225	$9.38^{+0.85}_{-0.82}$	$0.16^{+0.11}_{-0.11}$	$18.10^{+0.45}_{-0.44}$	$4.33^{+0.05}_{-0.05}$	$0.19^{+0.01}_{-0.01}$
60	125	463	$8.51^{+0.99}_{-0.60}$	$0.69^{+0.18}_{-0.17}$	$12.50^{+0.42}_{-0.42}$	$1.19^{+0.02}_{-0.02}$	$0.03^{+0.03}_{-0.02}$

Table 4.8: Values obtained from spectral fitting of the 10 concentric annuli centered on the cluster center using `projct * (tbabs * apec)` model. The inner edge corresponds to 8.7$''$ and the outer to 16.7 $''$. Errors are calculated at 1σ.
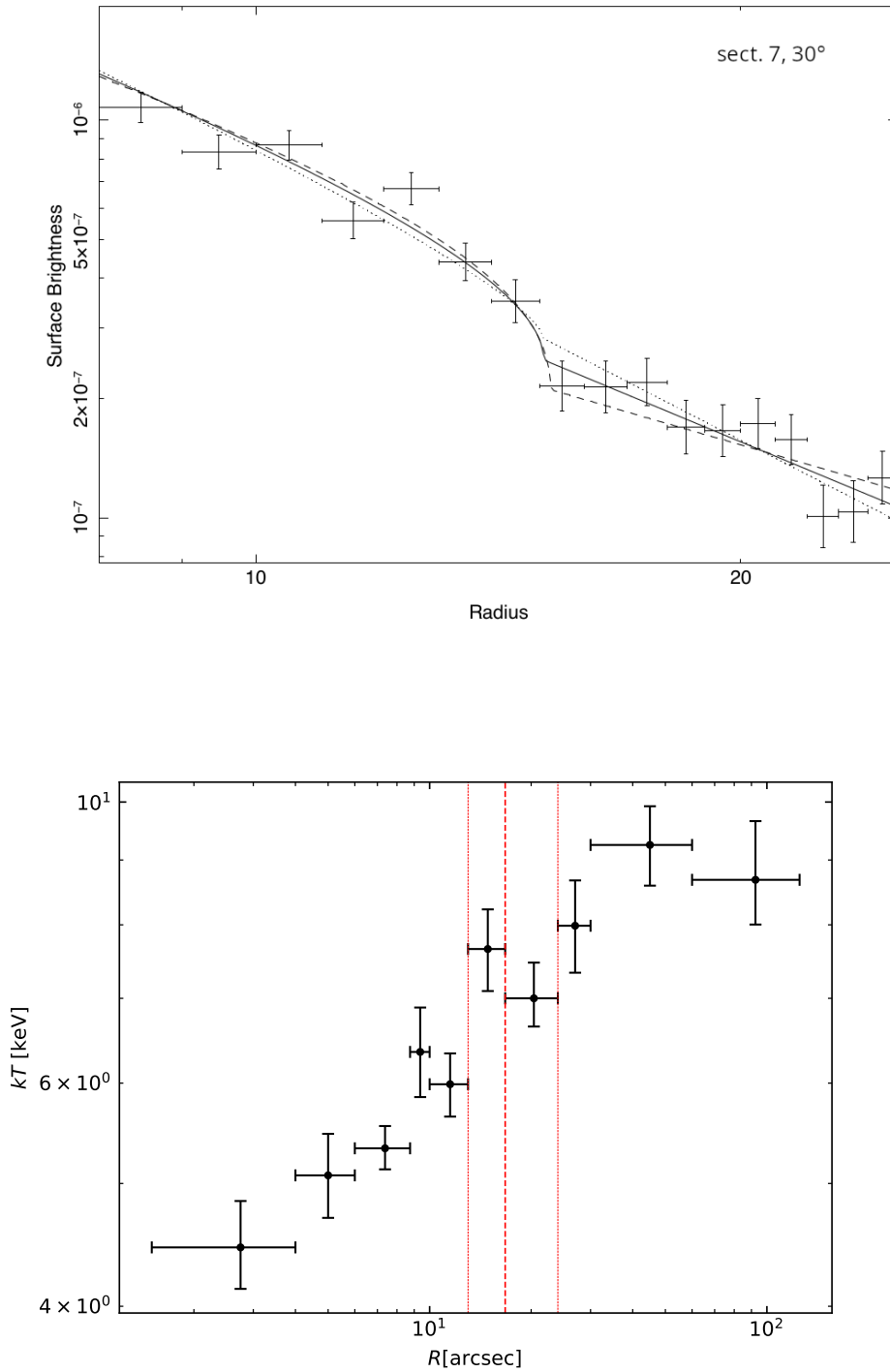
Figure 4.17: Radial profiles which indicate the presence of a shock wave. The *dashed red* lines rapresent the inner and the outer regions of the front. *Top panel*: Broken power-law fitted to the surface brightness profile. The temperature jump predicted is $1.4 \, ^{+0.9}_{-0.3}$. *Bottom panel*: Temperature profile obtained from the deprojected analysis. The temperature jump observed is $1.1 \, ^{+0.1}_{-0.1}$. Vertical bars indicate error which are estimated at 1σ. Horizontal bars indicate the radius of the annulus of each bin.
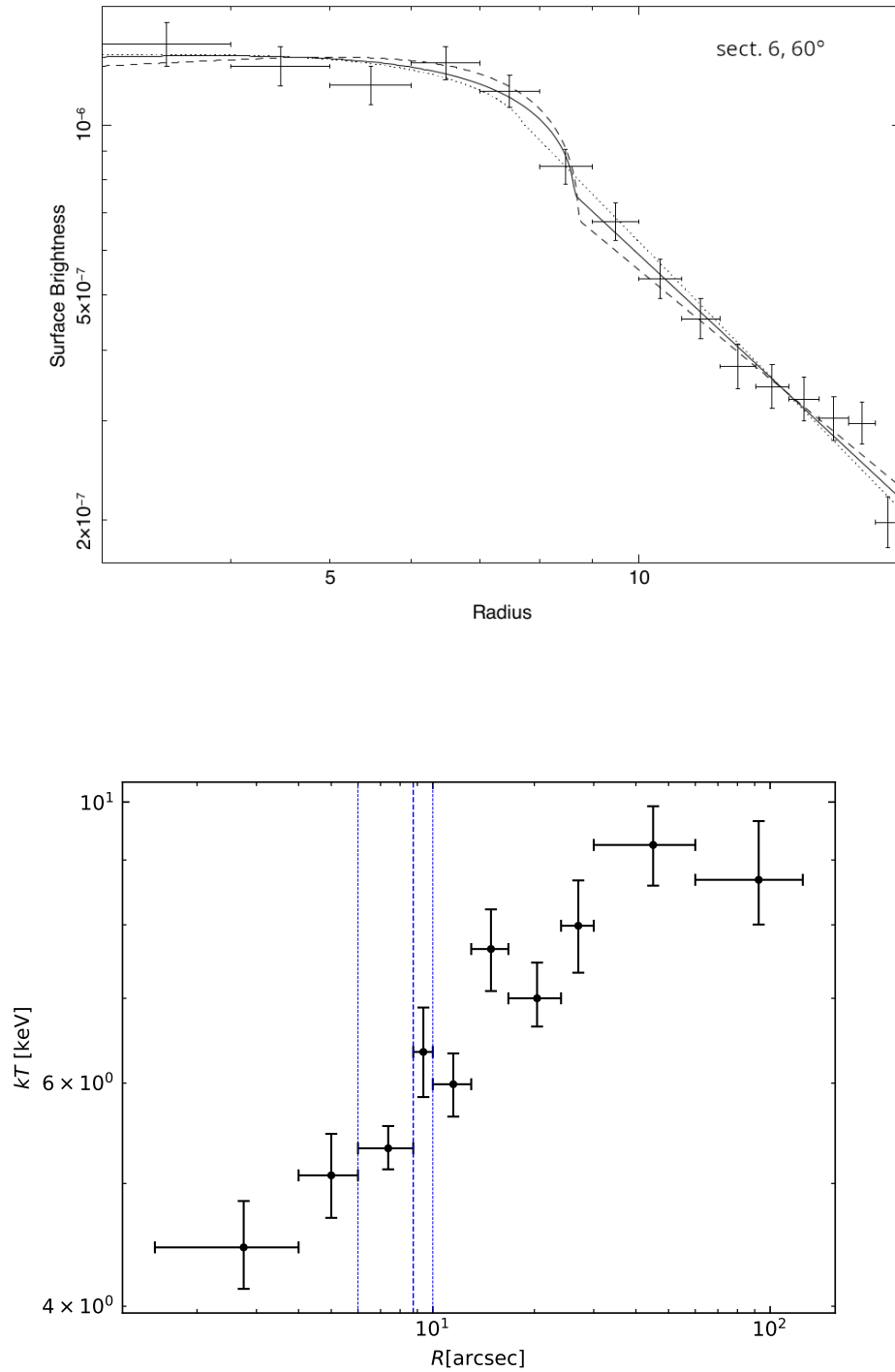
Figure 4.18: Radial profiles indicate the presence of a inner discontinuity. The *dashed blue* lines represent the inner and the outer regions of the front. *Top panel*: Broken power-law fitted to the surface brightness profile. *Bottom panel*: Temperature profile obtained from the deprojected analysis. The inner discontinuity is found at 8.7″ from the center. Vertical bars indicate error which are estimated at 1σ. Horizontal bars indicate the radius of the annulus of each bin.

Chapter 5

Conclusions

Recent observations in the low radio frequencies revealed the presence of a very steep $(\alpha \simeq -1.7, S \propto \nu^{\alpha})$ diffuse radio emission on Mpc scale in cool-core galaxy clusters (Savini et al., 2018, 2019; Raja et al., 2020). The discovery of this new zoology of diffuse emission opens new questions on the mechanisms of particle acceleration. The authors suggested a possible explanation in which the cluster-scale emission is produced by the sloshing motion of the core after a minor merger. As this event dissipates lower energy than major merger, very steep radio spectra could be commonly observed at the low radio frequencies in cluster with a dense cool-core, and with some levels of X-ray disturbances on larger scale.

5.1   Our results

Motivated by these recent discoveries, we carried out the LOFAR radio analysis of the cool-core cluster RBS797 to investigate the presence of steep diffuse emission extended outside the mini-halo. We also analysed archival X-ray observations to search for cold front at the mini-halo edges.
Both radio and X-ray observations revealed interesting peculiarity of this cool-core cluster. Before giving an interpretation about the multi-wavelength properties of the cluster, we summarize the main results obtained from LOFAR and Chandra analysis.

5.1.1   LOFAR results

Despite RBS797 is a cool-core cluster previously studied with VLA observations (e.g. Gitti et al., 2005), its emission at low radio frequency was not possible until the advent of LOFAR, which provides the necessary sensitivity and resolution to investigate the mini-halo. In particular, we produced the radio images, both at high and low resolution, and we performed a spectral index analysis.
The new radio observation presented in Chap. 3, led to the following results:

- We imaged the data at low resolution to maximise the sensitivity to low surface brightness extended emission of the cluster. This image with a restoring beam of $4.7'' \times 6.9''$ shows the presence of diffuse emission covering $\simeq 150$ kpc from the center . We associated this radio emission to the mini-halo hosted by this cool-core, previously discovered by Gitti et al. (2006) with 1.4 GHz VLA observations. From

this image, we do not observe extended emission outside the core. Therefore, we decided to produce a lower resolution image, with a resolution of $26'' \times 28''$, in order to compare the upper limit to the undetected emission with the radio power of the diffuse emission found by Savini et al. (2018). In particular, considering $3 \times$ RMS, we obtained $P_{140\mathrm{MHz}} < 1.4 \times 10^{24}$ W/Hz, with respect to 4.4×10^{24} W/Hz measured by the authors, and therefore we excluded a diffuse emission outside the core.

- The high resolution image, $2.4'' \times 3.3''$, reveals the presence of the prominent radio lobes which fill the two well-known cavities. In particular, they extent to 75 kpc from the center in the northeast-southwest direction.

- We analysed the spectral index properties between 140 and 1400 MHz combining LOFAR and archival VLA observation. From the images produced, with a restoring beam of $5'' \times 5''$, we noted as the VLA emission covers a larger scale than the LOFAR emission, and extends 190 kpc from the center in the north-south direction. We measured a spectral index which becomes flatter with increasing distance from the center of the cluster. From the map, we noted a steepening of the spectrum in the regions corresponding to the radio lobes, in particular $\alpha = -1.04 \pm 0.07$ ($S_\nu \propto \nu^\alpha$). These radio bubble produced by the central AGN displace the ICM and create the so-called X-ray cavities. They present typical steep spectra due to the spectral ageing of the synchrotron emission.

- The new LOFAR observation allowed us to perform a spectral index radial profile, which leads to the discovery of a flattening of the spectral index moving toward the external region of the cluster, in particular at distance of $\simeq 64$ kpc α is -0.45 ± 0.09. This is the first detection of a flat spectral index of the radio diffuse emission in GCs, and we associated this trend to a possible shock propagating in the ICM.

5.1.2   Chandra results

RBS797 was also widely studied in X-ray observations, especially its predominant system of cavities, filled by the radio lobes (e.g. Doria et al., 2012; Cavagnolo et al., 2011). Therefore, in this thesis we focused on the Chandra analysis of RBS797 aimed at detecting evidences of discontinuities in the ICM, such as shocks and cold fronts, and investigating their possible relation to the extended radio emission. We performed a morphological and spectral analysis, presented in Chap. 4, which reveal the presences of an inner and an outer discontinuity.
We report the main results of the Chandra analysis:

- From the analysis of radial surface brightness profiles performed by considering sectors around the cluster, we detected an inner and an outer brightness discontinuity at a distance from the center of the cluster of $8.7''$, corresponding to $\simeq 43$ kpc, and $16.7''$, corresponding to $\simeq 83$ kpc, respectively. These are consistent with the edges identified by Doria et al. (2012) by means of unsharp masked images.

- To properly investigate the nature of the brightness discontinuities revealed in the morphological analysis, i.e. discriminating between a cold front or a shock wave origin, we analyzed the spectral properties of the ICM from dedicated sectors,
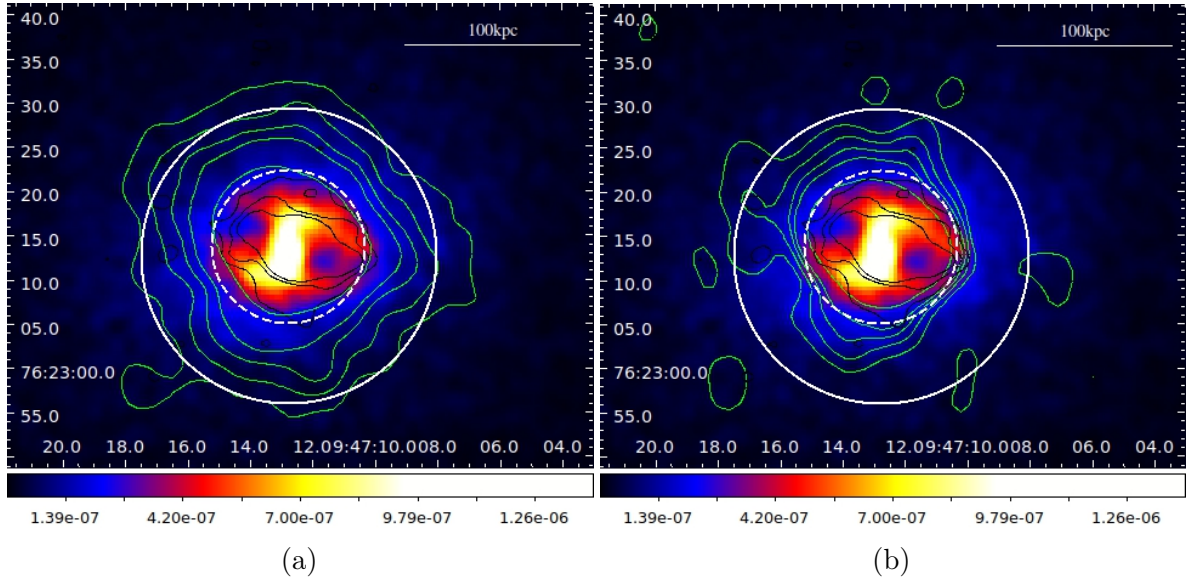
Figure 5.1: (a) Chandra smoothed image (0.5-2 keV) with overlaid the 1.4 VLA GHz radio contours (*green*) spaced by a factor of 2 starting from 3× RMS, where RMS = 448μJy/beam and high-resolution, LOFAR 140 MHz radio contours (*black*) spaced by a factor of 2 starting from 3× RMS, where RMS= 27μJy/beam. The VLA image has a restoring beam of $5'' \times 5''$ and the high resolution, LOFAR images has a restoring beam of $2.4'' \times 3.3''$. (b)Chandra smoothed image (0.5-2 keV) with overlaid the 140 MHz low resolution, LOFAR contours (*green*) spaced by a factor of 2 starting from 3× RMS, where RMS = 258μJy/beam and high-resolution, LOFAR 140 MHz radio contours (*black*) spaced by a factor of 2 starting from 3× RMS, where RMS= 27μJy/beam. The low resolution LOFAR image has a restoring beam of $5'' \times 5''$ and the high resolution image has a restoring beam of $2.4'' \times 3.3''$. In both panels the *white circle* and the *dashed white circle* represent the outer and the inner discontinuity, respectively. The color bar represents the flux density in unit of phot/cm^2/s.

corresponding to the inner and outer regions of the fronts.

The inner discontinuity at $8.7''$ reveals properties typical of a cold front, in particular it presents lower temperature and higher density inside the front, however this jump is likely produced by the bright rims surrounding the cavities system (Doria et al., 2012). Indeed, from Fig. 5.1a, which shows the Chandra smoothed image with overlaid the 140 MHz high resolution radio contours (black contours), we can see how the inner discontinuity (dashed white circle) surrounds the system of cavities, filled by the two radio lobes which we detected in the LOFAR image with a resolution of $2.4'' \times 3.3''$.

The outer jump at $16.7''$ is instead characterized by higher temperature and density in the inner region of the edge, where the pressure is also higher, showing a jump obtained from the deprojected analysis at a significance of $\simeq 2\sigma$. Therefore, this discontinuity is likely associated with a shock wave propagating to the external region of the cluster.

- We also performed an azymuthally-averaged spectral analysis to determine whether these discontinuities trace cocoon-shaped fronts, and thus represent global features in the ICM possibly associated to the central AGN.

Therefore, we extracted spectra from ten concentric annuli centered on the cluster. At the position of the inner ($8.7''$) and outer discontinuities ($16.7''$) revealed in the surface brightness analysis, we detected two jumps with the same thermodynamical properties found in the spectral analysis in sectors.

In particular, for the outer discontinuity we measured properties compatible with a shock front, which presents a pressure jump at a significance of $\simeq 2\sigma$. This possible shock has a Mach number of 1.1.

5.2   The first evidence of a shock in a mini-halo cluster

RBS797 is characterized by the presence of a radio mini-halo. These objects generally present steep radio spectrum and are found in cool-core GCs. The origin of mini-halos is still debated, it could be produced by secondary electrons generated by the collisions between thermal protons of the ICM and relativistic cosmic ray protons, or to the re-acceleration of CR electrons by turbulence in the cool-core.

Turbulence may be generated by sloshing motions of the core after a minor merger event (e.g. Mazzotta & Giacintucci, 2008; ZuHone et al., 2013) or by AGN feedback (e.g. Cassano et al., 2008; Doria et al., 2012; Gitti, 2015; Bravi et al., 2016). On one hand, the presence of cold fronts in cool-core GCs support the scenario in which turbulence is induced by gas sloshing motion, and on the other hand the central AGN can drive shocks in the ICM.

Therefore, the X-ray observations of RBS797 may discriminate between these two scenario by determining the nature of the discontinuities as either a cold front (sloshing scenario) or a shock front (AGN feedback scenario).

Our X-ray analysis, presented in Chap. 4, indicates the presence of a shock in the outer regions of the cluster (84 kpc) from the center.

As we discussed before, recent LOFAR observations of CC GC carried out by (Savini et al., 2018) showed a mini-halo which coexists with steep-spectrum emission on Mpc scale, and this diffuse emission can be produced by the sloshing of the core. These steep spectra can be better observed in the low frequencies (Bonafede et al., 2014; Sommer et al., 2017). Thus, LOFAR is the current best array which allows us to study these radio sources in GCs.

In our analysis, we detected a more extended emission at high frequency (VLA, 1.4 GHz) with respect to the low radio frequency (LOFAR, 159 MHz), and a flatter spectrum in the external region of the cluster($-0.45 \pm 0.09, S \propto \nu^{\alpha}$). One possible explanation of these radio peculiar features of diffuse emission in RBS797 can be related to the presence of the shock.

In Fig.5.1a we show the Chandra smoothed image with overlaid the VLA 1.4 GHz and high resolution LOFAR, 140 MHz radio contours, and we compare it with Fig.5.1b, which shows the same X-ray image, with overlaid the LOFAR 140 MHz, low resolution radio contours. From these image, it is evident the extension of the VLA 1.4 GHz contour with respect to the LOFAR 140 MHz contour, and the position of the outer (white circle) and inner (white dashed circle) jump with respect to both emissions. In particular, as we evidenced before, the inner discontinuity surrounds the main system of cavities, filled by the radio lobes.

Gitti et al. (2006) noticed an evidence of differently oriented jets in RBS797, in particular they found radio bubbles emission in the northeast-southwest direction at 1.4 GHz, which we also detected with LOFAR observations.

These radio properties can be associated with three different outburst episodes with a precession of the jet axis of $\simeq 90°$ in $\simeq 10^7$ yr (Doria et al., 2012). In particular, the northeast–southwest inner cavities, and the associated inner bright rims, could be produced by the intermediate outburst, instead the outer edge could be associated with the oldest outburst.

In this scenario, the weak shock detected mainly in the north-south direction in this thesis work can be related with the past activity of the AGN, that could have created large, outer cavities undetected in the current, shallow exposures. The shock propagating in the ICM can accelerate CR electrons to higher energy, leading to an emission at 1.4 GHz more elongated in the north-south direction with respect to 140 MHz emission, and a flattening of the spectral index in the outskirts of the cluster.

A deeper study of this scenario will be perfomed in the immediate future thanks to the observations awarded in Chandra Cycle 21 Large Project (420 ks, PI M. Gitti), which will allow us to confirm the detection of the cocoon shock front at the mini-halo boundary and investigate the presence of large, outer cavities associated to the past outburst. *This will provide for the first time a direct evidence of a clear link between the AGN feedback and the mini-halo origin, already hinted at in our thesis work.*

Bibliography

Abell G. O., 1958, *The Distribution of Rich Clusters of Galaxies.*, ApJS, 3

Ackermann M., et al., 2010, *Fermi LAT observations of cosmic-ray electrons from 7 GeV to 1 TeV*, Phys. Rev. D, 82, 092004

Ackermann M., et al., 2015, *Search for Extended Gamma-Ray Emission from the Virgo Galaxy Cluster with FERMI-LAT*, ApJ, 812, 159

Ackermann M., et al., 2016, *Fermi Large Area Telescope Detection of Extended Gamma-Ray Emission from the Radio Galaxy Fornax A*, ApJ, 826, 1

Ahnen M. L., et al., 2016, *Deep observation of the NGC 1275 region with MAGIC: search of diffuse γ-ray emission from cosmic rays in the Perseus cluster*, A&A, 589, A33

Airy G. B., 1835, *On the Diffraction of an Object-glass with Circular Aperture*, Transactions of the Cambridge Philosophical Society, 5, 283

Arnaud M., Pratt G. W., Piffaretti R., Böhringer H., Croston J. H., Pointecouteau E., 2010, *The universal galaxy cluster pressure profile from a representative sample of nearby systems (REXCESS) and the Y_{SZ} - M_{500} relation*, A&A, 517, A92

Bell A. R., 1978, *The acceleration of cosmic rays in shock fronts - II.*, MNRAS, 182, 443

Bîrzan L., McNamara B. R., Nulsen P. E. J., Carilli C. L., Wise M. W., 2008, *Radiative Efficiency and Content of Extragalactic Radio Sources: Toward a Universal Scaling Relation between Jet Power and Radio Power*, ApJ, 686

Bonafede A., 2010, in Galaxy Clusters: Observations, Physics and Cosmology. p. 17

Bonafede A., 2014, *Low mach number shocks reaccelerating particles in the Intra-cluster Medium: the unique case of PLCKG287.0 +32.9*, Chandra Proposal

Bonafede A., et al., 2009, *Revealing the magnetic field in a distant galaxy cluster: discovery of the complex radio emission from MACS J0717.5 +3745*, A&A, 503, 707

Bonafede A., et al., 2014, *A giant radio halo in the cool core cluster CL1821+643.*, MNRAS, 444, L44

Böringer H., Schuecker P., 2002, *Observational signatures and statistics of galaxy Cluster Mergers: Results from X-ray observations with ROSAT, ASCA, and XMM-Newton.* pp 133–162, doi:10.1007/0-306-48096-4_5

Bravi L., Gitti M., Brunetti G., 2016, *On the connection between radio mini-halos and gas heating in cool core clusters*, arXiv e-prints, p. arXiv:1603.00368

Brüggen M., Bykov A., Ryu D., Röttgering H., 2012, *Magnetic Fields, Relativistic Particles, and Shock Waves in Cluster Outskirts*, Space Sci. Rev., 166

Brunetti G., Jones T. W., 2014, *Cosmic Rays in Galaxy Clusters and Their Nonthermal Emission*, International Journal of Modern Physics D, 23, 1430007

Brunetti G., Venturi T., Dallacasa D., Cassano R., Dolag K., Giacintucci S., Setti G., 2007, *Cosmic Rays and Radio Halos in Galaxy Clusters: New Constraints from Radio Observations*, ApJ, 670, L5

Brunetti G., et al., 2008, *A low-frequency radio halo associated with a cluster of galaxies*, Nature, 455, 944

Brunetti G., Cassano R., Dolag K., Setti G., 2009, *On the evolution of giant radio halos and their connection with cluster mergers*, A&A, 507, 661

Carilli C. L., Taylor G. B., 2002, *Cluster Magnetic Fields*, ARA&A, 40, 319

Cassano R., Brunetti G., Setti G., Venturi T., Giacintucci S., Dallacasa D., 2006, in IAU Joint Discussion. p. 46

Cassano R., Gitti M., Brunetti G., 2008, *A morphological comparison between giant radio halos and radio mini-halos in galaxy clusters*, A&A, 486, L31

Cassano R., Ettori S., Giacintucci S., Brunetti G., Markevitch M., Venturi T., Gitti M., 2010, *On the Connection Between Giant Radio Halos and Cluster Mergers*, ApJ, 721, L82

Cavagnolo K. W., McNamara B. R., Nulsen P. E. J., Carilli C. L., Jones C., Bîrzan L., 2010, *A Relationship Between AGN Jet Power and Radio Power*, ApJ, 720

Cavagnolo K. W., McNamara B. R., Wise M. W., Nulsen P. E. J., Brüggen M., Gitti M., Rafferty D. A., 2011, *A Powerful AGN Outburst in RBS 797*, ApJ, 732

Cavaliere A., Fusco-Femiano R., 1976, *Reprint of 1976A&A....49..137C. X-rays from hot plasma in clusters of galaxies.*, A&A, 500

Clark B. G., 1980, *An efficient implementation of the algorithm 'CLEAN'*, A&A, 89, 377

Coles P., Lucchin F., 2002, *Cosmology: The Origin and Evolution of Cosmic Structure, Second Edition*

Condon J. J., Kaplan D. L., 1998, *VizieR Online Data Catalog: PNe in NRAO VLA Sky Survey (Condon+ 1998)*, VizieR Online Data Catalog, p. J/ApJS/117/361

Condon J. J., Ransom S. M., 2016, *Essential Radio Astronomy*

Condon J. J., Cotton W. D., Greisen E. W., Yin Q. F., Perley R. A., Taylor G. B., Broderick J. J., 1998, *The NRAO VLA Sky Survey*, AJ, 115, 1693

Cornwell T. J., 2008, *Multiscale CLEAN Deconvolution of Radio Synthesis Images*, IEEE Journal of Selected Topics in Signal Processing, 2, 793

Croston J. H., Arnaud M., Pointecouteau E., Pratt G. W., 2006, *An improved deprojection and PSF-deconvolution technique for galaxy-cluster X-ray surface-brightness profiles*, A&A, 459, 1007

Doria A., Gitti M., Ettori S., Brighenti F., Nulsen P. E. J., McNamara B. R., 2012, *A Chandra-VLA Investigation of the X-Ray Cavity System and Radio Mini-Halo in the Galaxy Cluster RBS 797*, ApJ, 753, 47

Eckert D., 2017, in Ness J.-U., Migliari S., eds, The X-ray Universe 2017. p. 12

Ettori S., Gastaldello F., Leccardi A., Molendi S., Rossetti M., Buote D., Meneghetti M., 2010, *Mass profiles and c-M_{DM} relation in X-ray luminous galaxy clusters*, A&A, 524

Evrard A. E., 1997, *The intracluster gas fraction in X-ray clusters: constraints on the clustered mass density*, MNRAS, 292, 289

Fabian A. C., 1994, *Cooling Flows in Clusters of Galaxies*, ARA&A, 32

Fabian A. C., Sanders J. S., Taylor G. B., Allen S. W., Crawford C. S., Johnstone R. M., Iwasawa K., 2006, *A very deep Chandra observation of the Perseus cluster: shocks, ripples and conduction*, MNRAS, 366, 417

Felten J. E., Gould R. J., Stein W. A., Woolf N. J., 1966, *X-Rays from the Coma Cluster of Galaxies*, ApJ, 146

Feretti L., Dallacasa D., Giovannini G., Tagliani A., 1995, *The magnetic field in the Coma cluster.*, A&A, 302, 680

Feretti L., Dallacasa D., Govoni F., Giovannini G., Taylor G. B., Klein U., 1999, *The radio galaxies and the magnetic field in Abell 119*, A&A, 344, 472

Ferrari C., 2003, *High resolution observations of the merging cluster Abell 3921*, Chandra Proposal

Furlanetto S. R., Loeb A., 2001, *Intergalactic Magnetic Fields from Quasar Outflows*, ApJ, 556, 619

Ghirardini V., et al., 2019, *Universal thermodynamic properties of the intracluster medium over two decades in radius in the X-COP sample*, A&A, 621, A41

Giacintucci S., Markevitch M., Venturi T., Clarke T. E., Cassano R., Mazzotta P., 2014, *New Detections of Radio Minihalos in Cool Cores of Galaxy Clusters*, ApJ, 781, 9

Giacintucci S., Markevitch M., Cassano R., Venturi T., Clarke T. E., Brunetti G., 2017, *Occurrence of Radio Minihalos in a Mass-limited Sample of Galaxy Clusters*, ApJ, 841, 71

Gitti M., 2015, in Proceedings of "The many facets of extragalactic radio surveys: towards new scientific challenges" (EXTRA-RADSUR2015). 20-23 October 2015. Bologna. p. 43

Gitti M., 2016, *Radio mini-halos and AGN heating in cool core clusters of galaxies*, arXiv e-prints, p. arXiv:1602.08312

Gitti M., Brunetti G., Setti G., 2002, *Modeling the interaction between ICM and relativistic plasma in cooling flows: The case of the Perseus cluster*, A&A, 386, 456

Gitti M., Brunetti G., Setti G., Feretti L., 2003, in Bowyer S., Hwang C.-Y., eds, Astronomical Society of the Pacific Conference Series Vol. 301, Matter and Energy in Clusters of Galaxies. p. 489 (`arXiv:astro-ph/0207145`)

Gitti M., Feretti L., Schindler S., 2005, in American Astronomical Society Meeting Abstracts. p. 177.13

Gitti M., Feretti L., Schindler S., 2006, *Multifrequency VLA radio observations of the X-ray cavity cluster of galaxies RBS797: evidence of differently oriented jets*, A&A, 448, 853

Gitti M., Piffaretti R., Schindler S., 2007, *Mass distribution in the most X-ray-luminous galaxy cluster RX J1347.5-1145 studied with XMM-Newton*, A&A, 475

Gitti M., Brighenti F., McNamara B. R., 2012, *Evidence for AGN Feedback in Galaxy Clusters and Groups*, Advances in Astronomy, 2012

Govoni F., Feretti L., 2004, *Magnetic Fields in Clusters of Galaxies*, International Journal of Modern Physics D, 13, 1549

Govoni F., Feretti L., Giovannini G., Dallacasa D., Taylor G. B., 2002, in Gilfanov M., Sunyeav R., Churazov E., eds, Lighthouses of the Universe: The Most Luminous Celestial Objects and Their Use for Cosmology. p. 78, doi:10.1007/10856495_10

Govoni F., Murgia M., Feretti L., Giovannini G., Dolag K., Taylor G. B., 2006, *The intracluster magnetic field power spectrum in Abell 2255*, A&A, 460, 425

Grasso D., Rubinstein H. R., 2001, *Magnetic fields in the early Universe*, Phys. Rep., 348, 163

Hardcastle M. J., et al., 2016, *LOFAR/H-ATLAS: a deep low-frequency survey of the Herschel-ATLAS North Galactic Pole field*, MNRAS, 462, 1910

Högbom J. A., 1974, *Aperture Synthesis with a Non-Regular Distribution of Interferometer Baselines*, A&AS, 15, 417

Johnson R. E., Markevitch M., Wegner G. A., Jones C., Forman W. R., 2010, *Core Gas Sloshing in Abell 1644*, ApJ, 710, 1776

Kalberla P. M. W., Burton W. B., Hartmann D., Arnal E. M., Bajaja E., Morras R., Pöppel W. G. L., 2005, *The Leiden/Argentine/Bonn (LAB) Survey of Galactic HI. Final data release of the combined LDS and IAR surveys with improved stray-radiation corrections*, A&A, 440, 775

King I., 1962, *The structure of star clusters. I. an empirical density law*, AJ, 67

Longair M. S., 2011, *High Energy Astrophysics*

Macario G., Venturi T., Brunetti G., Dallacasa D., Giacintucci S., Cassano R., Bardelli S., Athreya R., 2010, *The very steep spectrum radio halo in Abell 697*, A&A, 517, A43

Markevitch M., 2012, in Chamseddine A. H., ed., Twelfth Marcel Grossmann Meeting on General Relativity. pp 397–410, doi:10.1142/9789814374552_0018

Markevitch M., Vikhlinin A., 2007, *Shocks and cold fronts in galaxy clusters*, Phys. Rep., 443

Markevitch M., Sarazin C. L., Vikhlinin A., 1999, *Physics of the Merging Clusters Cygnus A, A3667, and A2065*, ApJ, 521

Mazzotta P., Giacintucci S., 2008, *Do Radio Core-Halos and Cold Fronts in Non-Major-Merging Clusters Originate from the Same Gas Sloshing?*, ApJ, 675, L9

McNamara B. R., Nulsen P. E. J., 2007, *Heating Hot Atmospheres with Active Galactic Nuclei*, ARA&A, 45

McNamara B. R., Nulsen P. E. J., 2012, *Mechanical feedback from active galactic nuclei in galaxies, groups and clusters*, New Journal of Physics, 14

Mohan N., Rafferty D., 2015, *PyBDSF: Python Blob Detection and Source Finder* (ascl:1502.007)

Mohr J. J., Mathiesen B., Evrard A. E., 1999, *Properties of the Intracluster Medium in an Ensemble of Nearby Galaxy Clusters*, ApJ, 517, 627

Molendi S., Pizzolato F., 2001, *Is the Gas in Cooling Flows Multiphase?*, ApJ, 560

Molendi S., De Grandi S., Guainazzi M., 2002, *A BeppoSAX view of the Centaurus Cluster*, A&A, 392, 13

Nulsen P. E. J., McNamara B. R., Wise M. W., David L. P., 2005, *The Cluster-Scale AGN Outburst in Hydra A*, ApJ, 628, 629

O'Sullivan E., Worrall D. M., Birkinshaw M., Trinchieri G., Wolter A., Zezas A., Giacintucci S., 2011, *Interaction between the intergalactic medium and central radio source in the NGC 4261 group of galaxies*, MNRAS, 416

Offringa A. R., van de Gronde J. J., Roerdink J. B. T. M., 2012, *A morphological algorithm for improving radio-frequency interference detection*, A&A, 539, A95

Offringa A. R., et al., 2014, *WSCLEAN: an implementation of a fast, generic wide-field imager for radio astronomy*, MNRAS, 444, 606

Peebles P. J. E., Yu J. T., 1970, *Primeval Adiabatic Perturbation in an Expanding Universe*, ApJ, 162

Perley R. A., Taylor G. B., 1991, *VLA Observations of 3C 295—A Young Radio Galaxy?*, AJ, 101, 1623

Peterson J. R., Fabian A. C., 2006, *X-ray spectroscopy of cooling clusters*, Phys. Rep., 427, 1

Pratt G. W., Croston J. H., Arnaud M., Böhringer H., 2009, *Galaxy cluster X-ray luminosity scaling relations from a representative local sample (REXCESS)*, A&A, 498

Press W. H., Schechter P., 1974, *Formation of Galaxies and Clusters of Galaxies by Self-Similar Gravitational Condensation*, ApJ, 187

Raja R., et al., 2020, *Diffuse radio emission in the galaxy cluster SPT-CL J2031-4037: a steep-spectrum intermediate radio halo?*, MNRAS, 493, L28

Rengelink R. B., Tang Y., de Bruyn A. G., Miley G. K., Bremer M. N., Roettgering H. J. A., Bremer M. A. R., 1997, *The Westerbork Northern Sky Survey (WENSS), I. A 570 square degree Mini-Survey around the North Ecliptic Pole*, A&AS, 124, 259

Rossetti M., Molendi S., 2004, *Is there a hard tail in the Coma Cluster X-ray spectrum?*, A&A, 414, L41

Russell H. R., Sanders J. S., Fabian A. C., 2008, *Direct X-ray spectral deprojection of galaxy clusters*, MNRAS, 390, 1207

Rybicki G. B., Lightman A. P., 1986, *Radiative Processes in Astrophysics*

Ryle M., Hewish A., 1960, *The synthesis of large radio telescopes*, MNRAS, 120, 220

Sarazin C. L., 2002, *The Physics of Cluster Mergers*. pp 1–38, doi:10.1007/0-306-48096-4_1

Sarazin C. L., 2009, *X-Ray Emission from Clusters of Galaxies*

Savini F., et al., 2018, *First evidence of diffuse ultra-steep-spectrum radio emission surrounding the cool core of a cluster*, MNRAS, 478, 2234

Savini F., et al., 2019, *A LOFAR study of non-merging massive galaxy clusters*, A&A, 622, A24

Scaife A. M. M., Heald G. H., 2012, *A broad-band flux scale for low-frequency radio telescopes*, MNRAS, 423, L30

Schindler S., Castillo-Morales A., De Filippis E., Schwope A., Wambsganss J., 2001, *Discovery of depressions in the X-ray emission of the distant galaxy cluster RBS797 in a CHANDRA observation*, A&A, 376

Shimwell T. W., et al., 2017, *The LOFAR Two-metre Sky Survey. I. Survey description and preliminary data release*, A&A, 598, A104

Shimwell T. W., et al., 2019, *The LOFAR Two-metre Sky Survey. II. First data release*, A&A, 622, A1

Smirnov O. M., Tasse C., 2015, *Radio interferometric gain calibration as a complex optimization problem*, MNRAS, 449, 2668

Sommer M. W., Basu K., Intema H., Pacaud F., Bonafede A., Babul A., Bertoldi F., 2017, *Mpc-scale diffuse radio emission in two massive cool-core clusters of galaxies*, MNRAS, 466, 996

Springel V., 2005, *The cosmological simulation code GADGET-2*, MNRAS, 364

Sunyaev R. A., Zeldovich Y. B., 1972, *The Observations of Relic Radiation as a Test of the Nature of X-Ray Radiation from the Clusters of Galaxies*, Comments on Astrophysics and Space Physics, 4, 173

Sutherland R. S., Dopita M. A., 1993, *Cooling Functions for Low-Density Astrophysical Plasmas*, ApJS, 88

Tasse C., et al., 2018, *Faceting for direction-dependent spectral deconvolution*, A&A, 611, A87

Taylor G. B., Perley R. A., 1993, *Magnetic Fields in the Hydra A Cluster*, ApJ, 416, 554

Thompson A. R., Moran J. M., Swenson George W. J., 2017, *Interferometry and Synthesis in Radio Astronomy, 3rd Edition*, doi:10.1007/978-3-319-44431-4.

Urban O., et al., 2014, *Azimuthally resolved X-ray spectroscopy to the edge of the Perseus Cluster*, MNRAS, 437, 3939

Vazza F., Brüggen M., 2014, *Do radio relics challenge diffusive shock acceleration?*, MNRAS, 437, 2291

Vazza F., Tormen G., Cassano R., Brunetti G., Dolag K., 2006, *Turbulent velocity fields in smoothed particle hydrodymanics simulated galaxy clusters: scaling laws for the turbulent energy*, MNRAS, 369, L14

Vazza F., Jones T. W., Brüggen M., Brunetti G., Gheller C., Porter D., Ryu D., 2017, *Turbulence and vorticity in Galaxy clusters generated by structure formation*, MNRAS, 464, 210

Venturi T., Giacintucci S., Brunetti G., Cassano R., Bardelli S., Dallacasa D., Setti G., 2007, *GMRT radio halo survey in galaxy clusters at z = 0.2-0.4. I. The REFLEX sub-sample*, A&A, 463, 937

Venturi T., Giacintucci S., Dallacasa D., Cassano R., Brunetti G., Bardelli S., Setti G., 2008, *GMRT radio halo survey in galaxy clusters at z = 0.2-0.4. II. The eBCS clusters and analysis of the complete sample*, A&A, 484, 327

Venturi T., et al., 2017, *The two-component giant radio halo in the galaxy cluster Abell 2142*, A&A, 603, A125

Vikhlinin A., Markevitch M., Murray S. S., Jones C., Forman W., Van Speybroeck L., 2005, *Chandra Temperature Profiles for a Sample of Nearby Relaxed Galaxy Clusters*, ApJ, 628, 655

Voit G. M., 2005, *Tracing cosmic evolution with clusters of galaxies*, Reviews of Modern Physics, 77

Wayth R. B., et al., 2015, *GLEAM: The GaLactic and Extragalactic All-Sky MWA Survey*, PASA, 32, e025

Wik D. R., et al., 2014, *NuSTAR Observations of the Bullet Cluster: Constraints on Inverse Compton Emission*, ApJ, 792, 48

Wilber A., et al., 2018, *LOFAR discovery of an ultra-steep radio halo and giant head-tail radio galaxy in Abell 1132*, MNRAS, 473, 3536

Wittor D., Vazza F., Brüggen M., 2017, *Testing cosmic ray acceleration with radio relics: a high-resolution study using MHD and tracers*, MNRAS, 464, 4448

Wrobel J. M., Walker R. C., 1999, *Sensitivity*. p. 171

Xue Y.-J., Wu X.-P., 2000, *Properties of the double β model for intracluster gas*, MNRAS, 318, 715

Zhang C., Churazov E., Schekochihin A. A., 2018, *Generation of internal waves by buoyant bubbles in galaxy clusters and heating of intracluster medium*, MNRAS, 478, 4785

Zhuravleva I., et al., 2014, *Turbulent heating in galaxy clusters brightest in X-rays*, Nature, 515, 85

ZuHone J. A., Markevitch M., 2010, in American Astronomical Society Meeting Abstracts #215. p. 378.02

ZuHone J. A., Markevitch M., Brunetti G., Giacintucci S., 2013, *Turbulence and Radio Mini-halos in the Sloshing Cores of Galaxy Clusters*, ApJ, 762, 78

ZuHone J. A., Brunetti G., Giacintucci S., Markevitch M., 2015, *Testing Secondary Models for the Origin of Radio Mini-Halos in Galaxy Clusters*, ApJ, 801, 146

Zúñiga V., Haridas N., Erdogan A. T., Arslan T., 2009, *Effect of a Central Antenna Element on the Directivity, Half-Power Beamwidth and Side-Lobe Level of Circular Antenna Arrays*, 2009 NASA/ESA Conference on Adaptive Hardware and Systems, pp 252–256

van Haarlem M. P., et al., 2013, *LOFAR: The LOw-Frequency ARray*, A&A, 556, A2

van Weeren R. J., et al., 2014, *A Distant Radio Mini-halo in the Phoenix Galaxy Cluster*, ApJ, 786, L17

van Weeren R. J., et al., 2016, *LOFAR Facet Calibration*, ApJS, 223, 2

van Weeren R. J., et al., 2017, *The case for electron re-acceleration at galaxy cluster shocks*, Nature Astronomy, 1, 0005

van Weeren R. J., de Gasperin F., Akamatsu H., Brüggen M., Feretti L., Kang H., Stroe A., Zandanel F., 2019, *Diffuse Radio Emission from Galaxy Clusters*, Space Sci. Rev., 215

van de Weygaert R., Bond J. R., 2008, *Observations and Morphology of the Cosmic Web*, doi:10.1007/978-1-4020-6941-3_11.

Ringraziamenti

Ho conseguito questo percorso con pazienza e determinazione, con il fine di coronare il mio sogno che si concretizza con questa tesi.

Vorrei ringraziare tutti coloro che mi hanno accompagnato e sostenuto durante questi anni e senza i quali non ce l'avrei fatta.

Ringrazio la mia relatrice Myriam Gitti, per la sua professionalità e competenza, e per tutto il tempo dedicato alla realizzazione di questo lavoro. Grazie anche alla mia co-relatrice Annalisa Bonafede per essersi sempre resa disponibile ad aiutarmi e per l'opportunità che mi ha dato di poter svolgere parte di questa tesi all'osservatorio di Leiden. Quindi ci tengo a ringraziare Timothy Shimwell, Rainout Van Weeren per i loro insegnamenti e tutti i ragazzi, Andrea, Jit, Gabriella per avermi accolta subito. Uno speciale grazie va ad Alessandro, per essere stato sempre presente, per i consigli e aiuti. Grazie papà, per avermi trasmesso l'amore per la scienza e grazie mamma per avermi sempre ammirata per la mia scelta. Grazie nonni, per avermi sempre incoraggiata a non mollare mai. Un grande grazie va a mio fratello Alessio, per essere stato sempre al mio fianco.

Questo percorso mi ha anche regalato persone speciali, quali Emilio, Valeria e tutti i miei amici del gruppo Dark Matter, e li ringrazio per tutta la felicità che mi hanno trasmesso in ogni momento trascorso insieme.

Infine, colgo l'occasione per ringraziare una persona che non c'è più, Giovanni Bignami, perché dicendomi semplici parole quando ancora ero una liceale, mi ha incoraggiata ad intraprendere la strada dell'astrofisica, con un entusiasmo che porterò sempre nel cuore. Grazie davvero a tutti.